College of Engineering, Design and Physical Sciences

Turbulent Boundary Layer Noise Mitigation by Geometrical Surface Treatments and Near Wall Passive Flow Control Devices

A dissertation submitted for the degree of Doctor of Philosophy

Chioma Muhammad

November 2021

Without the generous funding by the Thomas Gerald Grey Charitable Trust, this opportunity would not have been possible, and I am deeply grateful for this.

I would like to express my deepest thanks to my academic supervisor Dr. Tze Pei Chong for his support, guidance, patience and believing in me when I didn't.

To my colleagues Alexandros Vathylakis, Laith Ayad Salman, Mohammed Hasheminejad, Auris Juknevicius, Phillip Woodhead and Yasir Al-Okbi, I admire and respect each of you, and thank you for your companionship and along this journey. You have been trailblazers, and your creativity, passion and drive have been nothing short of inspirational.

Thank you to the unsung heroes of the Engineering department– the workshop technicians. With special thanks to Gillimero Schkzamian, Kevin Robinson, Paul Yates and John Wenn for making miracles happen.

Thank you to Patricia Correia and the all the PGR department for your patience and email reminders.

Contents

Abstract

By way of experimental investigation, this thesis outlines the effects of drag reducing riblet wall surface and outer layer large energy break-up (LEBU) device on the broadband noise of the turbulent boundary layer and the potential implications on hypothetical radiated noise from a sharp trailing edge.

Through hot wire measurements on a stable time-invariant artificially tripped boundary layer, the flow conditions of the baseline turbulent boundary layer and the turbulent boundary later over the drag reducing riblets has been investigated. From there, the fluctuating pressure field of the turbulent boundary layer has been measured and characterized by way of wall embedded microphone sensors.

Turbulent spots have been employed as a tool and visual aid into the spatial and temporal effect that the passive flow control devices have on the turbulent flow structures.

It has been found that there is potential to affect trailing edge noise predictions when using a hybridised method of passive flow control, where both the near wall and outer boundary layer are targeted simultaneously.

Table of Figures

Chapter 1 Introduction

1.1. Research motivations

The study of fluid generated noise is far reaching and is relevant in relevant in industries across the world. For example, noise from high rise buildings in architecture and civil engineering, from air conditioning units in building services, from windfarms in the energy industry and noise from airliners in the aviation industry. Whilst initially, they may all seem to be different problems, they are the same in the respect that air passing over and around the structures generates noise.
Since the first commercial jetliner in 1952, air travel has been a popular mode of transport. 4.1 billion passengers were carried in 2017 (1), 4.4 billion in 2018 (2), and International AIR Transport Association (IATA) expects growth to 8.2 billion passengers in 2037 (3) .

Due to the importance of air-travel in migration and economy, it is often the case that new developments are built in the vicinity of airports to facilitate the booming travel industry. This leads to more population around the airport which in turn leads to noise complaints. One such example is the expansion of Heathrow Airport which grew from an airfield on the outskirts of London to the thriving international airport that it is today. With the demand for air-travel on the rise, there has been an application to build a third runway at Heathrow which has been met with much local opposition. One of the main issues – Noise.

According to the WHO (World Health Organisation) excessive noise from air traffic has been linked to cardiovascular, hypertension and sleep disturbance leading to premature deaths. In the aviation industry, ICAO cites aircraft noise as being the biggest issue in perception of airport operation by the

local communities (4). With air transport having grown by 60% in the last ten years and according to ICAO statistics passenger traffic grew by 6.3% on the previous year in 2016 (5). Operational measures have been implemented at multiple airports to mitigate the effect of arriving and departing aircraft on the local populations. For example, at Heathrow Airport there are runway rotations, noise abatement flight paths and time restricted flights (where flights do not operate during specific times of the night).

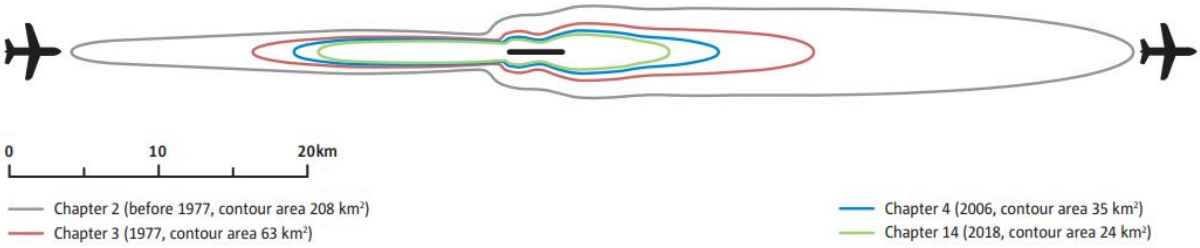

Figure 1.1 – Modified figure from Ref (6) showing the noise maps of area exposed levels of 80db during a single take-off and landing, within the ICAO noise levels. The area grows smaller throughout the decades representing quieter aircraft.

Whilst operational measures have been a great help, there is also the major factor of improved aircraft design which has created the most impact. Figure 1.1 shows the contours of acceptable area affected noise levels of 80dB. From 1977 to 2018, the acceptable area is lower and noise regulations more stringent.

Major strides have been made over the last 50 years in reducing aircraft noise from civil aviation aircrafts. With improved design and technology, the modern aeroengine has become vastly quieter than its earliest predecessor. The largest contributors to this reduction have been the implementation of high bypass engines and the improvements of acoustic liners inside the engine Figure 1.2.

Figure 1.2 - Examples of engine intake technology improvement. Photo courtesy of Rolls Royce (7).

The next noise challenge of modern aircraft design is to reduce airframe noise – the dominant noise sources being turbulent flow of flight surfaces causing propagating pressure waves and structural vibration (8); and separated turbulent flows around bluff bodies especially in the landing gear and high lift high lift devices on the leading and trailing edges of the wings.

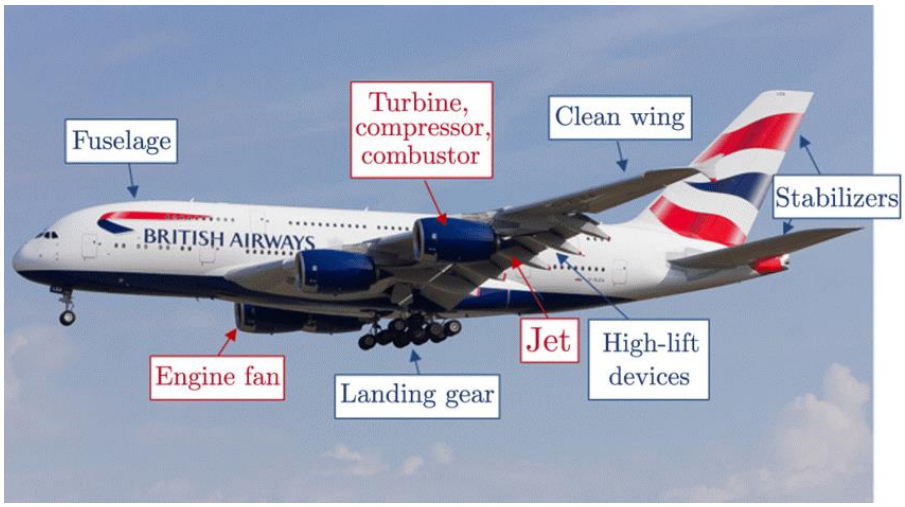

Figure 1.3 - Mian sources of aircraft noise, figure courtesy of Proenca (9) and photograph property of adapted from photo property of Tim Stiehl

In cruise flight, the airframe of the aircraft is considered "clean", where the landing gear is stowed and the aircraft is in optimal configuration for sustained flight. However in slow flight, especially on landing approach, the configuration is "dirty" – the landing gear and high lift devices are deployed. This corresponds to the greatest noise signatures around airports being on take-off and approach shown in Figure 1.1.

Aerodynamic noise is not limited to the aircraft noise. With the everchanging environment, and the impacts of pollution becoming more prevalent - green sources of energy have been on the rise. Wind farms are a popular method of power generation, with turbines being installed both on and off-shore. Whilst wind turbines are less than 40db at around 500m according to GE (10), it is important to note that the location of the wind-turbines is a major factor in the noise complaint. In 2011, windfarm in Lissett, Yorkshire exceeded its specified noise limits on windy days (11).

1.2. Research aims

The aims of the current thesis are to:

- Investigate whether drag the reducing riblets can potentially lead to trailing edge noise reduction from turbulent wall pressure fluctuations.
- Use the fluctuating pressure field beneath a turbulent boundary layer to investigate whether a Large Eddy Break Up Device (LEBU) can potentially reduce trailing edge noise radiation.
- Use turbulent spots to investigate the effect of the riblets and LEBU on the turbulent structure of a single instance of the turbulence to ascertain a potential correlation between the fluctuating streamwise velocity field and pressure field.
- Determine the effect of a hybrid configuration of Riblets and LEBU on a turbulent spot and determine the effects on trailing edge noise radiation.

1.3. Thesis Outline

Chapter 1 introduces and outlines the motivation for this study. To provide a background and understanding of principles related to this study, a number of past and present works will be outlined in Chapter 2. Experimental set-up and methodology are outlined in Chapter 3. Included are the design of the aerodynamic facility and surface treatment fabrication. The chapter also discusses apparatus that were used in this study and the methods of calibration, set-up and data collection. Chapter 4 gives a comprehensive analysis of the aerodynamic and aeroacoustic characteristics of the Baseline turbulent boundary layer compared to turbulent boundary layer over the geometrically treated surface. Also included is a visual study of the composition of a turbulent spot in a laminar boundary layer over both surfaces. The effect of the outer layer drag reduction device is reviewed in Chapter 5 with the focus on the aeroacoustic changes in the wall power spectral density and trailing edge predictions. Included in this chapter are visual studies of the effect of a of the outer layer device on the on a turbulent spot. The final section of the chapter takes a examines the surface pressure and trailing edge predictions of the surface treatment in conjunction with the outer layer device, as well as the combined effect on a turbulent spot.

Chapter 6 is the conclusion where the findings of the entire study are summarised, and recommendations of future works are proposed. The final chapter, Chapter 7, lists the works that have been cited in this study.

Chapter 2 Literature Review

The aim of this chapter is to give a comprehensive understanding of the theory of the turbulent boundary layer and the way in which riblets and LEBU affect it.

2.1. Turbulent Boundary Layer

It is possible to describe the boundary layer in such a way that will make it easily scalable and comparable other boundary layers under different conditions. That is to say, the units of height and velocity by friction velocity and flow viscosity, making the resulting units dimensionless. These units are called wall units and are denoted by a superscript +. The wall normal height (location perpendicular to the flow surface) becomes y^+ and the local velocity as a function of wall shear velocity becomes u^+.

$$y^+ = \frac{yu_\tau}{\upsilon}$$

Equation 2.1

$$u^+ = \frac{u}{u_\tau}$$

Equation 2.2

The structure of a turbulent boundary layer is divided into 2 sections – the inner layer and the outer layer. Each section has distinct characteristics.

	Region	Location	Characterised by:
Inner Layer	Viscous sublayer	$y^+ < 5$ $y/\delta < 0.1$	Organised low speed vortical streaks. Velocity is affected predominantly by viscosity. Reynolds' shear stress is negligible.
	Buffer layer	$5 < y^+ < 30$	Transition between viscosity dominated region and turbulence dominated region.
	Viscous wall region	$y^+ < 50$	The viscous contribution to the shear stress is significant.
Outer Layer	Log-law region	$y^+ > 30$	The log-law holds.
	Overlap region	$y^+ > 50$	The transitional region between the inner and outer layer.

Table 2.1 - Turbulent Boundary layer regions compilation (12) (13) (14)

2.1.1. Viscous sublayer

In early turbulent boundary layer theory, it was believed that the near wall region of the turbulent boundary layer was laminar. It has been called the laminar sublayer; however, low speed coherent structures have been observed in this region.

A review of the structures inside the turbulent boundary layer flow states that coherent streak-like structures were observed in the viscous sublayer as early as 1953 by Hama (15) by use of dye. The streaks were observed to move downstream slowly and randomly wave in the spanwise direction. Hydrogen bubble visualisation of the streaks in the viscous sublayer was conducted by Kline *et al.* (14). The presence of the low speed streaks was found between higher speed counter-rotating vortexes pairs.

a) b)

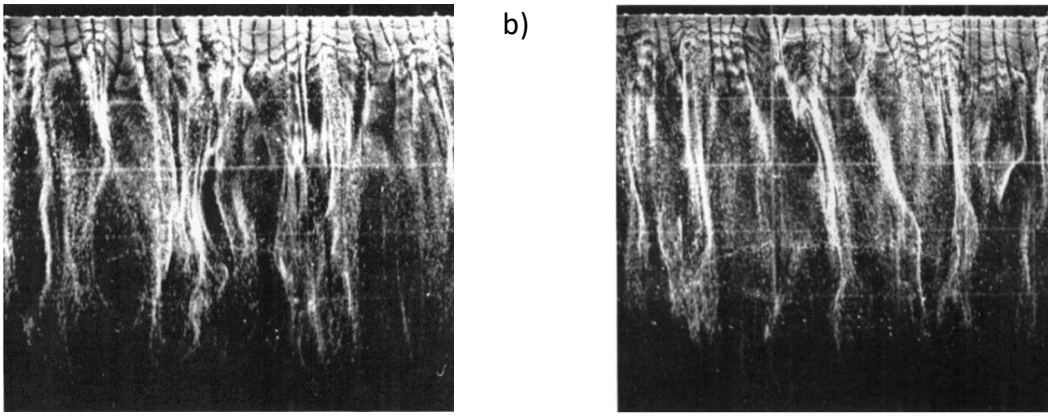

$y^+ = 2.7$ $y^+ = 4.5$

Figure 2.1 - Hydrogen bubble visualisation of the low speed streaks in the viscous sublayer of a turbulent boundary layer as taken from Ref. (14)

The low speed streaks moved slowly downstream, lifting away from the surface before oscillating and lifting sharply from the surface. Low speed fluid is ejected away from the wall into the higher speed outer region of the boundary layer.

a) b)

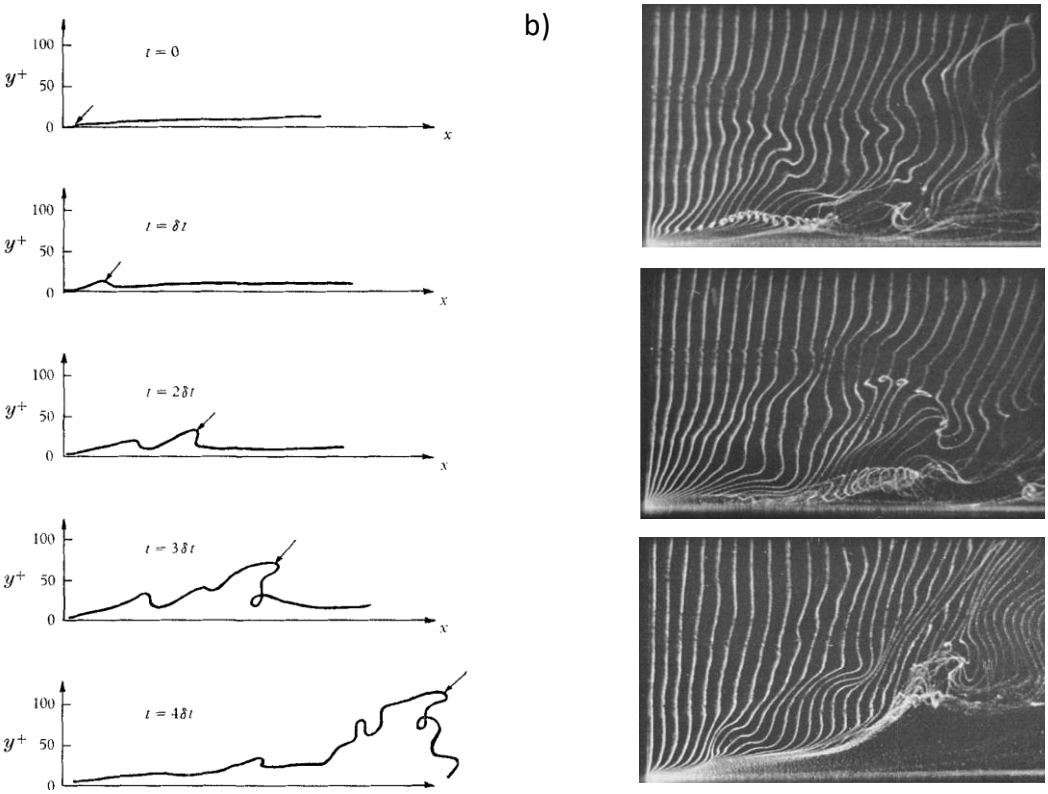

Figure 2.2 – a) Dye streak break up from Kline et al. (14) showing the elongation of the streak, oscillation with increasing magnitude and the breakup and ejection of the low speed wall flow into the outer boundary layer; b) photographs showing the lift up and increasing oscillation of the near wall streak, resulting in the breakup and ejection from Kim et al. (16).

Flow visualisation with emphasis on the turbulent energy production in the near wall region was conducted by Kim et al (16), also using the hydrogen bubble visualisation technique. It was an important study as it showed that the predominant mechanism of turbulent production in the outer layer of the boundary layer originated from the near wall in a process described by Kline *et al.*, which came to be widely known as bursting.

Early investigations of the turbulent boundary layer flow transport properties were conducted by Laufer in 1954 (17) in a fully turbulent pipe flow and it was noted that there was a strong kinetic energy transfer away from the edge of the viscous sublayer, where the maximum kinetic energy rates of production, dissipation and diffusion all reached a maximum. Runstadler *et al.* (18) stipulated that the production of turbulence energy in the outer boundary layer was due to the transfer of energy which was created by the bursting and ejection of the low speed streaks.

Corino *et al.* (19) conducted experiments in a pipe flow and provided visualisation of the movement of fluid from on region to another during an "event", importantly showing the direction. A similar study was conducted by Offen *et al.* (20) where both studies showed during an ejection from the sublayer, the fluid dispelled into the outer region broke down into chaotic disturbance, which corroborates with the findings of Kim *et al.* (14) and Kline *et al.* (16) .This study also showed the movement of fluid towards the wall region from the log region in a "sweep", thus highlighting visually the momentum exchanges of self-generating turbulence.

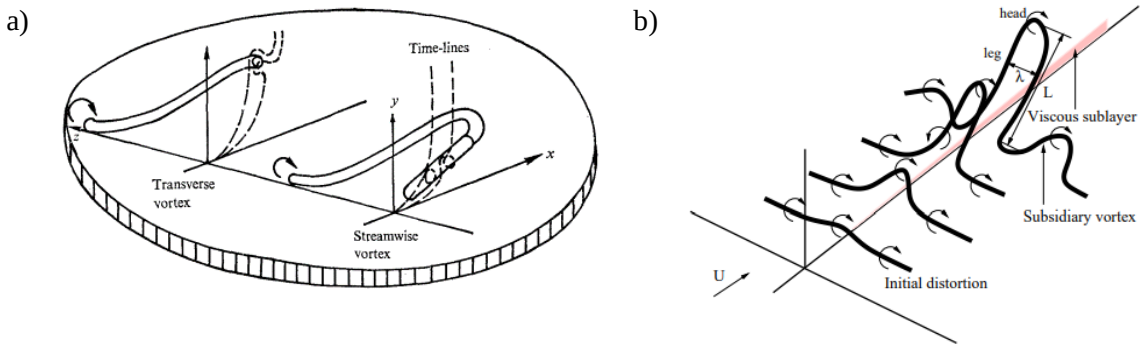

Figure 2.3– a) An adaptation of the lifting of a vortex generated from a low speed streak from Kline (14), showing the effect of spanwise location of visualisation. b) Schematic of the growth of a hairpin vortex (21)

In 1975, Offen (22) produced a paper partly culminating all the previous studies of the lifting and bursting process to provide a full picture of the entire process, and at the same time proposing a slightly different hypothesised model. This model views the lifting stage as an upwell and the

"sweeps" as a passage of bursts which occurred earlier upstream. The most significant part of this model is the description of the oscillatory phase that all the previous studies observed.
Later these structures became known as hairpin vortices and were observed to appear growing in succession downstream by Head and Bandyopadhyay (23), explaining the momentum exchange between the inner and outer layer of the boundary layer and the feedback loop.

2.2. Transition and the Turbulent Spot

The turbulent spot is a useful "tool" to visually examine effect of flow transition. By generating a single instance of turbulence, the interaction of the surface and the turbulence can be examined visually.

The turbulent spot was first observed in 1951 by Emmons (24) whilst looking at the transition of a laminar to turbulent boundary layer on a water table. They were initially Λ-vorticies that eventually presented as random arrow-head shaped instances which grew in amplitude to and frequency downstream until they merged to form the profile of the turbulent boundary layer.

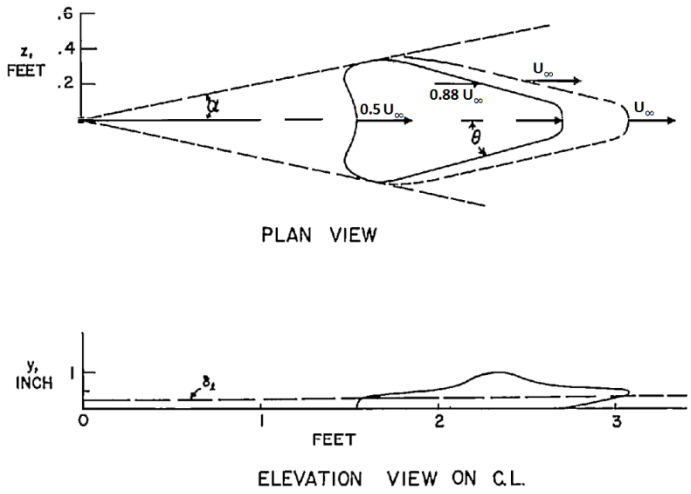

Figure 2.4 – The plan and side elevation of a turbulent spot with corresponding as measured by Schubauer and Klebenoff (25)

Schubaeur and Klebenoff (25) conducted a rather extensive experiment to determine the plan view and side elevation of the turbulent spot - their results are shown in Figure 2.4. Using hotwire anemometry and oscillograms, the laminar boundary layer was excited by way of a spark at the surface and the ensuing turbulent spot measured downstream.

It became evident that the turbulent spot forms an in the shape of an arrowhead or wedge with the sharp leading edge moving with the streamwise flow. It is symmetrical about its streamwise axis. The hotwire registered a calm region stable signal in the laminar boundary layer and was excited by the passage of the turbulent spot. The trailing edge of the spot was marked by a region where the mean velocity at the vertical location returned to the state of the undisturbed laminar boundary layer. It was found that the leading edge of the turbulent spot propagated at a rate of 88% of the free stream velocity, $0.88U_\infty$, and the trailing edge at a rate of $0.5U_\infty$, leading to the downstream elongation. In the plane of symmetry, the trailing edge of the turbulent spot had a half-spread angle, α, of approximately$10°$.

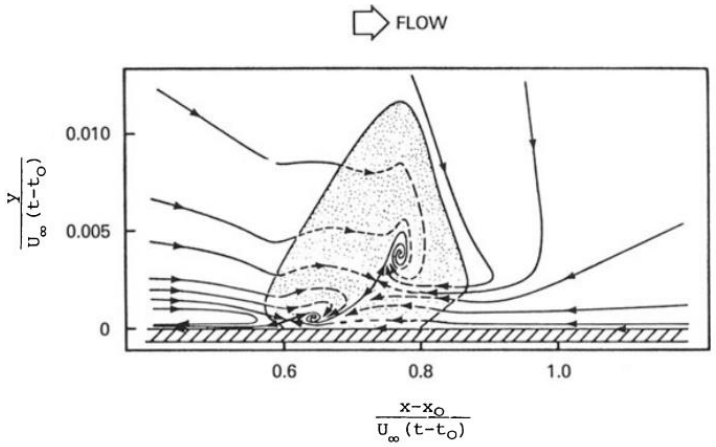

Figure 2.5 – Sketch of the particle trajectories by Cantwell et al. (26), adapted from ref. (27)

Using ensemble averaging Falco (28) found the presence of what seemed to be a large-scale turbulent structure in the spot. However, it was also observed that this coincided with large velocity fluctuations in the observed instantaneous velocity which were more consistent with a turbulent boundary layer. It was therefore suggested that two types of conditions were being observed. Cantwell *et al.* (26) later used laser doppler anemometry to study the particle trajectories inside a turbulent flow, the results were conditionally averaged to provide a general trend of many spots. It showed clearly two vortex structures inside the turbulent spot – one inside near the leading edge of the spot away from the wall and another towards the trailing edge near the wall - these however were never observed in instantaneous results. It was therefore concluded that these vortex-like structures only exist in an ensemble averaged turbulent spot. It was therefore concluded that the fluctuating velocities were more a control factor of the growth of the turbulent spot than the mean values.

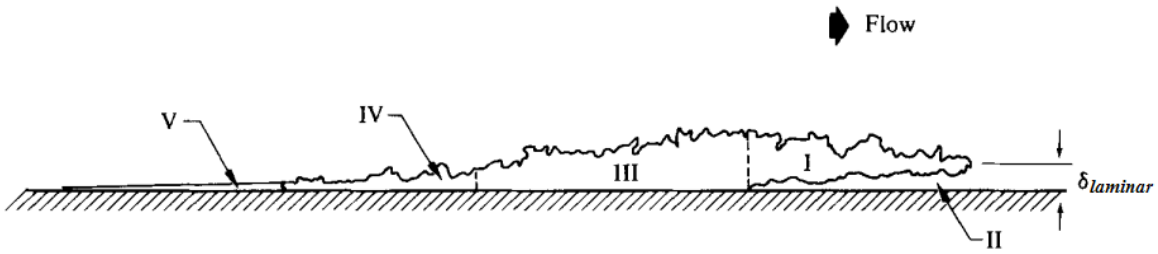

Figure 2.6 – The regions of the turbulent spot. Adapted from Gad-el-Hak et al. (29)

Gad-el-Hak *et al.* (29) used fluorescent dye in a water tank to view and observe the distinct characteristics of different regions of the turbulent spot. These are shown in Figure 2.6, and the 5 regions are summarised as:

I – The approach of the turbulent spot is not witnessed at the wall. There is a distinct "overhang" which is witnessed at the laminar boundary layer height, $\delta_{laminar}$, which corresponded with Wygnaski et. al (30).
II – The laminar boundary layer below the overhang is excited by the overhang as new turbulence is added, and the instability causes the breakdown into turbulence at the boundary to III.
III – The arrival of the wall region of the main body of the turbulent spot is characterised by the approximate maximum height of a turbulent boundary layer. This region is similar flat plate to a turbulent boundary layer in both boundary layer growth rate and turbulence intensity. The maximum shear stress is located at the boundary between III and IV.
IV – At the trailing edge if the turbulent spot, there is a section of fluid that was originally part of the III that begins to entrain and interact with the surrounding laminar boundary flow and outer laminar free stream flow. This the section of the spot which convects downstream at $0.5U_{\infty}$.
V – The passage of main body of the turbulent spot has passed and the entraining laminar boundary layer prevails. This is a highly stable laminar boundary layer and is called the "calmed" region. It is characterised with higher velocity which decays to the undisturbed boundary layer characteristics.

2.3. Passive Flow Control

2.3.1. Riblets

Riblets are a classic example of biomimicry. Early studies by Reif and Dinklelacker (31) studied the exceptional movement capabilities and seemingly low hydrodynamic drag of the shark, it was found that their skin had dermal denticles which aided low drag movement. The scales were aligned along the body from nose to tail, with each scale having a cross section multiple "u" shaped channels with a sharp tip. Becheret and Reif. (32) found that ridges in the dermal denticles interacted with the viscous sublayer resulting in skin friction drag. This led to the scalloped shaped riblets which mimicked the shape of the denticles closest.

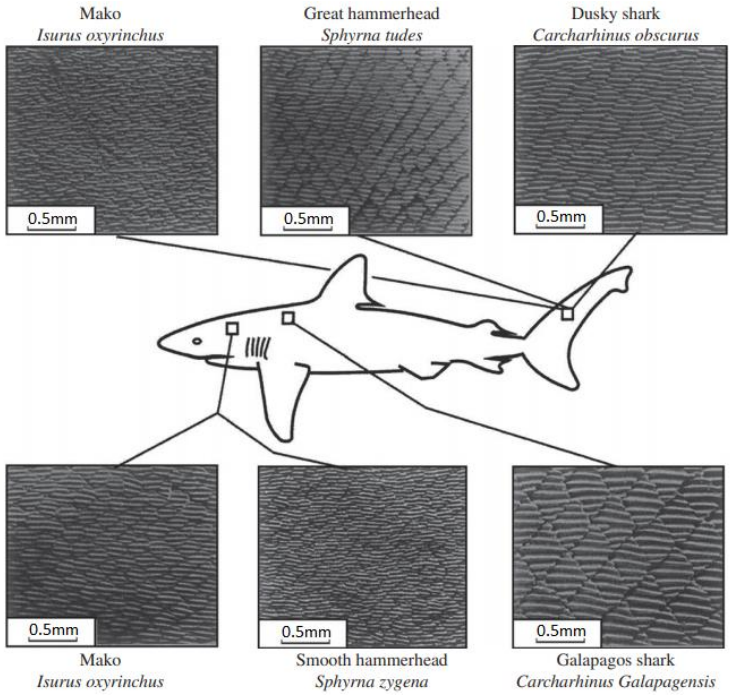

Figure 2.7 – Dermal denticle layout of fast swimming shark (modified from (32) (33))

In 1982, Walsh (34) conducted a wide scale wide scale study of the drag reduction capabilities of riblets with a v-shaped trough. By use of a momentum balance, it was concluded that they produced an 8% drag reduction when the height and spacing was optimised. The study also sought to understand the way that the turbulent changed by studying the burst frequency of the near wall vortices. It was found that whilst the burst frequency over the smooth and riblet surfaces remain unchanged, the turbulence intensity of the flow over the riblets was greatly reduced.

Hooshmand *et al.* (35) and Pulles (36) also studied the burst frequency and turbulent boundary layer characteristics over riblets - both noting an increase in burst frequency. Bacher and Smith (37) noted no marked difference in the burst frequency, whilst Gallagher and Thomas (38) saw a 30% reduction. Choi studies saw that the bursts were also reduced, and their restriction led to weaker bursts (39). The discrepancy between the bursting results was attributed to the difference in multiple factors such as sample rate, threshold levels and sample time. All of the studies did however agree that that for drag reducing riblets, the near wall turbulence intensity and local skin friction were significantly reduced.

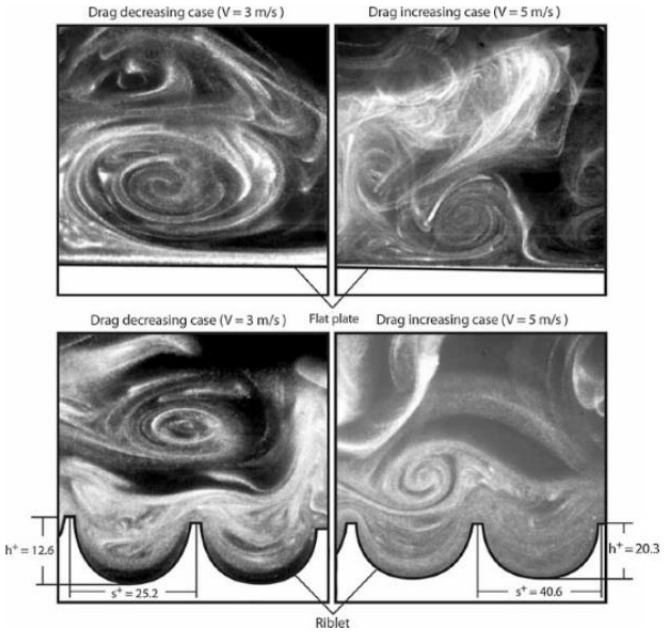

Figure 2.8 – Scalloped Riblet in a drag reducing and drag increasing scenario. Figure modified from Lee and Lee (40)

In 1983 Walsh (41) investigated different configurations of riblets and found that riblets with sharp peaks and round troughs were more effective at drag reduction than "inverted" riblets with sharp troughs and rounded tips. It was suggested that the low speed streaks in the sublayer were constrained in the troughs and restricted spanwise meandering, however Bacher and Smith (37; 42) reported that the streaks stayed above the peaks of the riblets in an organised way and increased the spacing between the near wall vortexes -this reduced their interaction. This was confirmed by the Choi (39) Lee and Lee (40), who also showed that not only were the vortexes smaller above drag reducing riblets in comparable flow to a flat plates, the riblets also impeded spanwise wavering across the surface.

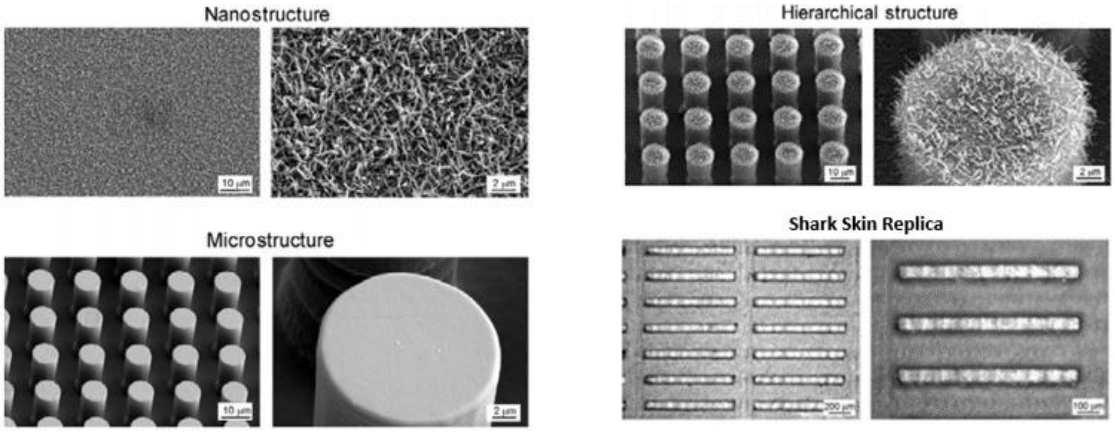

Figure 2.9 – Bio-inspired surfaces tested in the experiments. Adapted from Yong and Bhushan (43)

Yong and Bhushan (43) conducted experiments in air and water to investigate the drag reduction capabilities of biomimetic structures. The effectiveness of flat acrylic resin, shark skin replica (from a dogfish shark, Squalus ananthias, L, Squalidae) was measured by way of pressure drop across a channel. The study showed that in turbulent water flow the biomimetic nanostructure, microstructure and hierarchal structures surfaces, as seen Figure 2.9 produced a substantial reduction in pressure drop, with the hierarchal structure performing best. This was attributed to the superhydrophobic replication resulting in a lowest contact angle hysteresis. The replica shark skin produced around 30% less pressure drop in comparison to the epoxy surface. However, in the turbulent airflow the results were quite the opposite for the shark skin replica. Overall, it showed an increase in pressure drop by about 30%. This increase was attributed to the air flowing around the structures, creating vortices and increasing drag. This study was significant in the way of showing the surface texture mechanisms for producing drag reduction in air and water are very different, however the simple shape of the riblets are very effective in both.

Much work has been carried out into the shape and performance optimisation of the riblets. The classical shapes of riblets are 2D, meaning that each riblet is parallel to its neighbour and has a constant cross section throughout its length. V-groove (or sawtooth) riblets have been the most widely studied geometry, with by notable applications in wind turbines (Chamorro (44), Sareen (45)) and aircraft (Walsh and Lindemann (46), Walsh et. al (47), Szodruch (48), Zuniga *et al.* (49)) with positive drag reduction results.

An early instance of using blade type riblets to control the shear stresses in a boundary layer was by Sandborn (50) who glued 90^{o} brackets to the flat plate to form an array of equally spaced riblets. Walsh and Weinstein (51), who noted no overall drag reduction. Wand and Jovanovic noted a drag

reduction for riblets 5µm thick, and Bechert et al (52) used an adjustable ribbed plate to test optimisation for drag reduction and found a 9.9% reduction where the height, spacing and riblet thickness were optimised. El-Sammi *et al.* (53) used direct numerical simulation with blade riblets to produce a staggering 11% drag reduction. Whilst the results have been positive, the geometry is extremely fragile and cannot be used commercially.

A "happy medium" between the blade and sawtooth and blade riblets, is the trapezoidal groove riblet. Bechert *et al.* (52) found that whilst the blade riblets produced 9.9% drag reduction and sawtooth riblets produced 5.5%, the trapezoidal riblets produced 8.2%. They were more robust than the blades and offered better drag reduction than the sawtooth riblets. Kurita *et al.* (54) and Stenzel *et al.* (55) have been used by trapezium groove riblets on aircraft with positive drag reduction results, with the former using the popular 3M riblet film.

Chen *et al.* (56) cited up to 20% more drag reduction than traditional triangular riblets with a 3D herringbone structure, however works through extensive testing carried out by Bechert *et al.* (57) revealed that whilst the 3D riblets did provide drag reduction but were outperformed by 2D riblets.

$$s^+ = \frac{su_\tau}{\upsilon}$$

Equation 2.3

$$h^+ = \frac{hu_\tau}{\upsilon}$$

Equation 2.4

$$\ell_g^+ = \left(A_g^+\right)^{1/2}$$

Equation 2.5

By non-dimensionalising the spacing of riblets by the friction velocity and flow viscosity (Equation 2.3) from various studies of varying riblet configurations, a set of curves showing optimal riblet spacing with respect to height-spacing (h/s) ratio has been formed. The afore mentioned studies examining riblets have found that the optimal configurations were the same as those found on fast swimming shark, between $s^+ \sim 15 - 18$. (33) (58).

García-Mayoral and Jiménez (59) sought to find a method of scaling that would take into account the shape of the riblet, and therefore universally compare the drag reduction capabilities of riblets. They found that they were able to collapse the extensive drag reduction curves from curves of multiple geometries compiled by Bechert *et al.* (52) by scaling the area of the riblet groove using. The riblet scaling factor formulae is shown in Equation 2.5, and the collapsed curves shown in Figure 2.10. Drag reduction up to a riblet scaling factor of $\ell_g^+ \sim 16$ for most geometries, but the optimal riblet scaling factor occurs where $\ell_g^+ \approx 11$.

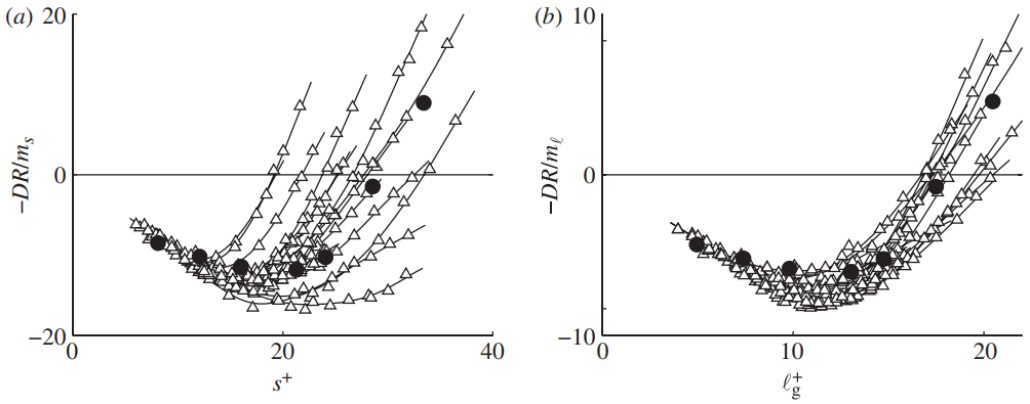

Figure 2.10 – Drag reduction curves of multiple riblet geometries a) expressed as a function of riblet spacing normalised by wall units, s^+, b) expressed as a function of area. Solid circles represent direct numerical simulations (DNS) by García-Mayoral and Jiménez (60)

The turbulent spot has been used as a tool to analyse the effect of riblets on the onset of turbulence such as Grek *et al.* (61) who found that the riblets delayed the amplification of the initial Tollmien-Schlicting wave to develop into a turbulent spot in comparison a smooth surface. A turbulent spot has also been used by Ancrum and Yaras (62) to determine the effect of the riblet spacing on the streak spacing and found that the wide spaced riblets kept the vorticies above the peak in such a way that they did not interfere with their neighbouring streak, unlike closely spaced riblets.

2.3.2. Large Eddy Break up devices

A Large Eddy Break Up devices (LEBU) is a passive device consisting of thin plate or airfoil placed into the outer region of the turbulent boundary layer. They are placed in such a way that the self-sustaining mechanism of momentum transport into the boundary layer are disrupted. The aim is to targeting large eddies in the boundary layer, breaking them up into smaller lower energy eddies that will eventually dissipate to viscosity as found by Yanjnik *et al.* (63) .

Honeycomb screens were investigated as a method of free-stream turbulence manipulator by restricting the lateral components of the flow turbulence was reduced, resulting in lower skin friction, c_f, downstream of the screen. However, there would be penalties due to the method that the screens are introduced to the flow.

Studies have been conducted by Hefner et al in 1979 (64) using a number of horizontal plates suspended over the flow surface so that there is interaction with the outer layer of the boundary layer.

Results showed that the skin friction was reduced by 24% over a length of 45 device heights, however this did not result in a net reduction.

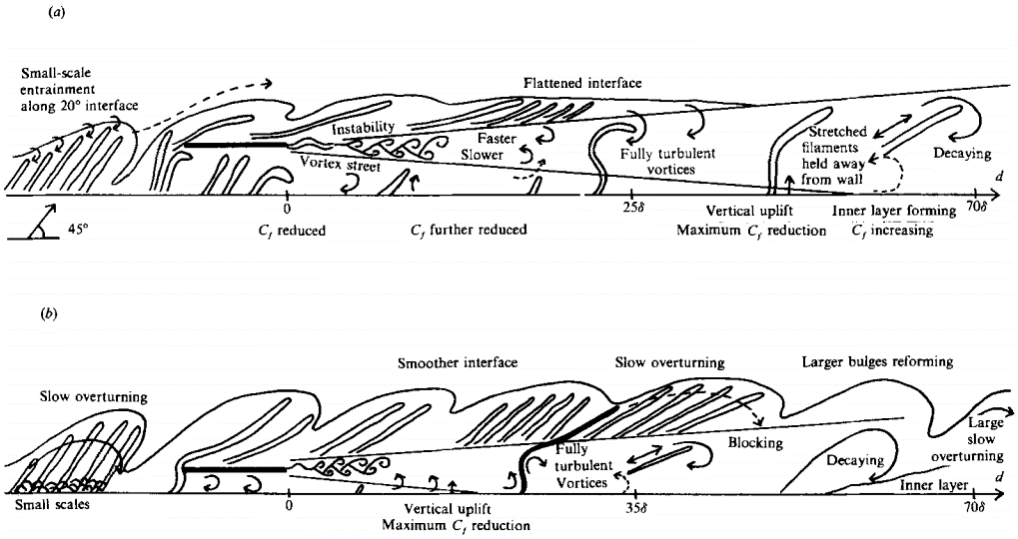

Figure 2.11 – Schematic representation of the LEBU boundary layer interaction based on flow visualisation results (65), a) single plate LEBU placed at 0.75δ at the LEBU leading edge boundary layer thickness, b) single plate LEBU placed at 0.25δ LEBU leading edge boundary layer thickness.

Savill and Mumford (65) used smoke wire and laser sheet to visualise the effect of the interaction between the boundary layer and the LEBU. The schematic is shown in Figure 2.11. It was found that the LEBU was very effective at reducing the skin friction for both LEBU configurations, but the where the LEBU was placed at 75% of the boundary layer height much outperformed its competitor.

2.3.3. Combined

In 1984, Walsh and Lindemann (46) placed riblets downstream of the LEBU to investigate the combined effect of the drag reduction devices. It was found that the combined effect was additive suggesting that the mechanics responsible for the drag reduction of each device individually, was independent of the other. A similar phenomenon was also reported by Gudilin *et al.* (66) who reported that a total of 16% skin friction reduction was achieved.

2.4. Noise and vibration

2.4.1. Lighthill's Acoustic Analogy: Turbulence as a source of sound

Until Lighthill's analogy in response to controlling noise from jet aircraft (67) (68), it was not possible to predict with any degree of accuracy what noise was generated from the fluid flow itself. The pressure fluctuations present in a flow could be the result of inflow structures interacting with a solid wall and causing vibrations to be propagated back into the flow, but Lighthill disregarded these effects, focussing solely on the fluid.

Derived from the Navier-Stokes momentum equations and mass momentum conservation, Lighthill's analogy successfully identified the exact source of the noise inside the moving fluid.

$$T_{ij} = \rho u_i u_j + p_{ij} - c^2 \rho \delta_{ij}$$

Equation 2.6

This analogy resulted in the second order differential equation called the wave equation, which expresses the propagation of the acoustic waves through the fluid with respect to position and time as (69):

$$\frac{\partial^2 \rho}{\partial t^2} - c^2 \nabla^2 \rho = \frac{\partial^2 T_{ij}}{\partial x_i x_j} + \frac{\partial q}{\partial t}$$

Equation 2.7

ρ = density, p_{ij} = compressive stress tensor, c = velocity of sound in fluid at rest, u_i is the velocity component in the direction x, y or z. Essentially, Lighthill shows that sound propagates in a moving fluid the same way it would in in as a stationary fluid that is acted upon by fluctuating stresses (70).

Chapter 3 Experimental set-up and methodology

This chapter describes the experiment set up and calibrations of the research tools. It also outlines the processes used for the manufacturing of individual test components, how they were set up, the data acquisition process probes, and the data processing technique.

3.1. Aerodynamic Wind tunnel

Experiments were conducted at Brunel University's aerodynamic wind tunnel. It is an open circuit suction-type tunnel, where the axial fan is driven by a 7.5kW motor capable of achieving velocity up to 35ms^{-1} in the test section. There are four 1.5m flat Perspex plates bolted together to form a single test section. The cross-sectional profile of the test section is square with dimensions of 0.5m x 0.5m.

At the inlet, the air passes through a honeycomb screen to straighten and streamline the flow before passing through a series of increasingly finer mesh screens. The screens serve to break down large scale turbulent eddies for the incoming flow in order to reduce the overall turbulence intensity of the main flow (63). The air is accelerated through a 3:1 ratio nozzle area contraction before reaching the test section. Inside the test section, the mean turbulence intensity of the flow was found to be between 0.4 – 0.6%.

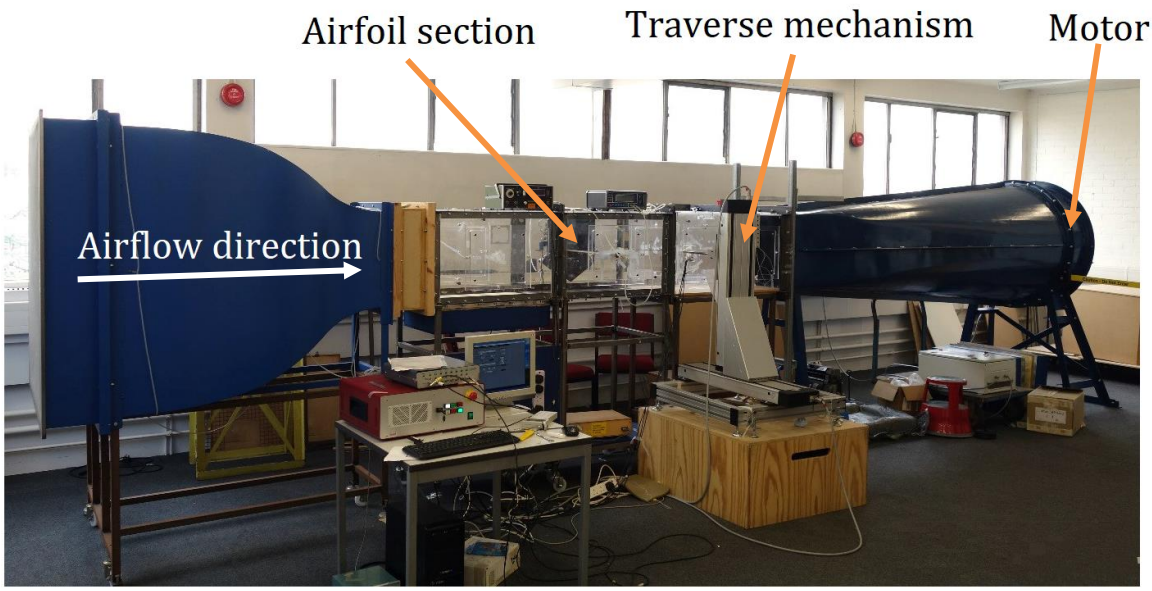

Figure 3.1 - Brunel University's Aerodynamic Open Circuit Wind Tunnel
[Photo courtesy of (12)]

After the test section, the air is expanded the diffuser, which is where the fan is housed. A photograph depicting the main components of the wind tunnel is shown in Figure 3.1.

3.2. Instrumented flat plate with trailing edge flap

Experiments were conducted on a flat plate which was designed and built in-house. It has an SLA (stereolithography apparatus) NACA0012 leading edge to facilitate a smooth entry of the flow to the flat plate and to the avoid the formation of a separation bubble at the leading edge.

The main frame of the flat plate is made up of a 20mm planed pine frame sandwiched between two sheets of 5mm thick Perspex on both sides of the flow surfaces. The frame was designed so that there were horizontal struts where the spaces between were packed with a dense 20mm foam. This gave the flat plate a more sturdy internal structure to prevent the Perspex from warping.

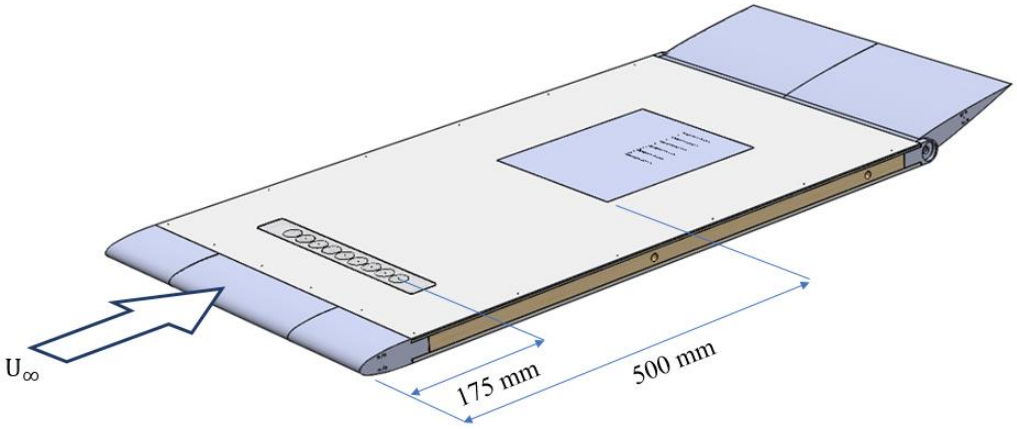

Figure 3.2 – Diagram of the instrumented flat plate with trailing edge flap

As shown in Figure 3.2, a removable strip at x = 175mm, where x = 0mm refers to the leading edge of the flat plate. This strip houses nine VISATON K23 8Ω 1W speakers which are used to generate artificial turbulent spots through a pinhole 1mm deep and 0.4mm in diameter (Section 3.5). The speakers are wired in series, which allows all nine speakers to be fired simultaneously. The centre speaker is also wired in a configuration that allows it to be used on its own as a single spot generator.

At x = 500mm, there is a 249mm x 209mm recess in the plate to house an interchangeable test plate. In this investigation, two types of plate were used. These will be further discussed in the following sections.

The trailing edge of the plate is a deflectable flap of the NACA0012 profile, where the maximum thickness is 30mm, corresponding to the overall thickness of the flat plate. The flap is connected by hinges at the rear of the plate. The flap serves to move the stagnation point to the upper side of the leading edge, supressing leading edge separation bubble to ensure a smooth boundary layer development over the upper flow surface. A similar plate design with trailing edge flap has been used successfully in other studies.

3.2.1. Interchangeable Baseline test plate

Two types of interchangeable plates were used in this investigation. The first plate is used as the baseline case, which is a smooth aluminium finish. The aluminium plate, which is 5mm thick, was manufactured accurately using a 3-axis CNC machine.

The plate consists of an array of pressure taps used for the unsteady pressure measurements. The taps on the flow surface of the test plates are approximately 0.4mm in diameter with extends to a depth of 1mm below the surface. These were counterbored with a 0.6mm diameter hole on the other side of the plate through the remaining 4mm depth. A 0.6mm diameter holes are connected by 6mm lengths of microbore brass tube with an internal diameter of 0.4mm, which were fixed into each hole with cyanoacrylate glue. Table 3.1summarisressure tap locations used in the current experiments.

Streamwise microphone number; Spanwise microphone number	Streamwise location of pressure tap from Flat Plate leading edge, x (mm)	Spanwise location of pressure tap from Flat Plate centreline, z (mm)
1; 1, 2, 3, 4, 5, 6, 7, 8	x = 625	0 0, 2, 4.2, 6.6, 9.2, 12, 15, 18.2
2	x = 627	0
3	x = 634	0
4; 1, 2, 3, 4, 5, 6, 7, 8	x = 645	0 0, 2, 4.2, 6.6, 9.2, 12, 15, 18.2
5	x = 655	0
6 1, 2, 3, 4, 5, 6, 7, 8	x = 665	0 0, 2, 4.2, 6.6, 9.2, 12, 15, 18.2
7	x = 685	0
8 1, 2, 3, 4, 5, 6, 7, 8	x = 725	0 0, 2, 4.2, 6.6, 9.2, 12, 15, 18.2

Table 3.1 – Locations of streamwise and spanwise pressure taps along with corresponding microphone number for the baseline riblet plate.

3.2.2. Interchangeable Riblet test plate

There are numerous methods of manufacturing riblets which include etching (71), laser machining (72), grinding (73) and micro-moulding (74) (75) (76) (77). Since we do not have the machining capability, 3D printing methods were explored in the current project. It is noteworthy that Wen *et al.* (78) successfully employed multi material 3D printing system to print a sheet of shark dermal denticles.

For the current study an Objet 30 Pro polyjet printer was used to trial the capabilities of jetted acrylic monomer. The test geometry is Sharklet Technologies Sharklet micro-pattern (79) scaled up by 100 times, shown in Figure 3.3. The figure shows several magnified view of the 3D printed sharklet

produced in the print trial. As can be seen, the individual geometries fuse together for the more compact sharklet configuration in Figure 3.3a, but the less compact one in Figure 3.3e is considerably better. The sharp boundaries have lost their resolution and become domed. This agrees with Wen *et al.* (78), who found that one of the major limitations of polyjet printing is that the dermal denticles lost intricate detail when printed at the original scale.

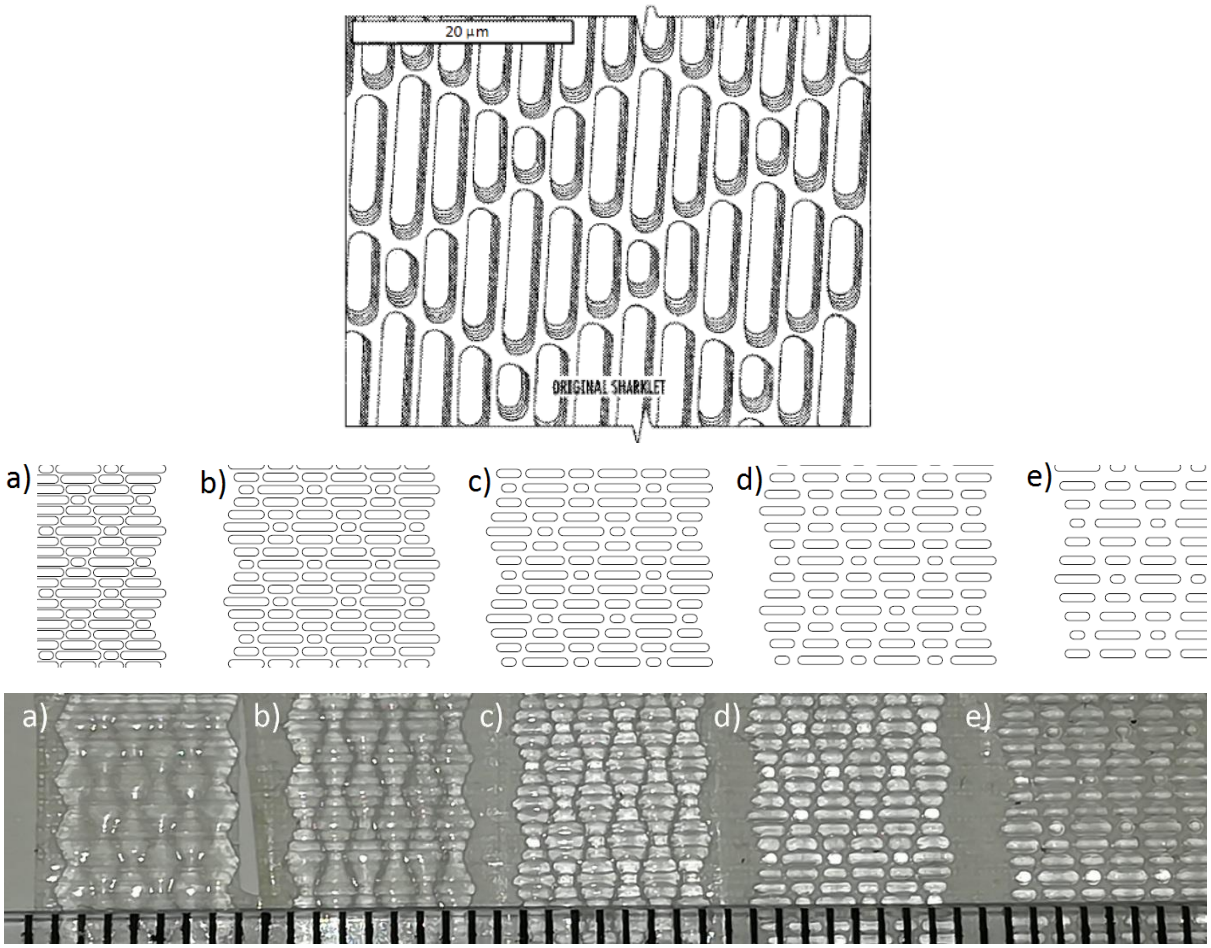

Figure 3.3 – Sharklet trial 3D print in the current project, (top) original Sharklet dimensions where micrograph represents 20µm, (middle) 2D sketch of printed Sharklets scaled up 100 times, (bottom) Polyjet printed geometry, where a) to e) represent 1x to 5x spacing and the scale is in mm.

SLA (stereolithography apparatus) 3D printing technique, as reviewed by Bhushan *et al.* (80), is found to have the best resolution and surface quality. Successful wind tunnel testing of SLA riblet models was reported by Stenzel *et al.* (55). Therefore, this method of rapid prototyping is adopted for this study.

The 3D Systems Viper Stereolithography system constructs geometries by lowering a part bed into a vat of photoreactive Accura® resin, which is then cured by a solid state Nd:YVO_4 laser with a beam diameter of 0.08mm. Before the part is started, there is a series of thin strategically placed 10mm high supports built to hold the part away from the surface of the part bed. In the high-resolution mode, the bed was lowered in steps of 0.02mm and resin flows previously cured layer. A blade is then passed over the surface to displace excess resin creating a level thickness, which is then cured by the laser. The vertical repeatability is within 0.0076mm, making the printing highly consistent from part to part. Once the part is completed, it will be removed from the machine and the uncured resin is washed off with isopropanol alcohol. After that it will be cured for a second time in a UV oven create a solid structure. The described process above represents the 3D printing method used to fabricate the Riblet geometry used in this study.

The dimensions for the Riblet are based on scaling with the turbulent boundary layer generated on a flat plate whose thickness, δ, and the skin friction coefficient, c_f, can be predicted by the 7th power law in Equation 3.1 and Equation 3.42 (81) (82).

$$\delta = 0.373x\ Re_x^{-1/5} \quad \textit{Equation 3.1}$$

$$c_f = 0.0592\ Re_x^{-1/5} \quad \textit{Equation 3.2}$$

$$\tau_w = \frac{1}{2}\rho {U_\infty}^2 c_f \quad \textit{Equation 3.3}$$

$$u_* = \sqrt{\tau_w/\rho} \quad \textit{Equation 3.4}$$

For the near wall properties such as the wall shear stress, τ_w, and the fiction velocity, u_*, the expressions are shown in Equations Equation 3.3 and Equation 3.4 respectively. Note that the dimensions were optimised for the printer limitations and quality, whilst retaining dimensions close to the designed parameters.

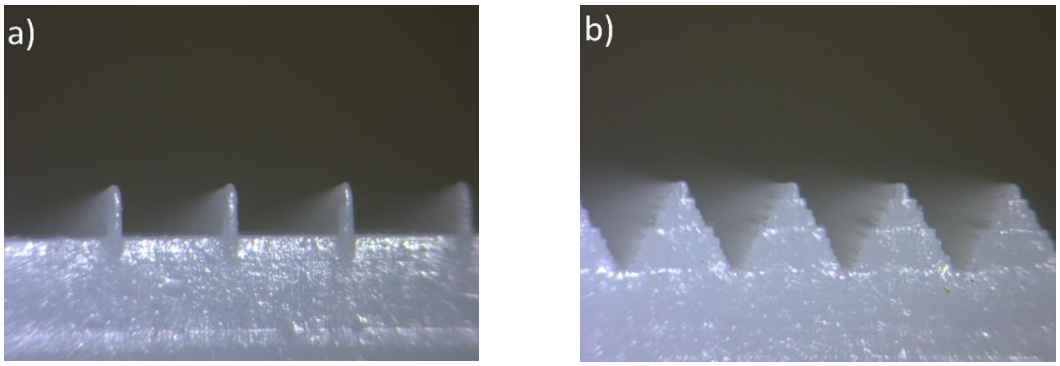

Figure 3.4 – a) Vertical blade riblets h= 0.32mm; b) Sawtooth Riblets h = 0.7mm

Initially, two geometries were to be used for the experiments in this study – vertical blade type riblet and a triangular (sawtooth) riblet, as seen in Figure 3.4a) and b) respectively. The vertical blades are

0.08mm thick and are found to be extremely fragile. The Sawtooth geometry is more robust, although drilling pressure taps into the surface plate means that the taps could compromise the integrity of the surface and could fall in different vertical locations of the individual riblets. Therefore, the trapezoidal grove riblets suggested by Bechert *et al.* (57) were used since they are more robust.

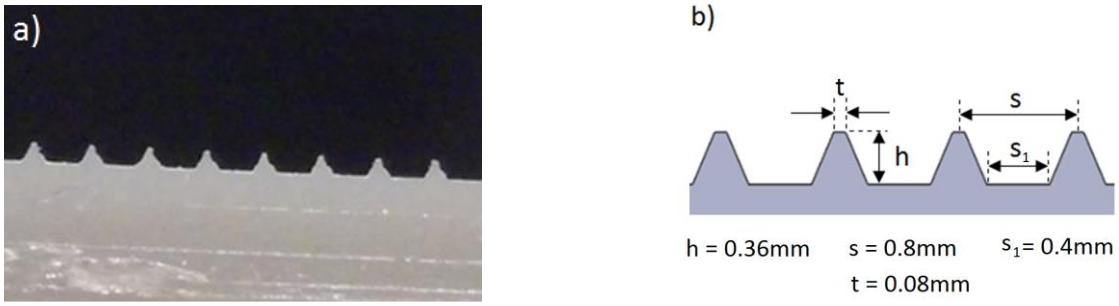

Figure 3.5 – a) 3D printed trapezoidal riblet profile dimensions; b) Riblet dimensions

The test plate that utilises the trapezoidal riblet profile has the same dimensions as the Baseline test plate, but the pressure taps in the spanwise direction are slightly different to ensure that each pressure tap falls equidistantly between the individual riblets. The profile and dimensions for the trapezoidal riblets used in this study are shown in Figure 3.5 and the pressure tap locations are tabulated in Table 3.2.

After the trapezoidal type riblet has been manufactured, it is then installed onto the flat plate where boundary layer measurements were conducted to determine the friction velocity, u_*, to obtain the non-dimensionalised s+, h+ and ℓ^+ as defined in Equation 2.3, Equation 2.4 and Equation 2.5 respectively, at freestream velocities U_∞= 10, 12 and 15m/s. From the preliminary boundary layer experiments, at 10m/s the Riblets are s^+ = 27.1 and h^+ = 12.2. The Riblet achieves a drag reduction parameter ℓ^+= 15.746. At 12m/s, the Riblet achieves s^+=31.9, h^+ = 14.3 and ℓ^+= 18.5. And lastly, at 15m/s the Riblet achieves, s^+=38.7, h^+ = 17.4 and ℓ^+= 22.5. Note that only one Riblet configuration is investigated in this study.

Streamwise microphone number; Spanwise microphone number	Streamwise location of pressure tap from Flat Plate leading edge, x (mm)	Spanwise location of pressure tap from Flat Plate centreline, z (mm)
1; 1, 2, 3, 4, 5, 6, 7, 8	x = 625	0; 0, 1.92, 4.48, 6.4, 8.96, 12.16, 14.72, 17.92
2	x = 627	0
3	x = 634	0
4; 1, 2, 3, 4, 5, 6, 7, 8	x = 645	0; 0, 1.92, 4.48, 6.4, 8.96, 12.16, 14.72, 17.92
5	x = 655	0
6; 1, 2, 3, 4, 5, 6, 7, 8	x = 665	0; 0, 1.92, 4.48, 6.4, 8.96, 12.16, 14.72, 17.92
7	x = 685	0
8; 1, 2, 3, 4, 5, 6, 7, 8	x = 725	0; 0, 1.92, 4.48, 6.4, 8.96, 12.16, 14.72, 17.92

Table 3.2 – Locations of streamwise and spanwise pressure taps along with corresponding microphone number for the trapezoidal riblet plate

3.3. LEBU

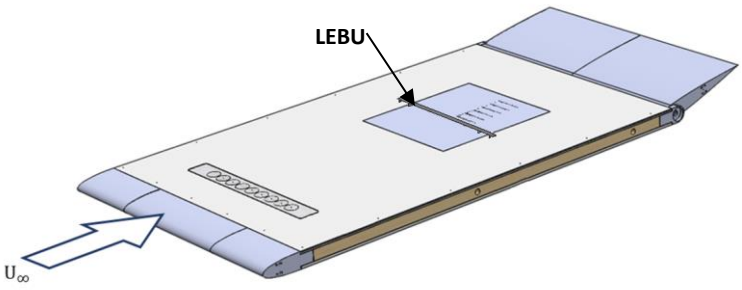

Figure 3.6 – Diagram of the LEBU installation

The LEBU used in this investigation is has a symmetrical airfoil cross-section of chord length c_{LEBU} = 15mm. The airfoil section chosen is the NACA0014 and has a thickness of approximately 2mm to provide a sturdy structure. The span of the LEBU is 300mm and is supported by plywood struts that are laser-cut from 0.5mm thick plywood and sanded down to be able to sit comfortably inside the 0.4mm trough between the riblet peaks. Two heights of struts have been used in this study, this first

raising the centreline of the LEBU to a height of 2.5mm above the surface of the flat plate, the second raising the centreline to 5mm. The struts were placed at the either end of the LEBU span to support the LEBU. A diagram if this is shown in Figure 3.6.

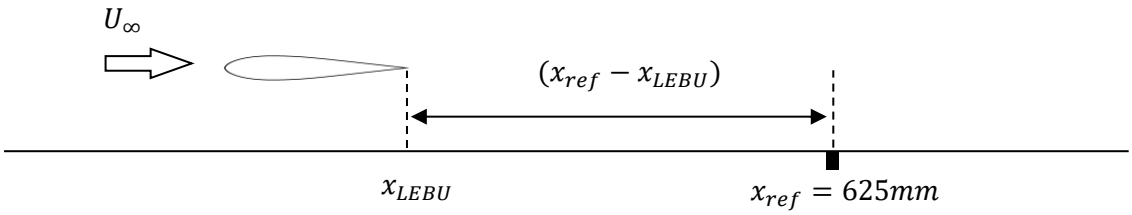

Figure 3.7 – Schematic describing the notation of LEBU location

The location of the LEBU is described in the Figure 3.7. The distance between the reference location and the LEBU is measured from the LEBU trailing edge. In Chapter 5, the LEBU measurements use this notation to describe the LEBU location as the LEBU is moved upstream of the reference location.

3.4. Unsteady surface pressure

3.4.1. Remote wall microphone set-up and measurement

Knowles FG3229-P07 electret microphones, which are circular (2.57mm diameter) with a sensing area diameter of 0.8mm, have been used successfully in previous studies for the unsteady wall pressure measurements (83) (84) (85). Therefore, the same electret microphone is used in this investigation along with a custom built 8-channel amplifier to measure the surface pressure fluctuations. These microphones are mounted remotely underneath the surface and are referred to as Remote Pinhole Probe, RMP. These microphones will predominantly be used for the auto-spectral, cross-correlation and coherence measurements of the wall pressure fluctuations.

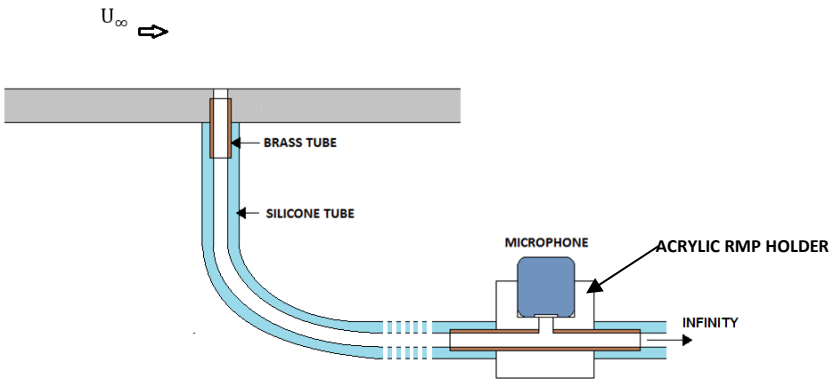

Figure 3.8 - Pressure tap and remote microphone configuration cross-sectional view

A schematic showing the RMP configuration is shown in Figure 3.8. The acrylic RMP holder has a 0.6mm diameter hole through the centre which houses the same type of brass tubing as that in the plate insert. The brass tube has a 0.4mm inside diameter and a 0.6mm outside dimeter. The connector that links the RMP diaphragm to the brass tube inside the acrylic block is 0.4mm and 1mm in length. A 40mm long silicone tube of 1mm outside diameter and 0.4mm internal diameter is used to connect the brass tube on the plate insert to the brass tube on the acrylic RMP holder, thus creating a continuous 0.4mm diameter section, 49mm long, from the pressure tap on the surface of the plate to the diaphragm of the RMP. The same type of silicone tube of about 3mm is connected to the other end of the RMP holder. The use of a long tube at the other end is to ensure that the acoustic waves travelling inside the RMP system does not encounter a sudden termination that will result in the backward reflection if this happens. Standing waves will be formed that could result in a fluctuation in the power spectral density. The current RMP configuration also ensures that the pinhole diameter will be constant up to the diaphragm of the RMP. This can avoid complications due to sudden area expansion.

It is also preferable for each tube connecting the plate surface to the RMP to be as straight as possible to minimise pressure loss. Due to the constraints of the plate being mounted inside the wind tunnel it is not possible to maintain a completely straight line throughout the RMP. Special care is taken to reduce of change for the curvature of the tube.

Corcos (86), Goody (87) and Schewe (88) highlighted that due to the finite surface of the pressure transducer sensing area, there are limitations in terms of signal attenuation at the high frequency. Over the years, the pressure transduces have become smaller in size, and are able to more accurately resolve the smaller length scale turbulence structures. However, for a microphone that features a circular sensing area, the sensitivity to the pressure fluctuations at the edge of the circular sensing area

will be less than at the centre. If a turbulence structure convects across an entire sensing area, some residue errors may be present in the acquired signals. To minimise this error, the pinhole on the surface that leads to the microphone underneath will focus only on the central region of the sensing are so that this edge of the sensing area remains unexposed to the turbulence pressure. This configuration can also ensure that the capability to resolve the smaller turbulence length scales.

3.4.2. RMP calibration

A Visaton FR8 10W full range speaker was used to calibrate each of the RMP in-situ. The Visaton FR8 has a near flat frequency response between 200Hz and 20kHz as shown in Figure 3.9a. It is attached to a cone that is designed to direct the sound pressure waves from a larger area to the other end of a smaller area. A similar calibration method was used by both Gruber (84) and Sagrado (83). In this method, a ¼" G.R.A.S reference microphone with a known frequency response is embedded in the wall of the cone near the surface as shown in Figure 3.9a. This allows the signal of the RMP and reference microphone to be measured simultaneously. The acoustic signal acquired by the reference microphone is assumed to be similar to the pressure fluctuation at the surface. It is essential to ensure that no leakage is present. An airtight seal between the contact areas of the cone and the surface is achieved around the contact area using putty.

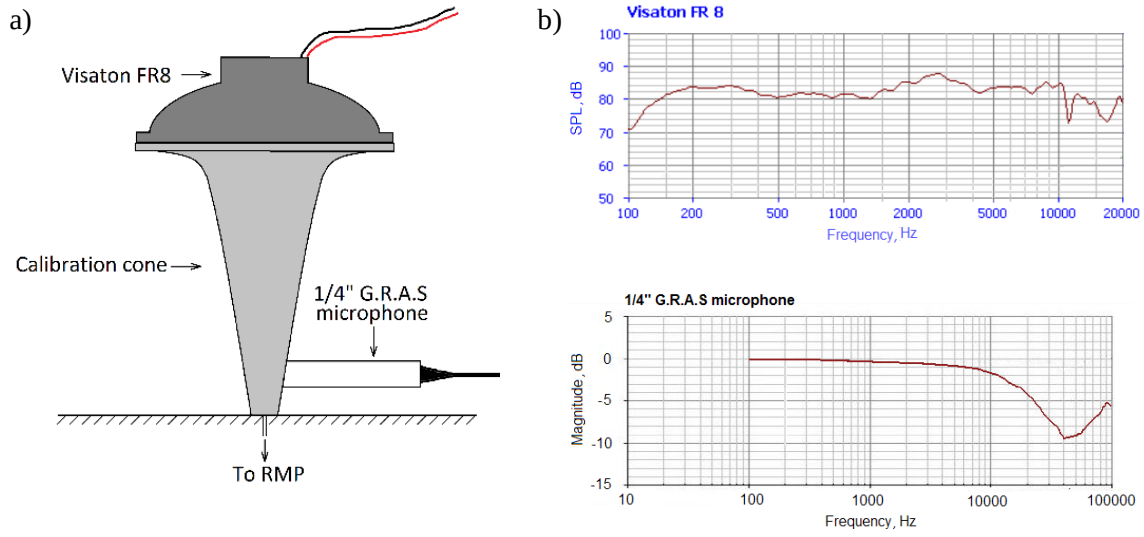

Figure 3.9 – a) Method to calibrate the each RMP in situ, b) Frequency response of the Visaton FR8 (top right), typical G.R.A.S frequency deviation from expectation according to the manufacturer (bottom right)

A transfer function is the ratio between the output signal and the input signal in the frequency domain. Therefore, multiplying an output signal by the transfer function, the original input signal can be recovered. To obtain the frequency response of the RMP, J_{RMP}, the acquired signal from the ¼" G.R.A.S microphone is used as the input signal , whilst the simultaneously acquired signal from the RMP is used as the output signal. A high definition white noise signal generated by SoX – Sound eXchange for Linux, is used to drive the loudspeaker. The definition of the transfer function, J_{RMP}, is described in Equation 3.5.

$$J_{RMP} = \frac{G_{E_{RMP}E_{ref}}(f)}{G_{E_{ref}E_{ref}}(f)}$$

Equation 3.5

Where the $G_{E_{RMP}E_{ref}}$ is the cross power spectral density between the RMP signal and reference microphone signal. $G_{E_{ref}E_{ref}}$ is the auto-spectrum signal of the reference microphone. This method also provides the phase information of each RMP used in the measurement of the surface pressure fluctuations over the frequency range of interest. Each RMP has its own unique transfer function based on its location. The transfer function is only applied up to 10kHz for the current study based on the flat frequency response curve of the reference microphone shown in Figure 3.9b. The calibration process was conducted for each RMP in situ. After the calibration process, the RMP microphones remain undisturbed for the entire experiment process. During the changeover of experiments, the RMP will then me reset and the aforementioned calibration process will be repeated again.

It is important to note that due to presence of the Riblets, calibrating the RMP in situ with the cone pressed against the surface above the pressure taps is not possible to achieve a perfect airtight seal. Therefore, calibration of the RMP was only performed for the Baseline plate. Nevertheless, the spatial distribution of the RMP between the baseline and the Riblet plate is the same. For this reason, the transfer function obtained for each RMP under the Baseline configuration can also be applied to the Riblet case.

3.4.3. Data sampling and processing

For the surface pressure measurements in the experiments, the raw data from each RMP was sampled at a rate of 40kHz for 15 seconds, which amounts to 600,000 samples. The data acquisition system has a 16bit resolution and each sampling channel has a built-in anti-aliasing filter.

Some examples of the power spectral density for a set of 8 RMPs subjected to three representative flow speeds are shown in Figure 3.10. From the spectra, there is a narrowband peak at approximately 6kHz, which remains present for all the flow velocities under investigation here. This implies that the noise source is unlikely originate from the flow, nor the fan itself since it would change the pitch frequency with rotational velocity. This narrowband component is likely generated static noise from the fan power source. The RMPs also show a significant dip at 7.5kHz. It is anticipated that under the velocity ranges that have been tested in this study, the majority of the small-scale turbulence structures would be adequately described by the spectrum at the frequency lower than 5kHz. To display the results as "cleanly" as possible, the wall pressure spectra in the following chapters will be presented between 200Hz and 5000Hz only.

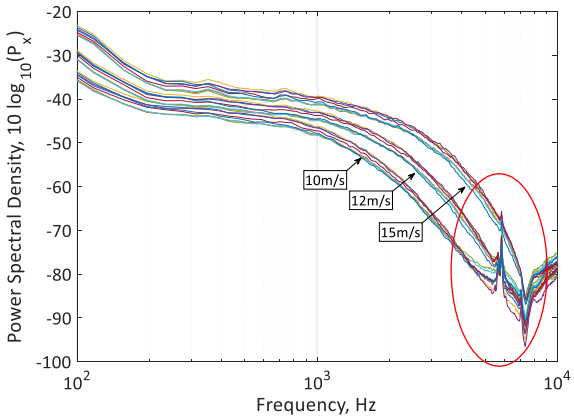

Figure 3.10 – Example of power spectral density for RMPs at 3 velocities.

3.5. Hot Wire Anemometry (HWA) measurement techniques and methodology

Hot wire measurements were carried out using a 3-axis TSI—ISEL traverse. The step motors of the traverse are capable of achieving very fine movement of 0.01mm as the smallest increment. The software used to control the traverse, calibrate and operate the hotwire probe, and data logging is the TSI Thermal Pro software. The analogue-to-digital (AD) card used in the HWA data acquisition has an 8-channel input with 12-bit resolution. In this investigation, the Dantec 55P11 miniature single wire probe is used to measure the flow velocity fluctuations. This hot wire probe consists of a 5µm diameter tungsten sensing wire and is 1.25mm long. The probe is specifically designed to be used in air. The overheat ratio of the hot wire is set to 1.8, which will give rise to an operating temperature of the hot wire becoming approximately 300ºC.

3.5.1. Hot wire calibration

It is necessary to calibrate the hot-wire probe. The calibration is aided by a pitot-static tube which is used to measure the mean velocity from the difference in the total pressure and static pressure. The pressure difference is measured by the Furness Controls FCO510 manometer. During each calibration, the hot wire probe and pitot static tube are raised by about 100mm from the flow surface, this vertical displacement will ensure that the both probes are outside of the boundary layer. The hot wire probe is placed in line with the static ports of the pitot-static tube, at a separating lateral distance of about 40-50mm to ensure that both probes are not interfering with each other.

It should be noted that the ambient temperature and atmospheric pressure are constantly monitored to provide an accurate air density value that is needed to calculate the velocity from the pitot static tube. The constant monitoring of the ambient temperature, especially during the hot wire calibration, is essential. This is because the resistivity of a hot wire will shift with ambient temperature. Therefore, a voltage-velocity curve obtained during a calibration on a particular day will not be accurate on another day when the ambient temperature could be different. In other words, as the ambient temperature drifts it will affect the velocity of the flow. It is possible to minimise the error in the velocity measurement by conducting correction during the post processing stage. From the method described by Bearman (89) and Jørgensen (90):

$$E = E_{acq} \cdot \left(\frac{T_w - T_0}{T_w - T_a}\right)^{0.5}$$

Equation 3.6

Where E is the corrected voltage, E_{acq} is the voltage acquired by the probe, $T_w$is the operating temperature of the wire, T_0 is the ambient temperature during the calibration, and T_a is the ambient temperature during the measurements.

The following paragraph will describe the hot wire calibration procedure.

Starting from 0m/s, the velocity of the mean flow is increased incrementally up to about 20m/s. Once the velocity has been steadied for each calibration point, the voltage measured by the hot wire will be digitised. At the end of the calibration, the acquired voltage, E_{acq}, is plotted against the velocity, u. An example of the calibration curve is shown in Figure 3.11, from which a 4th order polynomial curve fit is applied. The coefficients $C_1 – C_5$ in Equation 3.7 can then be determined. During the post processing after the hot wire experiment, the acquired voltage E_{acq} will be substituted to Equation 3.6

to convert to the corrected voltage. *E*, which will then be substituted into Equation 3.7 to calculate the instantaneous velocity.

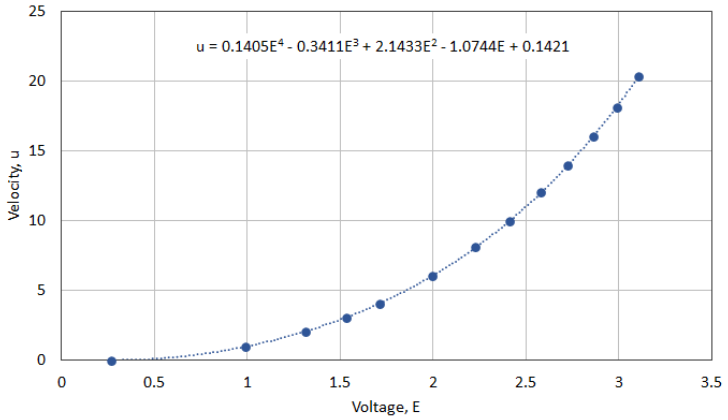

Figure 3.11 - Example of calibration curve for the Dantec 55P11 probe with the 4th order curve fitting equation

$$u = C_1E^4 + C_2E^3 + C_3E^2 + C_4E + C_5$$

Equation 3.7

To use the hot wire to measure the boundary layer accurately, it is important to determine the vertical distance between the hot wire probe and the wall surface. To set the probe height at an appropriate close vertical distance to the surface, a 0.3mm feeler gauge was used.

Once it is placed on the surface, the probe will gradually be lowered down until it just touches the surface of the gauge. The probe is then raised, the gauge is removed, and the probe is moved back to the gauge height. The traverse is then programmed to take the 0.3mm gauge height as the reference height, and then moved down by 0.15mm for the first measurement. This makes the nearest height approximately 0.15 mm above the surface. It is estimated that the margin of error in this method is in region of $\pm$0.1 mm.

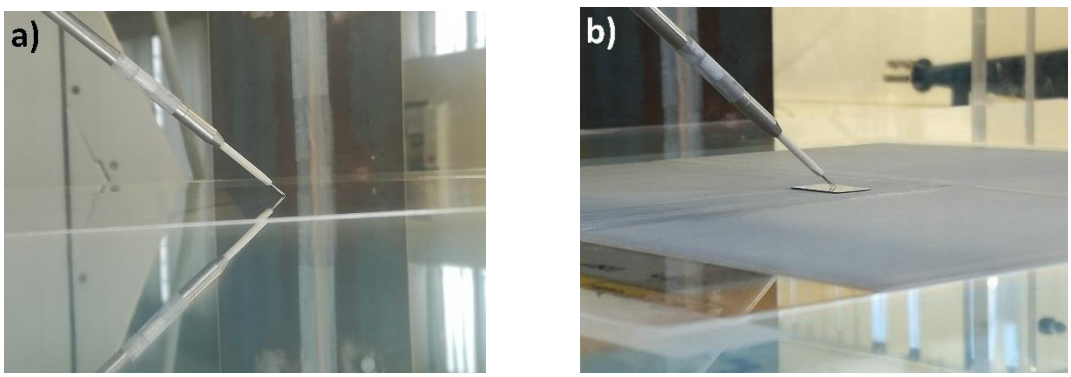

Figure 3.12 – a) Hotwire probe proximity to Baseline flow surface, b) Hotwire probe proximity to the gauge over riblet flow surface

3.5.2. Data sampling and processing

For the data acquisition in the experiments, the hot wire signal is sampled at a rate of 20,012Hz for 13 seconds, which results in 260,156 samples for each measurement point. The low-pass filter used in the data acquisition is set to 10kHz, which is equal to half of the sampling frequency. This is to ensure that the sampled signal is inside the Nyquist frequency and is not contaminated by aliasing and high frequency roll-off.

The mean velocity of each measurement point, and the turbulence intensity, are calculated by Equation 3.8 and Equation 3.9 respectively, where u' is the r.m.s of the velocity, *u*.

$$u = \frac{1}{N}\sum_{i=1}^{N} u_i$$

Equation 3.8

$$\frac{u'}{U_\infty} = \frac{\sqrt{\frac{1}{N}\sum_{i=1}^{N}(u_i - u)^2}}{U_\infty}$$

Equation 3.9

3.6. Turbulent spot

As mentioned earlier, a strip of loudspeakers housed in the plate is located at *x* = 175mm. The acoustic wave generated by the loudspeaker is used to trigger the laminar boundary layer and generate turbulent spots, first used by Gaster and Grant (91). The triggering pulse signals are generated by a Teledyne T3AFG10 function generator, that is connected to the centre loudspeaker. The pulsed signals are 4Vpp (4volt peak to peak) square waves with a 1ms duration at a frequency of 3 Hz. To verify the consistency of the generated turbulent spots, a hot wire was positioned at around 0.15mm from the flow surface at *x* = 625mm. Both the pulsed input signal and the hot wire signal are monitored with a Tektronix TDS 2014B oscilloscope. The hotwire probe was located in the centre span of the plate corresponding to the plane of symmetry of the turbulent spot.

Screenshots of the function generator interface and oscilloscope showing signatures of three turbulent spots are shown in Figure 3.13. A figure of the measured hot wire signal for a single turbulent spot between two pulse signals is shown in Figure 3.14. By using the trace function on the oscilloscope, the real-time individual instances of the turbulent spot can be overlaid to ensure that they are produced consistently and follow the same trend in terms of spot shape, size and arrival time.

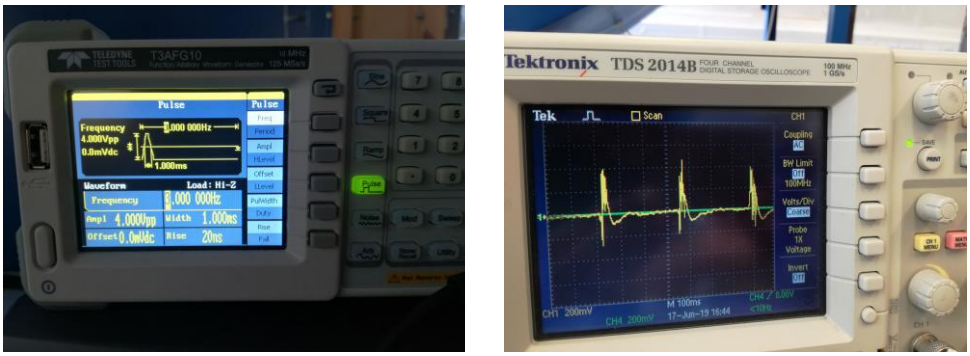

Figure 3.13 – The function generator used drive the loudspeaker, producing a disturbance in the laminar boundary layer that developed into a turbulent spot downstream (left), the hotwire signal displaying the passage of the turbulent spot at the probe location (right).

Initially, the pulses were generated at a frequency of 7Hz. However, by observing the signals on the oscilloscope, it was determined that the turbulent spots were interacting with each other. The calmed region that follows the passage of each turbulent spot did not fully return to the laminar starting condition before the next turbulent spot arrives. This can be easily corrected by reducing the pulse frequency to 3Hz. This spot generation frequency is confirmed as the ideal value to ensure the spot interaction does not occur. It is also an ideal value to ensure that the sampling time at each measurement location does not need to be excessive.

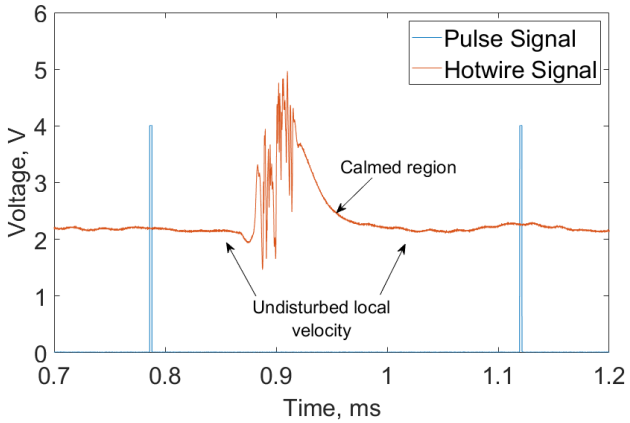

Figure 3.14 – Measured speaker pulse signal and turbulent spot signal on the hotwire probe.

The data analysis of the turbulent spot in this thesis relies heavily on the ensemble averaging technique. To perform the ensemble averaging successfully, the measured velocity needs to be separated into individual turbulent spot instances as shown in Figure 3.14 as an example. To perform this, the rising edge of each pulse signal is set as the time origin. An example of a post-processed turbulent spot is shown in Figure 3.15 with a turbulent spot measured by Cantwell *et al.* (26) for

comparison. Further discussion of the data analysis technique can be found in the instance in the next section.

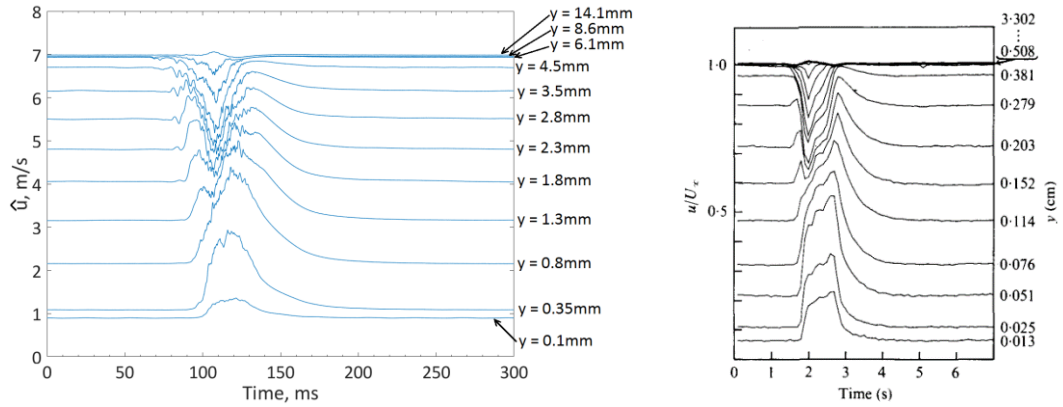

Figure 3.15 –Ensemble averaged measured velocity of experiment turbulent spot (left), ensemble averaged velocity from Cantwell et al. (26)

3.6.1. Data sampling and processing

The turbulent spots are sampled at a rate of 20,012Hz for approximately 26.2seconds, making each measurement point an average of 524,288 samples, N. The almost doubling of sampling time in comparison to the tripped boundary layer case in Section 3.4 is to endure that each measurement contains adequate individual turbulent spot signatures (approximately 78) for the ensemble averaging. The velocity is reduced by the same method as in Equation 3.8 and Equation 3.9. .

$$\tilde{u}(x,y,t) = \frac{\hat{u}(x,y,t) - u_{laminar}(x,y)}{U_\infty(x)}$$

Equation 3.10

$$u' = \frac{\sqrt{\frac{1}{N}\sum_{i=1}^{N}[u_i(x,y,t) - \hat{u}(x,y,t)]^2}}{U_\infty}$$

Equation 3.11

The local ensemble averaged velocity is given by $\hat{u}$. Before the arrival of the turbulent spot, the undisturbed boundary layer is laminar is denoted by $u_{laminar}$, whereas the local ensemble average velocity of the turbulent spot is given by $\hat{u}$. The ensemble averaged velocity perturbations can then be defined as per Equation 3.10 where U_∞ represents the freestream velocity. Note that the velocity perturbation is related to the momentum excess or deficit with respect to the turbulent spot. Another parameter that can be described from the ensemble averaging is the r.m.s velocity fluctuation which is given by Equation 3.11. Essentially, the r.m.s velocity fluctuation is the same as the turbulence intensity.

Chapter 4 The effect of Riblets

4.1. Introduction

This chapter comprises of two sections. The first (Section 4.2) presents some statistical boundary layer mean properties where the boundary layer near the leading edge of the flat plate is either artificially and instantly tripped into fully turbulent, or at least a bypass transition is triggered where a fully-developed turbulent boundary layer can be achieved at the measurement locations downstream. The turbulent properties produced by the artificial tripping will be time-invariant at the fully turbulent stage (i.e. the intermittency ≈ 1), which would allow a meaningful Fourier Transforming of the velocity or pressure fluctuation time signal to produce the Power Spectral Density for analysis to be performed in the frequency domain. In addition, standard time domain analysis techniques such as the mean, standard deviation, auto/cross-correlation can also be performed. Analysis from both the time and frequency domains will enable a wide perspective when comparing the untreated (Baseline) surface to that of the treated (Riblet) surface. The study will provide insights into how the Riblet might affect the turbulent boundary layer characteristics, such as the turbulent skin friction, turbulence production, and unsteady wall pressure power spectral density, the latter of which can be further exploited to provide additional insight into the aeroacoustics radiation. In other words, though the experiments in the first section are conducted on a flat plate, the results can provide a hint of how the application of surface treatment in the form of Riblet might affect the far field noise radiation pertaining to the aerofoil trailing edge self-noise.

The second (Section 4.2) part of this chapter will focus on the spatial and temporal development of turbulence in the form of *turbulent spots* on the flat plate subjected to both the baseline and surface treatment by Riblet. Unlike the previous case, the boundary layer tripping at upstream is done differently. Instead of using a passive tripping device like a zig-zag turbulator, controlled disturbance to the boundary layer is done only at a point, and also periodically with a constant time interval. The ensuing turbulent spots will then grow in the streamwise, spanwise and heightwise directions as they propagate downstream in an otherwise laminar boundary layer background pertaining to the flat plate. This characteristic allows an ensemble-averaging analysis technique to be performed to enable the monitoring of the spatio–temporal variations in the velocity perturbations and root-mean-square velocity fluctuations of the turbulent spots when passing over either a baseline or Riblet-treated surface.

4.2. "Stationary" Turbulent Boundary Layer – analysis based on the mean and turbulent velocity profiles

The following sub-sections discuss the results gained from the time-domain analysis of the tripped turbulent boundary layer experiments for their mean and turbulent velocity profiles. The measurement campaign includes experiments conducted at three freestream velocities, U_∞ = 10m/s, 12m/s and 15m/s. Although the variation in freestream velocity is not very significant, they are still expected to produce discernible differences in the boundary layer characteristics that could facilitate a study of the sensitivity of the Riblet's geometrical height to the skin friction and turbulence productions. In the current case, only one Riblet geometry is investigated.

4.2.1. Boundary layer integral parameters

The velocity profiles over the test plate surfaces were measured based on the methodologies described in Chapter 3. Despite the freestream velocity (upstream of the flat plate's leading edge) being set to 10m/s, 12m/s and 15m/s, respectively, a slight acceleration of the velocity potential across the flat plate surface is expected due to the growth of the boundary layer at the ceiling of the wind tunnel. This can normally be mitigated by tilting either the flat plate or the wind tunnel ceiling slightly to re-adjust the streamwise pressure gradient back to zero. However, modification of the current wind

tunnel ceiling is not a straightforward task. The flat plate, which is mounted in the centre of the wind tunnel, is deliberately aligned to the ground level in order to simplify the automated hot wire measurement procedure for the boundary layer profiles at different streamwise locations. Nevertheless, the level of flow acceleration is not expected to be significant in the current case. In addition, to ensure that the results at each streamwise location can be compared, the boundary layer velocity profiles will be normalised by the local freestream velocity.

The boundary layer thickness, δ, is described as the wall normal height at which the velocity becomes 99% of the freestream velocity, or $0.99U_\infty$. It can be obtained directly through analysing the velocity profile of the measured boundary layer, shown in Equation 4.1:

$$\delta = y_1 + (0.99U_\infty - \left(\frac{u_1}{U_\infty}\right)) \frac{(y_2 - y_1)}{\left(\frac{u_2}{U_\infty}\right) - \left(\frac{u_1}{U_\infty}\right)}$$

Equation 4.1

where y_1 and y_2 are the wall-normal distances below and above the δ, respectively. Similarly, u_1 and u_2 are mean velocities measured at y_1 and y_2, respectively. The U_∞ is determined by seeking and corresponding to the y location in which $\partial u/\partial y \approx 0$.

For the Baseline case, the no-slip condition determines that the lowest velocity should occur at the wall surface, where $u = 0$ at $y = 0$, which is considered as the "origin". For the Riblet case, the point at which the turbulent boundary layer begins from the surface is less straightforwardly to be defined. Due to the physical size of the hot wire probe, it is unable to reach the lowest part of the Riblet surface, i.e. the valley region between each peak, and measure the local velocity accurately. In other words, the nearest y location that a hot wire probe can reach is at y location higher than the peak of the Riblet. This presents a dilemma of defining the "origin" pertaining to a Riblet, where $y = 0$ could either be at the valley (i.e. the same as the Baseline case), or at the peak, or at a particular vertical distance between the valley and the peak. Figure 4.1a shows the boundary layer velocity profiles of the same location measured by the hot wire for both the Baseline and Riblet cases, where the latter is taken the Riblet valley as the origin where $y = 0$. The mismatch between the boundary layer profiles is unlikely to be solely attributed to the effect of the Riblet.

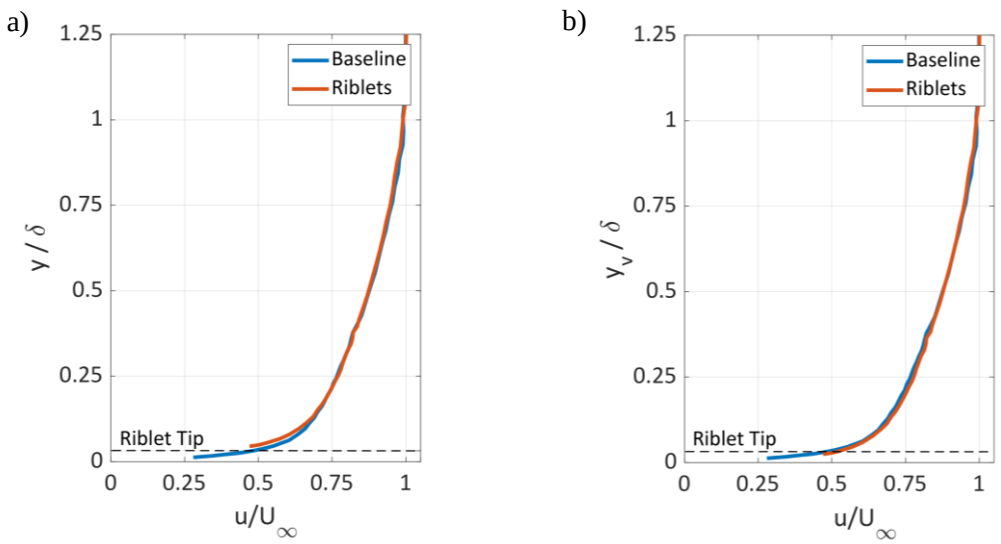

Figure 4.1 – Mean velocity profile above the Baseline and Riblets at 625mm downstream (a) taking the Riblet valley/trough of the Riblet curve as reference point, and (b) taking the virtual origin of the Riblet curve as reference.

In the current study, a concept of the "virtual origin" is instead used. As reported by Bechert (92), there is no universal definition of a virtual origin location because it is dependent on the Riblet geometry such as the riblet height, *h*, and riblet spacing, *S*. The virtual origin for this study has been found by matching the non-dimensional mean streamwise velocity profile over the Baseline and the Riblets, a method used by Lee at al. (40). This involves aligning the point at which the velocity becomes 99% of the freestream velocity, $0.99U_\infty$, over the Riblets to the point where the velocity reaches $0.99U_\infty$ over the Baseline and subtracting the vertical shift obtained. For the turbulent boundary layer over the Riblets in this study, the virtual origin is located at around $0.66h$ below the riblet tip. After performing this adjustment, the boundary layer profiles between the Baseline and Riblet are shown in Figure 4.1b and this time they are much better correlated. It should be noted that from this point forward, all the Riblet measurements are taken reference to this value of the virtual origin unless otherwise stated.

$$\delta_* = \int_0^\delta \left(1 - \frac{u}{U_\infty}\right) dy$$

Equation 4.2 – Displacement Thickness (13)

$$\theta = \int_0^\delta \frac{u}{U_\infty}\left(1 - \frac{u}{U_\infty}\right) dy$$

Equation 4.3 – Momentum Thickness (13)

Other parameters that can be used to describe the boundary layer are the displacement thickness (Equation 4.2) and momentum thickness (Equation 4.3). Apart from providing quantitative variations

of the turbulent boundary layer characteristics when subjected to the Riblet surface, they can also be used as, for example, the frequency scaling parameter in the power spectral density.

4.2.2. Mean Velocity Profiles and Turbulence Intensity Profiles

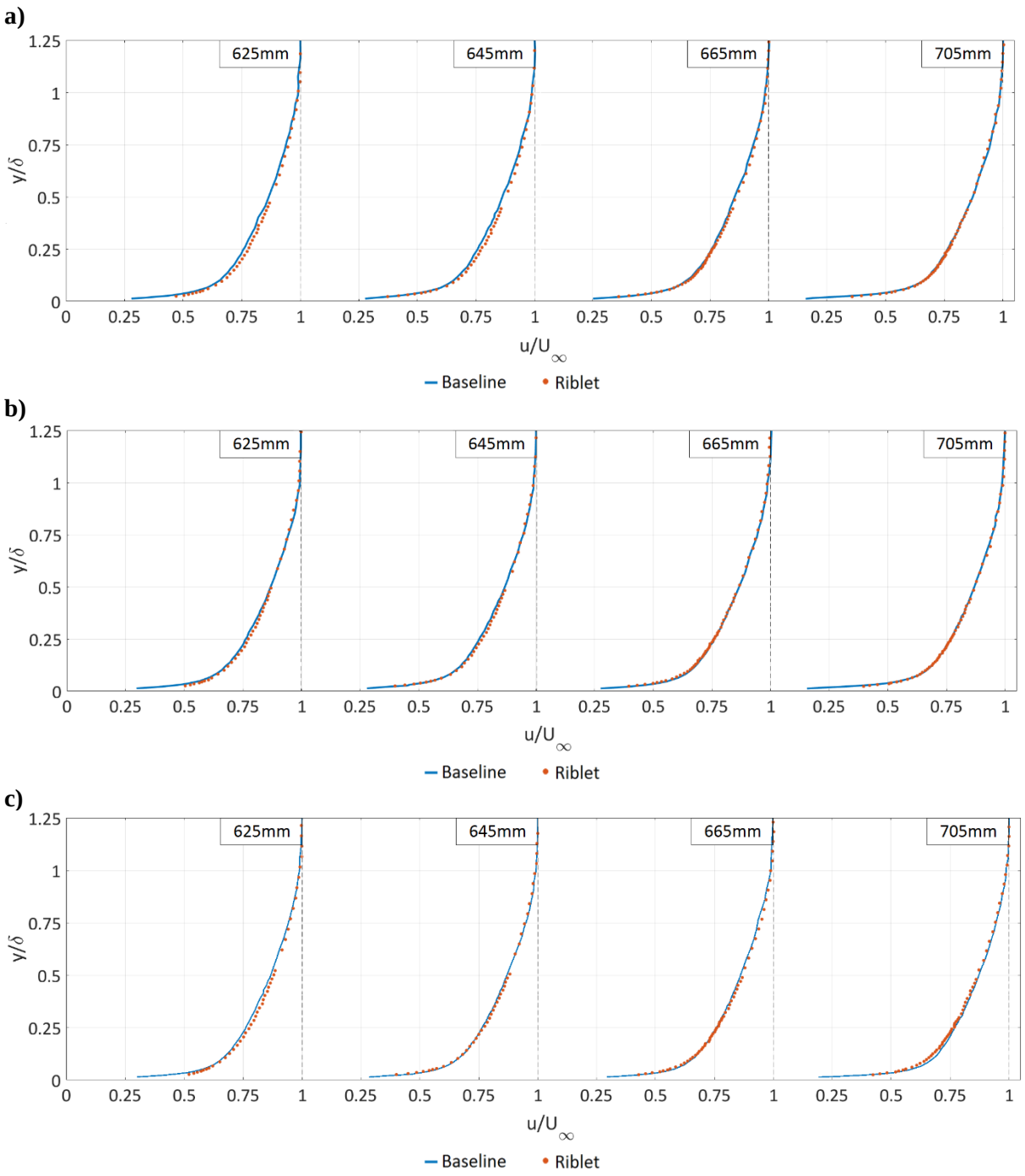

Figure 4.2 –Turbulent boundary layer non-dimensional velocity plot at various downstream locations for a) 10m/s, b) 12m/s and c) 15m/s

Figure 4.2 presents a summary of the streamwise development of boundary layer velocity profiles on the flat plate surface for the Baseline and Riblet cases at U_∞ = 10, 12 and 15m/s. The wall-normal distance y is non-dimensionalised by the local boundary layer thickness, δ, while the measured velocity is non-dimensionalised by the U_∞. This approach allows a meaningful comparison of the Baseline and Riblet boundary layer profiles and gives an indication as to the relative development of the boundary layers. A comprehensive boundary layer parameters for each of the measurement location, including the skin friction coefficients, are provided in Table 4.1.

As a reminder, the values quoted for the streamwise distances, x, in the figure are measured from the leading edge of the flat plate. The Riblet treatment is located at $500 \leq x \leq 710$mm. The first measurement point for the boundary layer profile is at x = 625mm, followed by x = 645mm, 665mm and 705mm. These four locations are situated within the Riblet surface.

At first glance, the boundary layer profiles for the Baseline and Riblet are not significantly different against each other. In the near wall region of the mean velocity profiles, both display a large velocity gradient $\partial u/\partial y$ at $y/\delta < 0.1$, which is an indication of the dominant effect of the viscous sublayer pertaining to a turbulent boundary layer where the velocity is predominantly affected by the turbulent fluid viscosity. A closer examination of the boundary layer profiles, especially those at x = 625mm, does reveal a subtle difference at the near wall region for the U_∞ = 10m/s, 12m/s and 15m/s cases. It appears that the mean velocity is higher for the Riblets case than the Baseline in the near wall region. Although any interpretation underpinned by such a small difference should exercise some cautions because the discrepancies could be within the margin of error, some physical explanations attributed to a change in the viscous effect in the near wall region could also be a possibility.

At U_∞ = for 10m/s (Figure 4.2a), the Riblets display an acceleration of the flow outside the viscous sublayer at x = 625mm and 645mm, but gradually displays similar velocity profiles as the Baseline case at x = 665 and 705mm. The same behaviour applies to the other freestream velocity cases in U_∞ = 12 and 15m/s. Overall, the difference of boundary layer profiles between the Baseline and Riblet is marginal. Further analysis underpinned by the mean velocity boundary layer profile will be conducted in later section in the context of skin friction coefficient. Next, the analysis will focus on the boundary layer turbulence intensity profiles.

a)

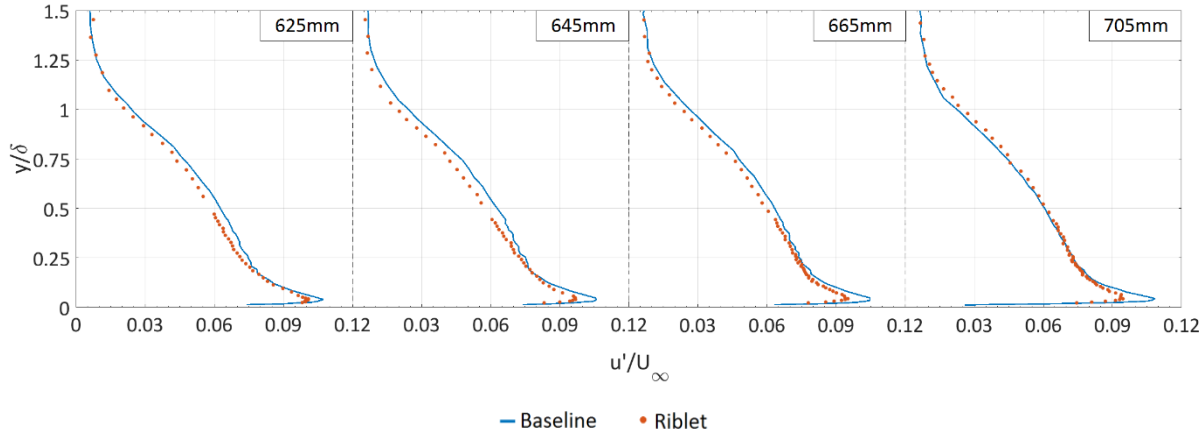

b)

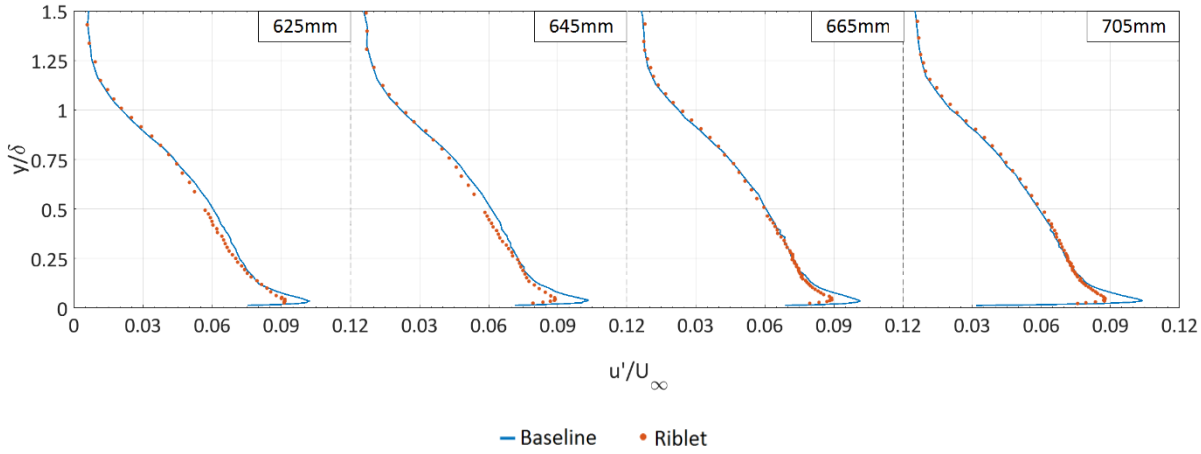

c)

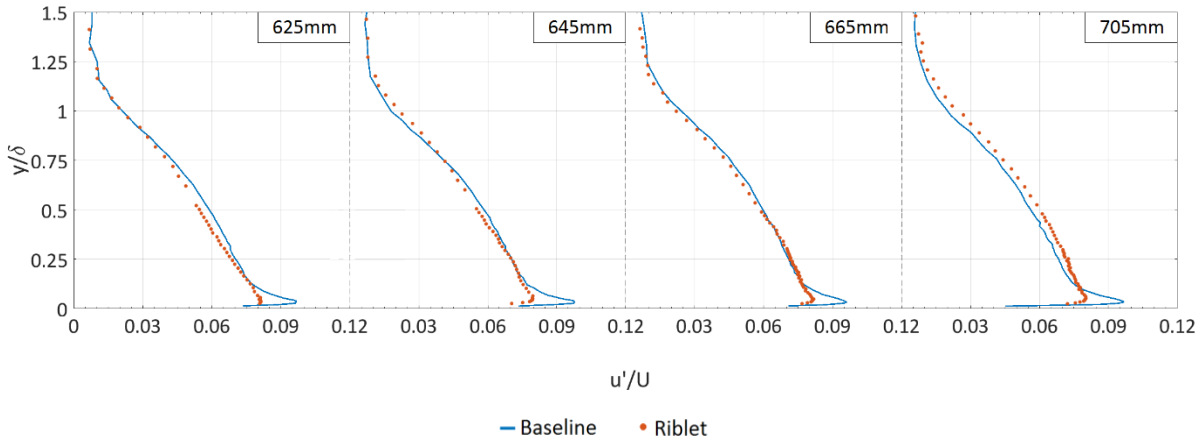

Figure 4.3 –Turbulence intensity for various streamwise locations Figure 4.3a) 10m/s, b) 12m/s and c) 15m/s.

Figure 4.3 shows the turbulence intensity u'/U_∞ boundary layer profiles for both the Baseline and Riblet cases. It is plotted against the non-dimensionalised height to compare the changes in turbulence intensity relative to the location inside the boundary layer. Unlike the mean velocity counterparts, the turbulence intensity profiles between them show discernible differences at $625 \leq x \leq 705$mm across the freestream velocities investigated here.

For the Baseline plots in Figure 4.3a, where U_∞ = 10m/s, the turbulence intensity plots develop as would be expected for a turbulent boundary layer. The turbulence intensity reaches a peak of $u'/U_\infty \approx 11\%$ in the near wall region and decays to between 0.4 and 0.6% in the freestream. The location of the maximum u'/U_∞ is generally located at $y/\delta \approx 0.05$, which is also likely to be the location where the maximum turbulence production occurs. Below this height, the turbulence level is dissipated by the viscosity effect. Another trend discernible is that, as U_∞ increases, the maximum level of u'/U_∞ also decreases (Figure 4.3b and 4.3c).

Interestingly, when the turbulence boundary layer profiles are compared against the Riblet case, the Riblet consistently exhibits a clear reduction in the turbulence intensity level at the near wall region. For example, for U_∞ = 10m/s at x = 625mm, the Riblet produces a reduction in the near wall u'/U_∞ level by approximately 6.8% compared to the Baseline case. At x = 705mm, the reduction in u'/U_∞ increases to 12.4%. As the freestream velocity increases (Figure 4.3b and 4.3c), the near wall turbulence reduction by the Riblet becomes more significant. The results provide a clear indication that the current Riblet surface can indeed manipulate the turbulence production in a boundary layer.

In the outer boundary layer region, the level of u'/U_∞ produced by the Riblet is also considerably less than that produced by the Baseline, especially at x = 625 and 645mm. This indicates that the turbulent energy transport across the entire boundary layer has been affected by the presence of the Riblet. At downstream locations of x = 665 and 705mm, whilst still exhibiting lower u'/U_∞ level at the near wall, the turbulence level in the outer boundary layer becomes similar, and sometimes exceed the Baseline counterpart. A similar result was noted by Yanjnik (63) and Choi (39) who described this increase as a natural redistribution of the turbulent kinetic energy in the outer boundary layer after a certain Riblet length has passed.

The observation thus far from the boundary layer mean and fluctuating profiles is that, whilst not showing much difference in the mean velocity profiles, the turbulent velocity profiles produced by the Riblet exhibit two characteristics. First, the near wall turbulence is very sensitive to the riblet where the reduction in the turbulence intensity level can be consistently achieved. In addition, the level of turbulence reduction increases as the Riblet length increases. Second, the sub-scale nature of the

Riblet is capable of extending its turbulence reduction influence to the outer layer, especially at the lower *x* region, i.e. the starting part of the Riblet plate. This indicates that when the turbulent boundary layer is relatively small in length scale under a certain Riblet height *h*, the disruption to the turbulence production at the near wall region can be effectively transferred to the outer layer. However, when the turbulent boundary layer grows further downstream, the effect of the riblet is mostly confined to the near wall region.

4.2.3. Skin Friction

Riblet is a passive flow control device that restrict the meandering of wall vortices. They are designed to be most effective in a specific range of flow conditions. The next analysis based on the data presented thus far will focus on the skin friction produced by both the Baseline and Riblet cases. For a turbulent boundary layer that originates from the surface of a smooth (Baseline) flat plate with zero pressure gradient, the skin friction coefficient can be obtained by referring to the boundary layer mean velocity profiles when they are plotted in non-dimensional parameters pertaining to the Law of the Wall. For instance, the Clauser method that uses u/U_∞ and $\rho U_\infty y/\mu$ as the non-dimensional parameters is a common method to determine the skin friction coefficient, where ρ and μ are the air density and dynamic viscosity, respectively. Since the linear relationship in the log layer of the boundary layer can be expressed as $u^+ = 5.6 \log_{10} y^+ + 4.9$, where $u^+ = \frac{u}{U_\infty}\sqrt{2/c_f}$ and $y^+ = \frac{\rho U_\infty y}{\mu}\sqrt{c_f/2}$, one can plot a series of lines with varying values of c_f, where c_f is the skin friction coefficient. The line that best fits the experimental data plotted in the same non-dimensional parameters represents the corresponding c_f produced by the wall surface. An example of this method is shown in Figure 4.4, in which the best fit of the experimental data is related to c_f = 0.00452. A comment about this method is that, obviously, the best fit is based on the log-layer region of a boundary layer, instead of the near wall sublayer region. Although there are debates surrounding this "extrapolation" method considering that the skin friction is closely related the velocity gradients at the near wall, i.e. $c_f \sim \tau_w \sim \mu \left(\frac{\partial u}{\partial y}\right)_{y\to 0}$, where τ_w is the wall shear stress. Nevertheless, using the Clauser method to determine the skin friction coefficients is still considered the best option in this study due to the extreme experimental difficulty to measure the $\left(\frac{\partial u}{\partial y}\right)_{y\to 0}$. Moreover, the error will be considered as relative because the emphasis is on the Δc_f between the Baseline and Riblet plates.

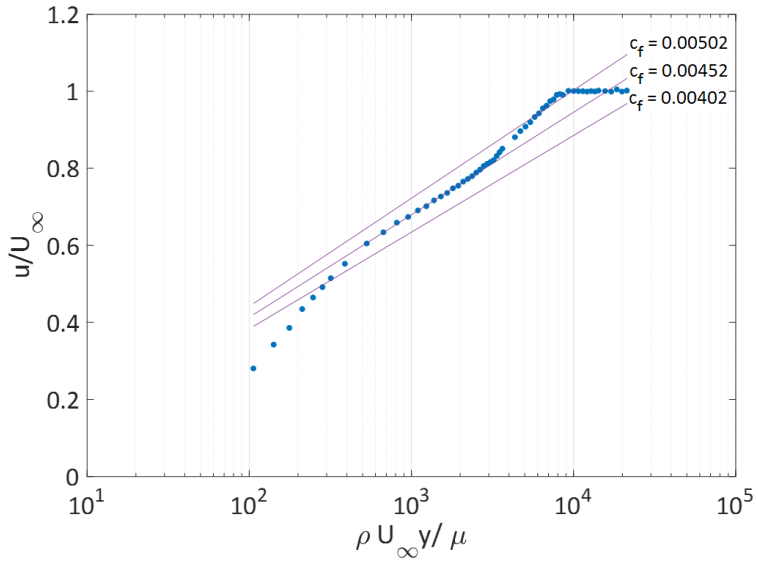

Figure 4.4 - Clauser plot for Baseline at 10m/s, 625mm downstream of the leading edge.

Further considerations are applied to the Riblet case. Clauser (93) proposes that for boundary layers at equilibrium, it can be expressed identically where $(u - U_\infty)/u_*$ is plotted against y/δ, where u_* is the fiction velocity. A similar method is suggested by Choi (39), where a velocity defect model was used in which the boundary layer velocity profile can be plotted in $(U_\infty - u)/u_*$ against $yu_*/\delta^* U_\infty$, where δ^* is the displacement thickness. With Choi's method it is assumed that the plots for the Riblets and Baseline would take the same shape except for the inner region of the boundary layer. Both Squire and Savill (94) and Bandyopadhyay (95) also used a similar technique, where accurate results can be obtained. Note that this method can also determine the virtual origin with a similar accuracy as the method proposed by Lee at al. (40). Using the velocity deficit model, the c_f can be varied in a similar fashion as the original Clauser model to obtain a good fit for the Riblets. An example of which is shown in Figure 4.5.

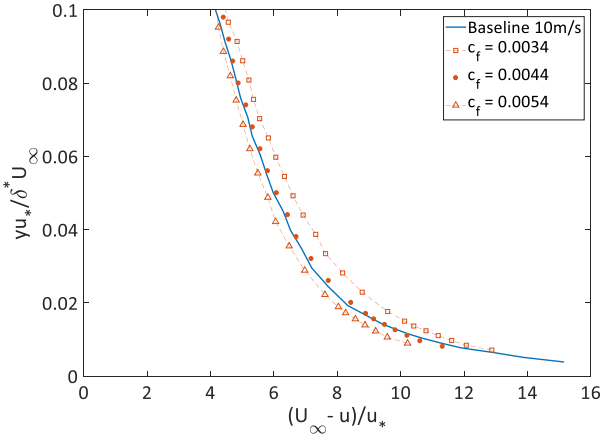

Figure 4.5 – Velocity defect matching for Riblet surface with respect to Baseline at 10m/s, 625mm downstream of leading edge.

After the determination of the skin friction coefficients, and thus the friction velocity u_τ, it is of interest to examine whether the Riblet might affect the flow in the context of deviation from the Law of the Wall, which uses the non-dimensional velocity and wall normal distance as the u^+ and y^+, respectively. Following the same Clauser's substitutions to the velocity and wall normal distance scaling, the boundary layer velocity profiles for the Baseline and Riblet cases are plotted in Figure 4.6. It is clear that whilst the gradient of the boundary layer profiles are the same for both, there is an increase of the intercept for the Riblet case from 4.9 to 5.4. Choi (39) attributes this "offset" by a Riblet to a reduction in the thickness of the viscous sublayer, leading to a reduction in the turbulent energy transport into the outer boundary layer. As shown in Table 4.1, the Riblet will produce smaller displacement thickness δ^*, momentum thickness θ and boundary layer thickness δ compared to the Baseline counterpart. Therefore, it is reasonable to assume that the laminar viscous sublayer for the Riblet case also follows this trend.

A general trend worth mention here is that, from Table 4.1, the boundary layer thicknesses in δ, δ^* and θ increase with x, they will decrease with U_∞. Table 4.1 also records the shape factors, H, which is defined as the ratio between the displacement thickness and momentum thickness. The typical shape factor of a turbulent boundary layer is H = 1.3~1.4 for a zero pressure gradient flow (96). From Table 4.1, the shape factor measured in the current study falls within an acceptable range pertaining to a fully developed turbulent boundary layer on a flat plate.

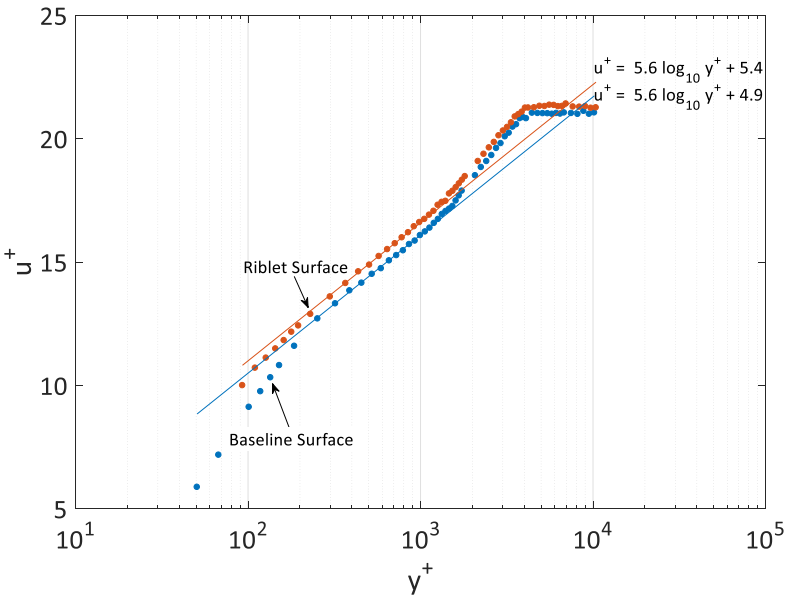

Figure 4.6 – Comparison of Law of the Wall for Baseline and Riblet surfaces at 10m/s, 625mm downstream of leading edge.

Summary of the skin friction coefficients for both the Baseline and Riblet are shown in Figure 4.7 and Table 4.1 for U_∞ = 10, 12 and 15m/s. The Riblet consistently demonstrates a production of lower skin friction coefficients than the Baseline counterpart across the entire ranges in x and U_∞ investigated in the current study[1]. The lower skin friction coefficient by the Riblet also correlates well with the earlier results in the turbulent velocity which shows a reduction in the turbulence intensity level at the near wall region. From the measured data, the average skin friction variations by the Riblet Δc_f (positive value denotes reduction, and vice versa) are in the region of 3.4% at U_∞ = 10m/s, 3.1% at U_∞ = 12m/s, and 2.5% at U_∞ = 15m/s. Hence, the effectiveness of the drag reduction capabilities of the Riblets, i.e. Δc_f, reduces with U_∞. As shown in Table 4.1, a higher U_∞ would entail lower boundary layer thicknesses in δ, δ^* and θ. In other words, Riblet with a fixed h at higher U_∞ will gradually be seen as a "surface roughness" instead of a sub-scale device that can restrict the wall vortices of the coherent structures. Despite only covering a relatively small U_∞ range, the interdependency between the boundary layer thickness and the Riblet height in their skin friction production follows a clear trend.

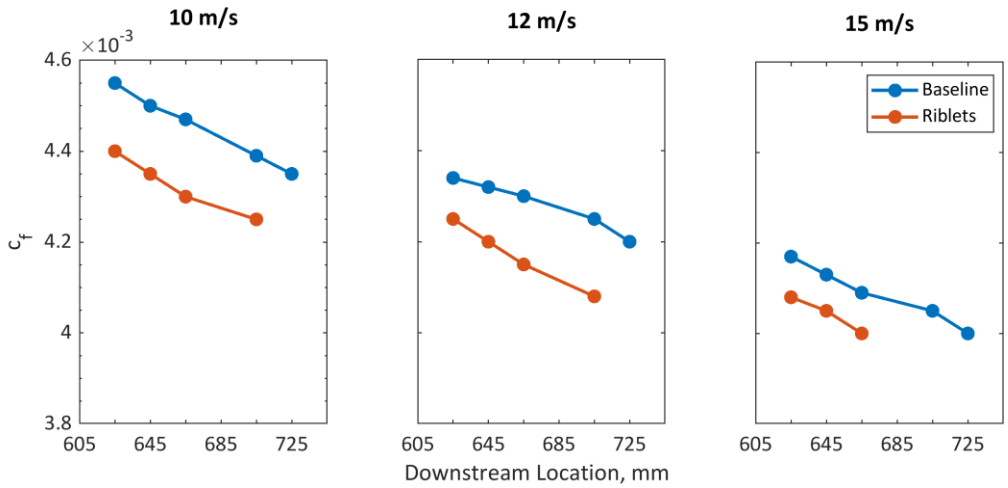

Figure 4.7 – Skin friction coefficient comparison between Baseline, Riblet and Empirical results.

[1] It should be noted that at x = 705mm and U_∞ = 15m/s, the result has been omitted because it was not possible to find a value inside the range of certainty. At x = 725mm, the result for the Riblet has also been omitted for the same reason.

Location, x	Boundary Layer Thickness, mm δ	Displacement Thickness, mm δ^*	Momentum Thickness, mm θ	Shape Factor, H	Skin Friction Coefficient, c_f	$\Delta\, c_f$, %
10m/s						
625 mm	11.352, 11.195	1.849, 1.565	1.362, 1.195	1.358, 1.310	0.00455, 0.00440	3.297
645 mm	12.097, 12.366	1.932, 1.744	1.412, 1.323	1.368, 1.319	0.00450, 0.00435	3.333
665 mm	12.633, 12.104	1.907, 1.818	1.391, 1.362	1.371, 1.335	0.00447, 0.00430	3.803
705 mm	13.125, 12.506	1.984, 1.806	1.424, 1.357	1.394, 1.331	0.00439, 0.00425	3.189
725 mm	14.393, 13.465	2.136, 2.425	1.534, 1.724	1.393, 1.407	0.00435, -	-
12m/s						
625 mm	10.857, 10.765	1.776, 1.568	1.314, 1.214	1.351, 1.214	0.00434, 0.00425	2.074
645 mm	11.794, 11.090	1.839, 1.607	1.353, 1.217	1.359, 1.320	0.00432, 0.00420	2.778
665 mm	11.950, 11.835	1.855, 1.792	1.366, 1.353	1.357, 1.325	0.00430, 0.00415	3.488
705 mm	12.205, 11.950	1.941, 1.769	1.415, 1.335	1.371, 1.325	0.00425, 0.00408	4.000
725 mm	12.588, 13.296	2.085, 2.285	1.493, 1.620	1.397, 1.411	0.00420, -	-
15m/s						
625 mm	10.503, 10.289	1.688, 1.403	1.260, 1.079	1.340, 1.300	0.00417, 0.00408	2.158
645 mm	10.985, 10.702	1.730, 1.498	1.278, 1.129	1.353, 1.328	0.00413, 0.00405	1.937
665 mm	10.846, 10.870	1.745, 1.623	1.299, 1.221	1.343, 1.329	0.00409, 0.00400	2.200
705 mm	11.340, 10.950	1.767, 1.675	1.313, 1.264	1.346, 1.325	0.00405, -	-
725 mm	12.159, 12.472	1.885, 2.174	1.349, 1.540	1.397, 1.411	0.00400, -	-

Table 4.1 – Summary of the turbulent boundary layer integral parameters at 10m/s, 12m/s and 15m/s respectively. Baseline to left of comma, Riblet to right of comma (taken about the virtual origin).

4.3. "Stationary" Turbulent Boundary Layer – analysis based on the wall pressure fluctuations

The previous section focuses on the time-domain analysis of the turbulent boundary layer subjected to the Baseline and Riblet surfaces. Based on the analysis of the mean velocity profiles, the drag reducing capabilities of the Riblet device designed and manufactured in-house have been positively demonstrated. In general, the amount of records in the literatures that document the wall pressure fluctuations when subjected to Riblet treatment on the wall surface are still scarce. The manipulation of the turbulence structures by the Riblet is also less studied from the perspective of the wall pressure fluctuations, which would otherwise be an important quantity for the aeroacoustics field. This section aims to fill this gap by presenting results obtained from the frequency-domain analysis of the wall pressure fluctuations, e.g. the Power Spectral Density (PSD), coherences, and turbulence length scale as a function of frequency, as well as time-domain analysis of the wall pressure fluctuations, e.g. the cross-correlation coefficients.

4.3.1. Power Spectral Density

The primary instrument to measure the wall pressure fluctuations is the remote microphone sensors. Descriptions of which, including the streamwise and spanwise distributions of these sensors across the flat plate surface are documented in Chapter 3. These remote microphone sensors are phase-calibrated against a reference microphone from a specially designed and manufactured calibrator to facilitate cross-correlation and coherence in the data analysis. Note that the amplitude of the fluctuations is not calibrated for the remote microphone sensors. Nevertheless, once installed, these remote microphone sensors will remain undisturbed even during the interchange between the Baseline and Riblet surfaces. Therefore, direct comparison for the wall pressure PSD between the Baseline and Riblet cases is valid.

Figure 4.8 presents the wall pressure PSD at x = 625, 645 and 665mm for U_∞ = 10, 12 and 15m/s. In each sub-figure, an offset of 5 dB is applied to each consecutive wall pressure spectrum of increasing x to make the comparison easier. Also, in each sub-figure two indicative lines pertaining to the frequency decay of $f^{-5/3}$ and f^{-5} are included. The PSD is showing the relative energies of the turbulent eddies in the boundary layer. The PSD at lower frequency dominates the flow, which is indicative of larger size eddies. The high frequency range is indicative of the smaller size eddies in the flow. To help with the discussion later, a generalisation is made here whereby the frequency region that contains a wall pressure PSD level decaying at $f^{-5/3}$ will be referred to as the "mid frequency", where the frequency range below it will be called the "low frequency". Finally, the frequency range that contains a wall pressure PSD level decaying at f^{-5} will be referred to as the "high frequency".

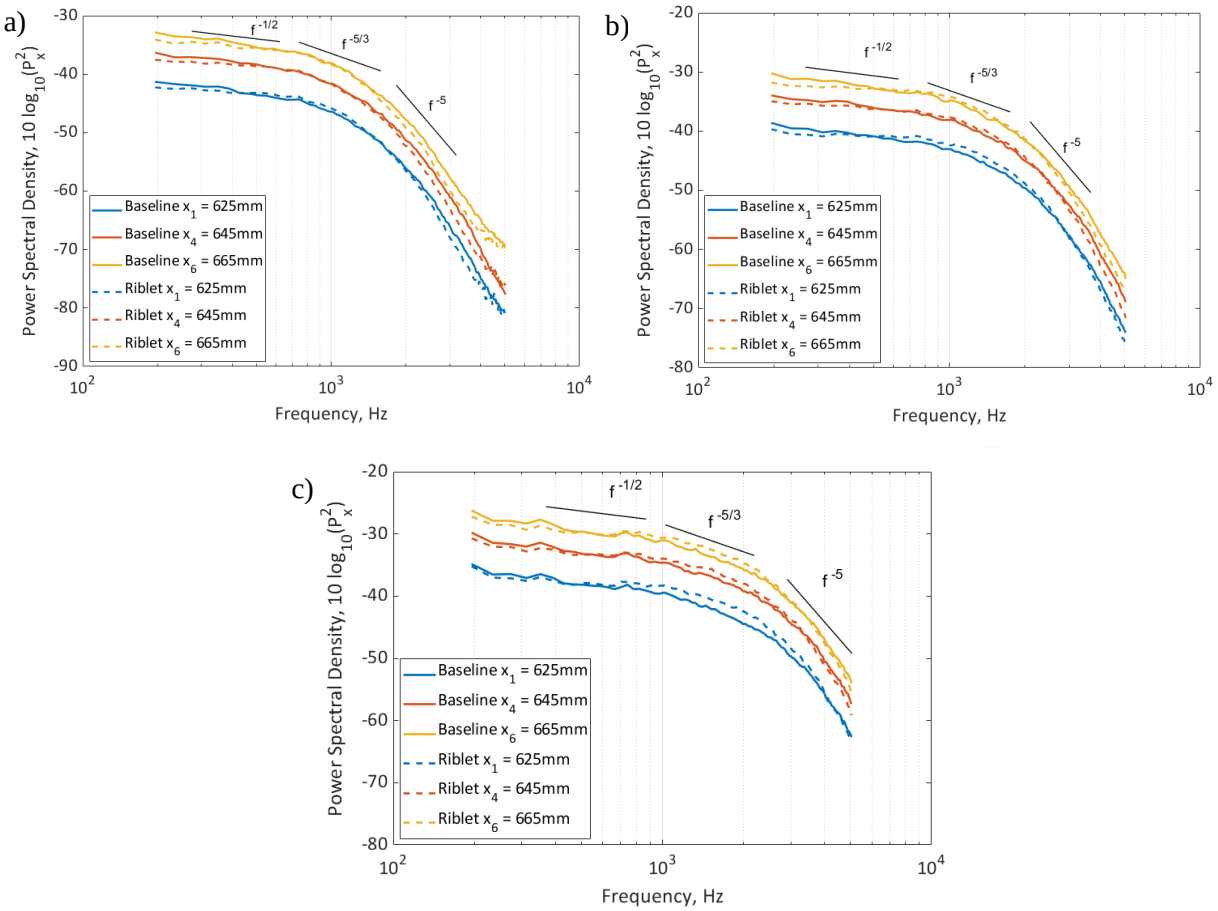

Figure 4.8 – Comparison of Baseline and Riblet surface pressure PSD for 3 downstream locations at a) 10m/s, b) 12m/s and c) 15m/s.

In Figure 4.8a, as mentioned earlier the wall pressure spectra are dominant at low frequency whose decay rate is relatively small. At some mid frequency region, the PSD will begin to decay at a rate of $f^{-5/3}$ (~ Kolmogorov's energy dissipation rate). However, at higher frequencies the decay rate of the wall pressure spectra increases to f^{-5}. This result is also observed by Gravante *et al.* (97) for a 2D turbulent boundary layer, similar to the current flow condition. As the flow progresses downstream and the boundary layer thickness grows, the location of the mid frequency range moves towards the lower frequency range. This may indicate that the boundary layer now is more dominated by the larger turbulent eddies, and less by the small-scale turbulent eddies. A similar trend is also observed at the wall pressure PSD at Figure 4.8b and 4.8c for higher freestream velocity.

At first glance, the wall pressure PSD produced by both the Baseline and Riblet are quite similar. However, a closer examination does reveal some notable differences for some cases. In the low and high frequency ranges, the Riblet produces lower level of wall pressure PSD compared to the Baseline counterpart. When examining the decay rates of the wall pressure PSD level, the Riblets have a lower energy signature in the low frequency region where the large scale turbulent eddies are slower to

dissipate (characterised by a slightly lower decay gradient of $f^{-1/2}$ whereas the energy at high frequency dissipates slightly faster over the Riblets than on the Baseline plate. This raises a prospect that, for the case of acoustic scattering at the trailing edge whose wall pressure PSD and scattered acoustic PSD are highly correlated, a lower level of wall pressure PSD observed in the Riblet surface has a potential to cause a lower noise emission at the low and high frequency regions. The results also suggest that the Riblet can manipulate more effectively for the large and small-scale turbulent eddies. However, it should also be noted that the wall pressure PSD is not the only hydrodynamic source for the far field radiation. For example, the lateral turbulence length is another important hydrodynamic source for trailing edge noise. More discussion about this can be found in Section 4.3.4.

To explain the above results from a physical point of view, the low speed streaks in the near wall region of the turbulent boundary layer over a Riblet surface are forced into alignment and their meandering tendencies are reduced significantly. Due to the presence of the virtual origin, they do not come into direct contact with the surface of the Riblets and they could also be effectively displaced from the surface in such a way that the turbulent structures would reside above the Riblet tip, and force a separation distance from the surface. It could be argued that since the boundary layer subjected to Riblet surface is described by a virtual origin, the wall pressure PSD would register a reduction since the turbulent structures is not in direct contact with the surface anymore. Nevertheless, it appears that this physical explanation is only applicable to the large and small-scale turbulent eddies. In the mid frequencies, where the wall pressure PSD would decay at $f^{-5/3}$, in some cases the Riblets actually produce a slight increase in the wall pressure PSD level when compared to the Baseline.

The above phenomena produced by a Riblet may be explained by Choi (39), who observes that the momentum exchange between the inner and outer layers is adjusting in response to the reduced viscous layer thickness by the Riblet. In the mid frequencies, the wall pressure PSD level produced by the Riblet is higher, which indicates that the relevant turbulent scale in this mid frequency range contains more energy as the result of the momentum exchange between the inner and outer layers. As the freestream velocity increases, the increase of the wall pressure PSD level at the mid frequency becomes more pronounced. This is likely to be caused by the thinner turbulent boundary layer beginning to experience the Riblet as a surface roughness, a phenomenon that is also more pronounced at the more upstream x locations.

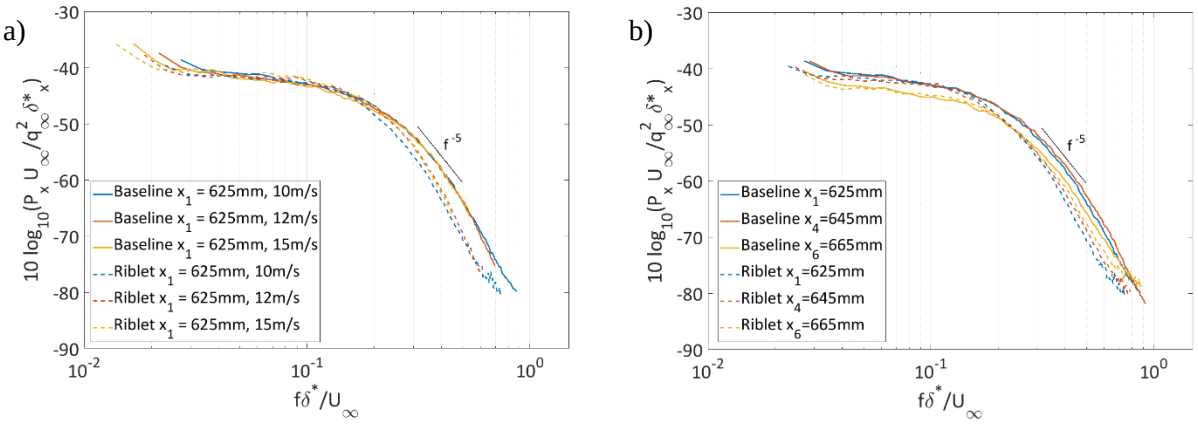

Figure 4.9 – Normalised wall pressure PSD for both the Baseline and Riblet at x = 625mm for U_∞ = 10, 12 and 15m/s.

From the discussion above, the disparity of the wall pressure PSD between the Baseline and Riblet as a result of flow interchange between the inner and outer layers may be examined alongside the variations in their boundary layer integral thicknesses. The next step is to study the universality of the Baseline and Riblet in their production of the wall pressure PSD. The scaling parameters are chosen as the outer variables, whereby the spectra is normalised using q_∞ (= ½ρU_∞^2) as the pressure scale and δ^*/U_∞ as the time scale. Accordingly, the frequency is non-dimensionalised by the inverse of the time scale used above. Figure 4.9a represents the non-dimensionalised wall pressure PSD at x = 625mm for U_∞ = 10, 12 ad 15m/s. For the Baseline cases, the spectra collapse well for most of the scaled-frequency range, including those at the high frequency despite using the outer-layer scales. The decay rate at the high frequency again follows $(f\delta^*/U_\infty)^{-5}$. The Riblet cases themselves also features a good collapse of the spectra throughout the non-dimensional frequency range, and the decay rate at the high frequency still follows $(f\delta^*/U_\infty)^{-5}$ reasonably well. However, it illustrates that the small-scale turbulent eddies can be attenuated more effectvely by the Riblets when compared to the Baseline.

When the comparison of the wall pressure PSD between the Baseline and Riblet is made in dimensional spectral level and frequency, the implication could be quite different when the same comparison is made in non-dimensional spectral level and frequency. For example, one could compare the dimensional (Figure 4.8c) and non-dimensional (Figure 4.9a) spectra for the case of x = 625mm and U_∞ = 15m/s: when compared to the spectrum produced by the Baseline in dimensional form, the Riblet demonstrates a slightly lower spectral level at the low frequency (f < 650Hz), higher spectra level at the mid frequency (650 < f < 4000Hz), and then a slightly lower spectral level at the high frequency (f > 4000Hz). However, when plotted in non-dimensional form, the scaled spectra between the Riblet and Baseline seem to "nudge" towards each other in the frequency-domain in such a way that they collapse well at $f\delta^*/U_\infty$ < 0.2, but a much larger level of reduction for the scaled

spectral level is demonstrated by the Riblet at $f\delta^*/U_\infty > 0.2$. This lends support to our earlier description that a Riblet can affect both the inner and outer parts of a boundary layer by disrupting the momentum exchange between them. More examination of this mechanism will be discussed in Sections 4.4 and 4.5 when the investigation turns to the temporal development of turbulent spots on the Riblet surface.

Figure 4.9b examines the scalability of the spectral level and frequency as a function of streamwise distance (x = 625, 645 and 665mm) under a single velocity of U_∞ = 10m/s. This is basically a re-plot of Figure 4.8a in a non-dimensional form, and without the application of the offset to the scaled spectral level. In Figure 4.9b, the collapse of the scaled spectra at $f\delta^*/U_\infty < 0.2$ can be repeated. However, at $f\delta^*/U_\infty > 0.2$, the Riblet that was originally shown to be effective in producing a lower scaled spectral level at x = 625mm becomes less effective at downstream location of x = 665mm. This illustrates that as the boundary layer over the Riblet surface becomes thicker, the ability of the Riblet to manipulate the turbulent structures becomes weaker, which is reflected by the wall pressure PSD slowly conforming to that of the Baseline's.

4.3.2. Streamwise Cross-correlation

The streamwise cross-correlation coefficient R_{xixj}, as defined in Equation 4.4, can be the measure of the turbulence decay in the temporal domain between the wall pressure fluctuation signals from two remote microphone sensors. In the equation, P'_{x_i} and P'_{x_j} are the wall pressure fluctuations from the remote microphone sensors i and j situated at locations x_i and x_j, respectively. Likewise, $P'_{x_i\,RMS}$ and $P'_{x_j\,RMS}$ are the root mean square values of the pressure fluctuations measured by the remote microphone sensors i and j respectively. τ is a time delay in ms between the signals, and the overbar denotes time averaging. This type of time domain analysis can be used to determine the convection velocity of the most prevalent scale of turbulence structures. For two remote microphone sensors that are separated by ε in the streamwise direction, the convection time for the most dominant wall pressure generating structures to traverse between them can be identified by the time delay τ corresponding to the maximum cross-correlation coefficient. From a dataset of (ε, τ), an average convection velocity of the dominant turbulent eddies can be determined. It should be noted that the most dominant turbulent eddies in the boundary layer would decay at a slower rate than the small-scale turbulent eddies.

$$R_{x_i x_j} = \frac{\overline{P'_{x_i}(x_i, t) P'_{x_j}(x_j, t-\tau)}}{P'_{x_i\,RMS}(x_i) P'_{x_j\,RMS}(x_j)}$$

Equation 4.4

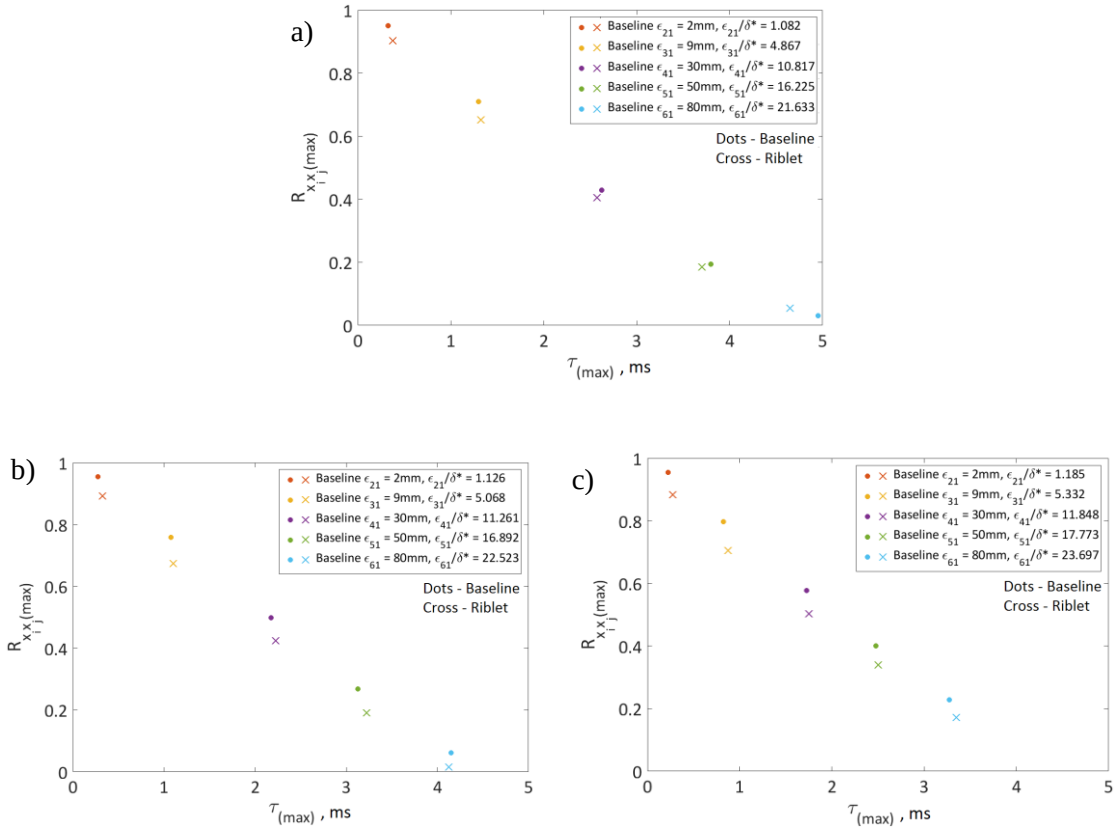

Figure 4.10 – Comparison of Baseline and Riblet streamwise cross-correlation maxima at a)10m/s, b) 12m/s and c) 15m/s

In the present experiments, all the streamwise cross-correlation studies were conducted by taking reference to the most upstream remote microphone sensor at x = 625mm. ε_{k1} denotes the distance between the reference microphone (subscript 1) and another microphone under question (subscript k). Figure 4.10 plots the maximum normalised cross-correlation coefficients, $R_{xixj\,(max)}$, against their corresponding $\tau_{(max)}$ for ε_{21}, ε_{31}, ε_{41}, ε_{51} and ε_{61}. The auto-correlation peak for the ε_{11} is omitted as by default it has a maximum value of $R_{xixi\,(max)}$ = 1 at $\tau_{(max)}$ = 0. The ε_{k1} are also normalised by the displacement thickness of the boundary layer at the reference microphone location (i.e. x = 625mm), where the values are tabulated in the figure.

It is clear from the figure that the Riblet consistently produces lower level of the $R_{xixj\,(max)}$ when compared to those produced by the Baseline. The difference between them is in the region of 3.2–8.3%. A reduced level of $R_{xixj\,(max)}$ achieved by the Riblet may be interpreted as a more effective

breakdown of the turbulence structures. This outcome is quite consistent across the freestream velocity at U_∞ = 10, 12 and 15m/s. There is also a clear evidence that the decay in $R_{xixj\,(\max)}$ is relatively linear across the range of time delay $\tau_{(\max)}$ for both the Baseline and Riblet. Nevertheless, if the linear best fit to these data points are extrapolated backward, the line will not intercept at $R_{xixi\,(\max)}$ = 1 at $\tau_{(\max)}$ = 0. This means that between ε_{11} and ε_{21}, which is 2mm apart, the linearity does not apply. This is likely to be due to the overlapping signals of turbulence structure whose characteristic length scale in the longitudinal direction is larger than 2mm.

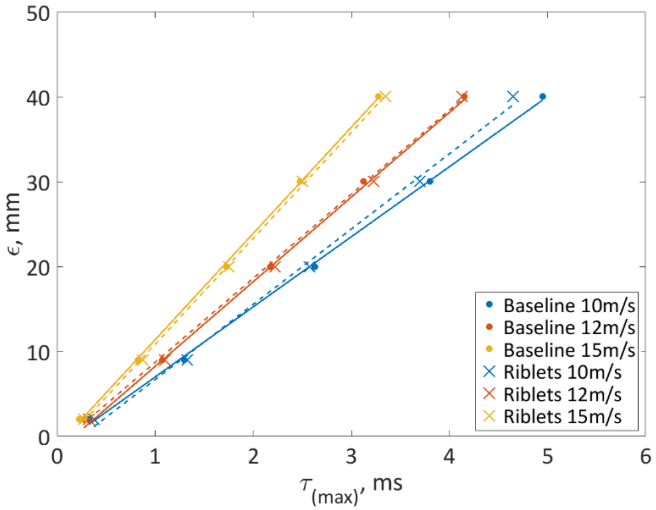

Figure 4.11 – Convection velocity of flow Riblets compared to Baseline

The next step is to investigate whether achieving a more rapid breakdown of the turbulence structures by the Riblet can also affect the turbulence convection velocity. Figure 4.11 presents several linear best fit lines for the datasets of ε against $\tau_{(\max)}$. The gradients of the linear best fit lines represent the convection velocity of the most dominant turbulence structures, which will increase proportionally with the U_∞. However, the comparison suggests that there is not a huge difference in the convection velocities of the dominant turbulence structures between the Baseline and Riblet. This is reflected in Table 4.2, which summarises the turbulence convection velocities normalised by the U_∞. The normalised convection velocity of about 0.8 is typical for a turbulent boundary layer.

	Baseline		Riblet	
U_∞	u_c (m/s)	u_c/U_∞	u_c (m/s)	u_c/U_∞
10m/s	8.216	0.822	8.875	0.875
12m/s	9.506	0.792	9.976	0.831
15m/s	12.522	0.835	12.480	0.832

Table 4.2 – Summary of the convection velocity of the dominant turbulence structures between the Baseline and Riblet cases.

4.3.3. Streamwise Coherence

Brooks and Hodgson (98) expressed that by measuring the streamwise coherence, it is possible to understand the lifespan of turbulent eddies in the flow filed. It is a measure of the *likeness* in the frequency domain of the pressure fluctuation signals between two remote microphone sensors. By definition, the magnitude squared coherence of two remote microphone signals, γ^2 is

$$\gamma^2(f) = \frac{|P_{x_i x_j}(f)|^2}{P_{x_i x_i}(f) P_{x_j x_j}(f)}$$

Equation 4.5

where $0 \leq \gamma^2 \leq 1$. P_{xixj} (f) is the cross power spectral density between two wall pressure fluctuating signals at locations x_i and x_j. The wall pressure signal at x_i is usually designated as the *reference* microphone sensor located at x = 625mm at the mid-span of the flat plate. Therefore, P_{xixi} (f) is the auto power spectral density of the reference wall pressure fluctuation. The wall pressure signals at location x_j represents another microphone sensor. Likewise, P_{xjxj} (f) is the auto power spectral density of the corresponding wall pressure fluctuation. If x_j is located at a certain longitudinal distance downstream of the reference microphone, but without any spanwise offset, the corresponding γ^2 represents the streamwise coherence. Alternatively, if x_j is located at a certain distance along the spanwise distance against the reference microphone, but without any streamwise offset, the corresponding γ^2 represents the spanwise coherence. In this sub-section, the analysis will be based on the streamwise coherence. The spanwise coherence will be discussed in Section 4.3.4.

Figure 4.12 compares the streamwise coherence spectra between the Baseline and Riblet cases at U_∞ = 10, 12 and 15m/s. Like the notation used in the cross-correlation analysis in Section 4.3.2, the streamwise coherence is described by ε_{k1}, which denotes the longitudinal distance between the reference microphone (subscript 1) and another microphone under question (subscript k). The spacing is expressed in dimensional term as well as non-dimensional term where the boundary layer displacement thickness at microphone 1 is used as the scaling parameter. These values can be found in the figure.

First, the analysis will focus on the coherence spectra for the Baseline case only. For the microphone pair of ε_{21} (Δx = 2mm, $\Delta x/\delta^*$ = 1.1–1.2), γ^2 = 1 cannot be found anywhere in the frequency. This illustrates that, even at such a short distance apart, a decay of coherence has already happened in the convecting field. The most dominant γ^2 (~ 0.8–0.9) understandably occurs at low frequency, which is associated with the large scale turbulent eddies. The streamwise coherence will undergo a logarithm

decay as a function of the frequency. This reflects a more effective turbulence dissipation at a smaller length scale. The trend holds true for all the U_∞ cases investigated in this study. It will become apparent that the decay of coherence level is non-linear with the separation distance ε_{k1}. For the next microphone pair of ε_{31} (Δx = 9mm, $\Delta x/\delta^*$ = 4.9–5.3), the coherence levels undergo a massive drop to $\gamma^2 \approx 0.2$. The results indicate that majority of the turbulence decay takes place within a scaled-longitudinal distance of $\approx 5\delta^*$. If the separation distance increases two folds to ε_{41} ($\approx 11.5\delta^*$) and three folds to ε_{51} ($\approx 17\delta^*$), only a slight drop of the coherence level is registered. When the scaled-longitudinal increment becomes slightly more than four folds at ε_{51} ($\approx 23\delta^*$), the coherence level diminishes across most of the frequency.

Some interesting phenomena may be discernible in the coherence spectra. Between ε_{31} and ε_{51}, there are narrowband frequency where elevated coherence level can be identified. Note that the word "elevated" is in the context of relative, since the overall coherence level is already quite low. For description purpose, this narrowband region is called the $\gamma^2_{(\text{hump})}$. By definition, the $\gamma^2_{(\text{hump})}$ can be related to a finite turbulence length scales that are slightly more resistant to the viscous dissipation. If $\gamma^2_{(\text{hump})}$ is related to a particular turbulence/vortical structure, the frequency pertaining to $\gamma^2_{(\text{hump})}$ decreases as the ε_{k1} increases for all the U_∞ cases investigated here. This implies that the associated length scale increases in the convecting field. In addition, this convective turbulence/vortical structure becomes increasingly coherent as U_∞ increases. It is out of scope for the current thesis to investigate the origin of this turbulence/vortical structure, if any. Nevertheless, even if such structure exists, the dominant source of the wall pressure fluctuation measured in this study is still expected to originate from the two-dimensional turbulent boundary layer. This can be reflected in Figure 4.8 for the wall pressure PSD where no narrowband spectra hump can be found for all the cases.

Now, the analysis will focus on the comparison of γ^2 between the Baseline and Riblet. The figure clearly shows that, at a short longitudinal separation distance of ε_{21}, the Riblet can already achieve a significant reduction of the coherence level for the wall pressure fluctuations across almost the entire range of frequency. This indicates that a significant cascade of turbulence length scales has been manipulated even at the early stage of the Riblet. The level of difference in the γ^2 between the Baseline and Riblet, as a function of frequency, increases as the U_∞ increases. This could be due to the fact that a Riblet is more effective when the ratio between the Riblet height and boundary layer thickness increases. However, it should also be noted that such ratio should not be too large as the Riblet could switch its role from a drag-reducing device to a turbulence-enhancing surface roughness. For the rest of the longitudinal separation distances, between ε_{31} and ε_{61}, reduction of γ^2 against the Baseline is also observed. This is considered as a natural continuation of the turbulence decay achieved by the Riblet earlier on.

As a closing remark of this sub-section, the wall turbulence can react rapidly to a Riblet in the context of coherence function decline. Although a Riblet can manipulate a wall turbulence structure in the longitudinal direction, as well as reduce the r.m.s. longitudinal velocity fluctuations in the boundary layer significantly (Figure 4.3), it does not result in a significant reduction of the wall pressure PSD level (Figure 4.8)[2]. It is known that the wall pressure fluctuations are pre-dominantly contributed by the velocity fluctuations in the transverse direction, e.g. the wall-inward sweeping event during the re-generation cycle of the coherent structures. Although a Riblet can change the turbulence structure in the convective field (i.e. its longitudinal structure), and reduce the overall boundary layer thicknesses (Table 4.1), it may not change the fundamental turbulence re-generation mechanism significantly.

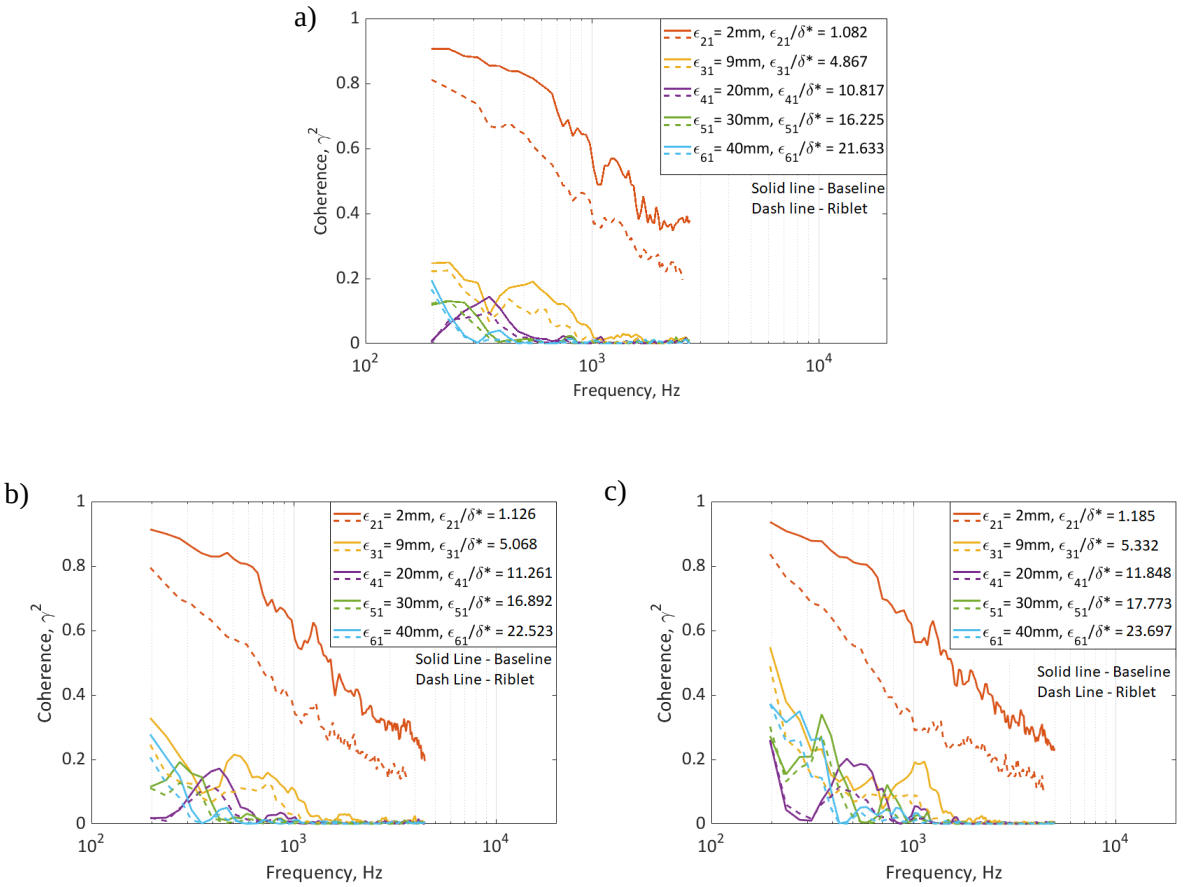

Figure 4.12 – Comparison of Baseline and Riblet streamwise coherence at U_∞ = a) 10m/s, b) 12m/s and c) 15m/s

[2] However, when both the spectral level and frequency of the wall pressure PSD are presented in non-dimensional form (Figure 4.9), considerable level of reduction can be observed at the high frequency range.

4.3.4. Spanwise Coherence

Another parameter that is appropriate to describe a turbulence structure and its physical size in the frequency domain is the spanwise (lateral) coherence function. As will be discussed later, the spanwise coherence function is also related to the spanwise length scale of the turbulence, which is one of the key sources for the trailing edge noise radiation. This sub-section will investigate the response of spanwise coherence of the turbulence when the wall surface is of the Riblet type. The spanwise coherence can also be described by Equation 4.5 for the magnitude squared coherence, γ^2, of two remote microphone signals that are located at the same longitudinal position, but separated in the lateral direction. Similarly, the *reference* wall pressure signal at x_i in Equation 4.5 is the microphone sensor located at x = 625mm at the mid-span of the flat plate. Wall pressure signal measured at microphone x_j only varies along the lateral direction.

Figure 4.13 shows the spanwise coherence spectra between the Baseline and Riblet cases at U_∞ = 10, 12 and 15m/s. The spanwise coherence is also described by ε_{k1}, which now denotes the lateral distance between the reference microphone (subscript 1) and another microphone under question (subscript k). It is important to reiterate here that the locations of the microphone k for the Riblet are differed slightly against the microphone k for the Baseline counterpart due to the physical constraint imposed by the Riblet geometrical spacing. Nevertheless, such a small difference can be treated as negligible. The spacing is expressed in dimensional term as well as non-dimensional term where the boundary layer displacement thickness at microphone 1 is used as the scaling parameter. This is reflected in the legends of Figure 4.13.

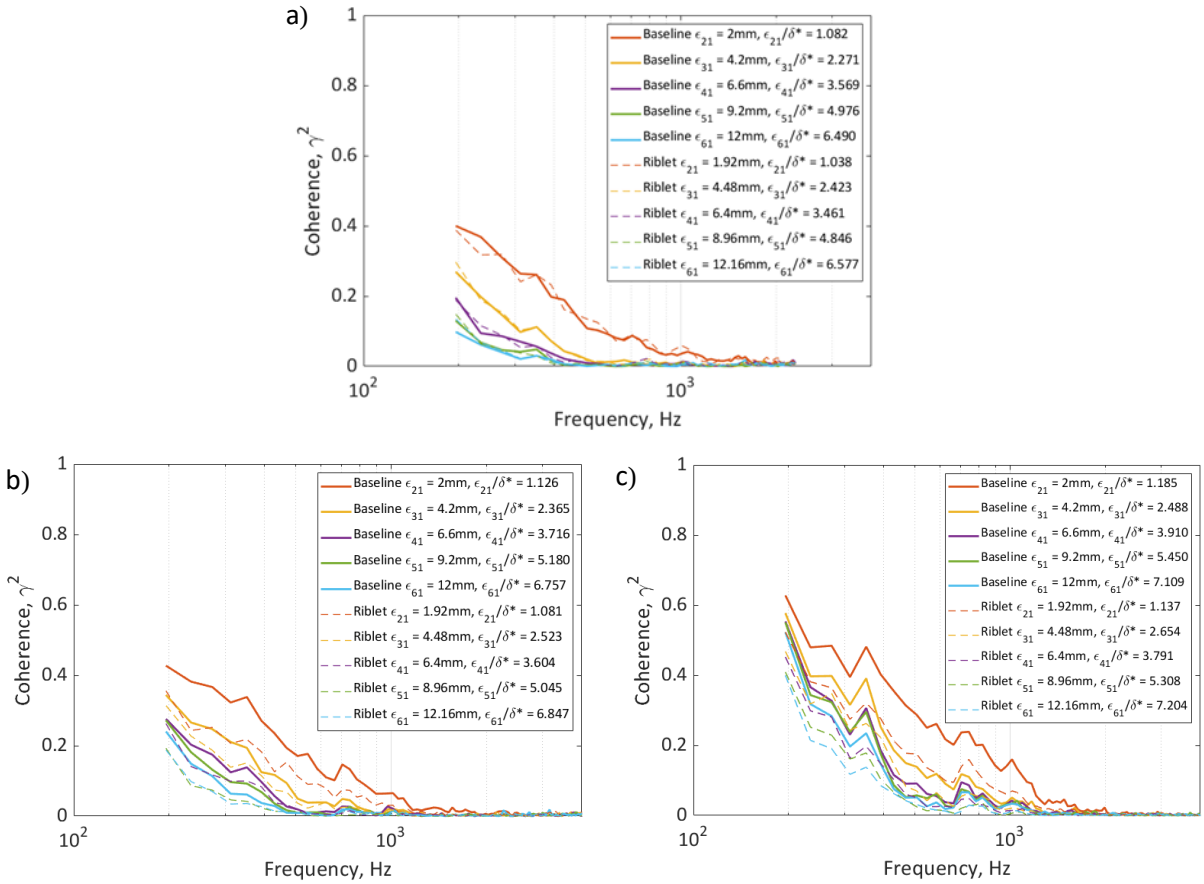

Figure 4.13 – Spanwise Coherence for Baseline and Riblet at x = 625mm at U_∞ = a) 10m/s, b) 12m/s and c) 15m/s

As expected, the spanwise coherence spectra exhibit an exponential decay across the frequency for all the cases examined. The overall coherence level also reduces as the lateral separation distance ε_{k1} increases, which denotes the increasingly loss in likeness of the turbulence. At U_∞ = 10m/s, the spanwise coherences produced by the Riblet between ε_{21} and ε_{61} are almost identical to those of the Baseline, suggesting that the turbulence structures maintain the same degree of lateral order over the Riblet. This means that the fundamental turbulence re-generation mechanism remains unaffected, which is supported by the fact that, except at the low frequency, the Riblet is incapable of altering the wall fluctuating pressure PSD at the mid and high frequencies as shown in Figure 4.8a. This also provides a further proof that the wall fluctuating pressure PSD is more correlated to the spanwise coherence instead of the streamwise coherence despite the latter is more sensitive to the Riblet (Figure 4.12a).

However, at U_∞ = 12 and 15m/s, the level of spanwise coherence achieved by the Riblet becomes consistently lower than the Baseline counterparts, especially for the ε_{21} where large reduction has been achieved. This implies that the fundamental turbulence structure may already be altered by the Riblet, which is also manifested by the quantifiable changes in the wall fluctuating pressure PSD at

the mid frequency shown in Figure 4.8b and 4.8c. Hence, it seems that the wall pressure spanwise coherence and PSD become more sensitive to the Riblet when U_∞ > 10m/s. A plausible explanation is related to the reduction of boundary layer thickness as U_∞ increases. After examination of the tabulated values in Table 4.1 in conjunction with the current Riblet whose height is fixed at h = 0.36mm, a condition of h/δ^* > 0.2 must be fulfilled in order for the Riblet to affect the wall pressure spanwise coherence and PSD. Note that this condition is for the wall pressure fluctuation only and does not apply to the velocity fluctuation levels within the turbulent boundary layer as shown in Figure 4.3.

$$l_z(f) = \int_0^\infty \sqrt{\gamma^2(z,f)}\, dz$$

Equation 4.6

The spanwise coherence does not measure any convective components of the turbulence structures. Instead, it mostly contains information about the physical size of the turbulent eddies. By definition, an integration of the spanwise coherence magnitude across the lateral location can result in the lateral coherence length of the turbulence, l_z, as a function of the frequency. This is illustrated in Equation 4., where γ^2 is the magnitude square of the spanwise coherence, and z is the distance in the lateral direction. In the current work, a total of seven microphones with various degrees of spanwise offset against the reference microphone are used for the calculation of the l_z. Note that the possible quantification error for the l_z is negligible because the focus in the current study is to compare the turbulence length scales produced by the Baseline and Riblet, respectively. Therefore, the context is relative, not absolute.

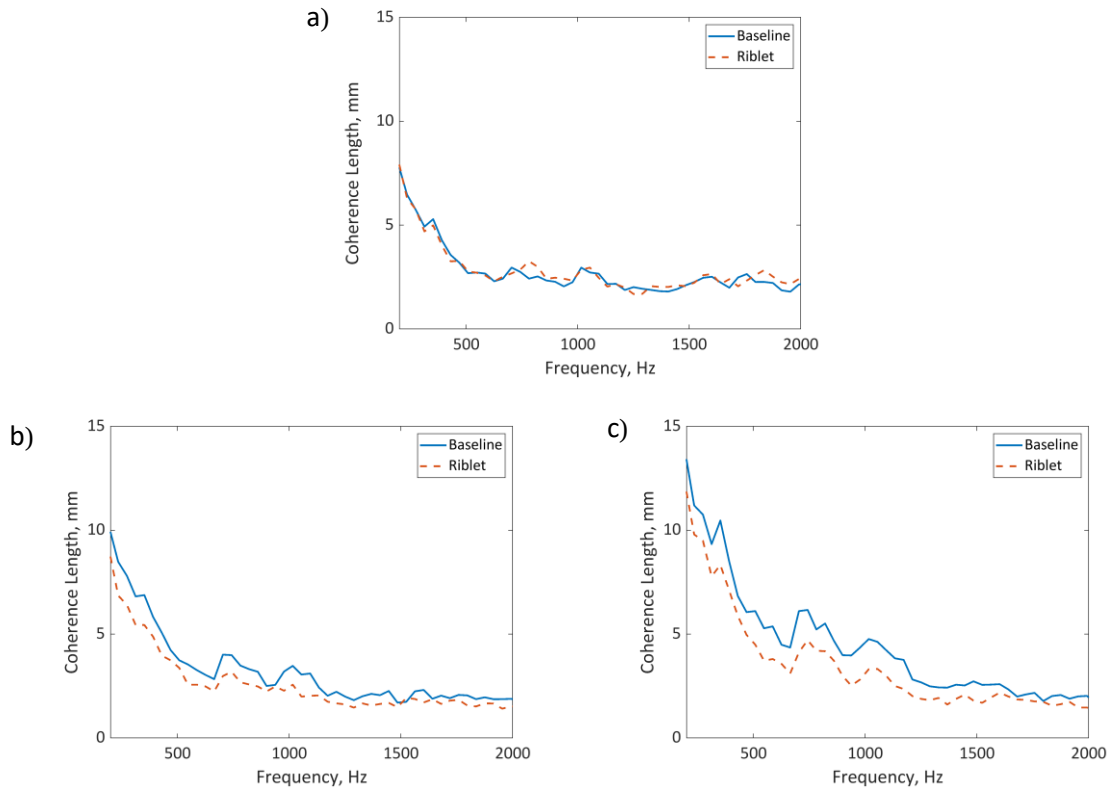

Figure 4.14 – Lateral Coherence Length of the turbulence at x = 625mm at U_∞ = a) 10 m/s, b) 12m/s and c) 15m/s

As shown in Figure 4.14a, the l_z spectra for both the Baseline and Riblet at U_∞ = 10m/s are very similar, which is consistent with the spanwise coherence spectra in Figure 4.13a. As expected, when the U_∞ increases to 12 and 15m/s in Figure 4.14b and 4.14c, respectively, both demonstrate a lower l_z, hence the size of the turbulence structure, when the Riblet is introduced.

The relationship between the far field pressure (i.e. noise) and the near field wall pressure fluctuation near the trailing edge of an aerofoil is made explicit in the classical work of Amiet (99) (100), who derived a direct relationship between the PSD of the far field trailing edge noise (S_{pp}) of an aerofoil for an observer in the centre-line plane of an aerofoil with span 2d, chord, 2b, to the wall pressure PSD (S_{qq}) by:

$$S_{pp}(x,0,y,\omega) = \left(\frac{\omega b y}{2\pi c_o \sigma^2}\right)^2 d|\mathcal{L}|^2 l_z(\omega) S_{qq}(0,\omega)$$

Equation 4.7

where ω is the angular frequency, σ^2 is a Mach number corrected geometrical function and $|\mathcal{L}|$ is the norm of the acoustical transfer function. From Equation 4.7, the product of the lateral coherence

length (l_z) and wall pressure PSD (S_{qq}) represents the main combined sources of the radiated spectrum (S_{pp}). Although no aeroacoustics measurement on aerofoil is performed in this study, it is still possible to evaluate the effect of Riblet on the trailing edge noise radiation by examining the 10 $\log_{10}(l_z . S_{qq})$.

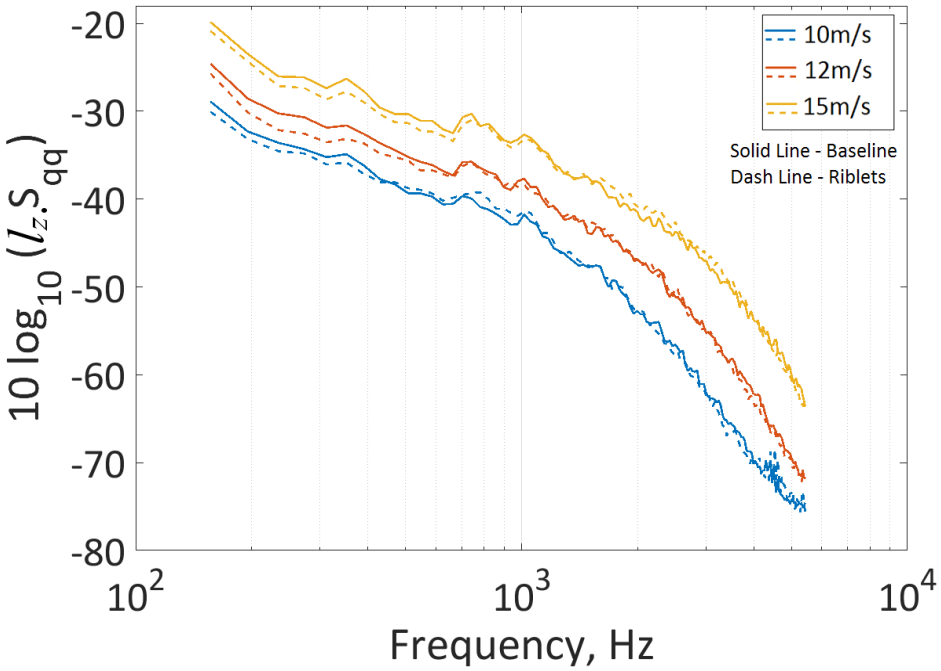

Figure 4.15 – Partial hydrodynamic sources based on Amiet's model for the prediction of the trailing edge noise radiation at x = 625mm

Figure 4.15 presents the 10 $\log_{10}(l_z . S_{qq})$ at x = 625mm between the Baseline and Riblet at U_∞ = 10, 12 and 15m/s. For the three U_∞ cases, slight reduction of 10 $\log_{10}(l_z . S_{qq})$ by the Riblet occurs at the low frequency ($150 < f < 600$Hz) only. This outcome is expected because both the hydrodynamic sources S_{qq} and l_z are predominantly lower respectively. The result suggests that a slight reduction of the trailing edge noise at low frequency might be possible for a Riblet. For the mid and high frequencies ($f > 600$Hz), however, the Riblet would produce a similar 10 $\log_{10}(l_z . S_{qq})$ spectra as the Baseline due to the counter-balancing effect between the S_{qq} and l_z. Whilst the l_z can be reduced by the Riblet, the corresponding S_{qq} actually undergoes an increase in level.

4.4. "Dynamic" Turbulent Boundary layer – analysis based on turbulent spots convecting over a Riblet surface

As introduced earlier in this chapter, the response of a turbulent boundary layer over a Riblet surface can be examined in the spatio-temporal domain when the turbulent spots are generated in an otherwise laminar boundary layer. The advantage of this analysis method is that it allows the tracking of the internal structure of an ensemble-averaged turbulence field in space and time. The quantities that will be used for the analysis are the velocity perturbation and r.m.s. velocity fluctuation, both of which have been defined in Chapter 3.

When measuring the laminar boundary layer on a Riblet surface, like the turbulent boundary layer, it also originates near the crest of the Riblet. The concept of virtual origin is also applied to the boundary layer velocity profiles, which is found to occur at about 0.66h below the riblet tip. This virtual origin is applicable to measurements conducted at $625 \leq x \leq 725$mm.

First, it is important to characterise the laminar boundary layer, which can be obtained from the conditionally averaged velocity profiles prior to the arrival of the turbulent spots. The ensemble-averaging of the velocity data pertaining to the laminar boundary layer is taken within the first 50ms after the spot is triggered. It is important to note that due to the probe length of 1.25mm, and that the distance between the Riblet tips is smaller than this, the aerodynamic flow data in the troughs between the Riblet tips is unavailable. Table 4.3 summarises the parameters pertaining to the laminar boundary layer at $625 \leq x \leq 725$mm for both the Baseline and Riblet cases. Note that in the experiments that measure the turbulent spots, the freestream velocity is set at $U_\infty = 7$m/s.

Location from L.E	Boundary Layer Thickness, mm δ	Displacement Thickness, mm δ^*	Momentum Thickness, mm θ	Shape Factor, $H = \frac{\delta^*}{\theta}$
625 mm	5.584, 5.529	1.610, 1.504	0.762, 0.730	2.113, 2.059
665 mm	5.638, 5.442	1.658, 1.503	0.764, 0.737	2.170, 2.040
705 mm	5.851, 5.241	1.689, 1.417	0.784, 0.723	2.154, 1.960
725 mm	5.702, 6.250	1.641, 1.955	0.770, 0.827	2.132, 2.365

Table 4.3 – Characteristics of the undisturbed laminar boundary layer over the Baseline plate and Riblet plate after the comma (taken about the virtual origin).

As expected, the boundary layer thicknesses over the flat plate grows steadily over the smooth Baseline surface. The growth of the boundary layer thicknesses over the Riblet surface fluctuates a bit over the longitudinal distance, and is less consistent. Whilst it could be due to error in the probe placement, it could also be a physical and genuine response of a laminar boundary layer when interacts with a Riblet. The ratio between the displacement thickness and momentum thickness is defined as the shape factor, H. The typical shape factor of a Blasius laminar boundary layer is H = 2.59. From Table 4.3, the shape factor is between $2.129 \leq H \leq 2.170$. Such a small deviation from the Blasius boundary layer could be due to the presence of small level of favourable pressure gradient along the flat plate surface.

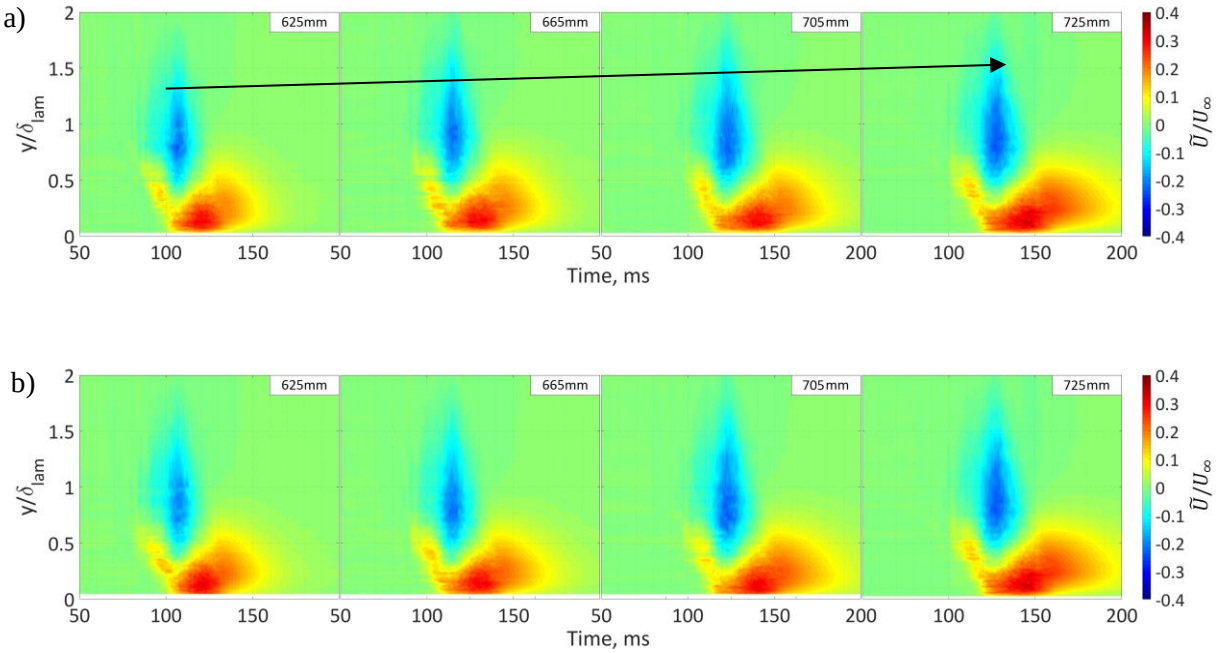

Figure 4.16 – Contours of the velocity perturbations of a turbulent spot at the plane of symmetry produced over a) Baseline, b) Riblet surface at 625 ≤ x ≤ 725mm

The attention now turns to the turbulent spots. In each measurement, 75 turbulent spots were triggered and ensemble-averaged to produce both the velocity perturbations and r.m.s. velocity fluctuations. More discussion about the analysis method can be found in Chapter 3. Figure 4.1616a represents the velocity perturbation contours of a turbulent spot at the plane of symmetry at $625 \leq x \leq 725$mm over the smooth Baseline plate. The spatio and temporal domains that encounter the velocity perturbation close to or equal to the value of zero denote the unperturbed laminar field. The ensemble-averaged turbulent spot displays *four* distinctive regions: (*1*) the near wall region that is dominated by the high level of positive perturbations, and (*2*) the outer region where the velocity perturbations are predominantly negative. This reflects very well of a typical turbulent boundary layer velocity profile that exhibits near wall velocity excess and outer layer velocity deficit. At some intermediate heights

from the surface, the turbulent spot will encounter both positive and negative perturbations along its length. These intermediate heights also coincide with the (*3*) leading edge overhang of the turbulent spot. Here, the leading edge overhang is formed by the upstream 'ejections' of turbulent fluid with sufficient energy from the near wall region to outside the laminar boundary layer. Although the ejected turbulent fluid propagates faster than the main body of the turbulent spot, it has no self-regeneration mechanism outside the boundary layer so it will gradually decay and join the nose of the turbulent spot to form an overhang. Another important feature pertaining to a turbulent spot that is discernible from the velocity perturbation contours is the presence of a (*4*) *calmed* region that corresponds to a slow recovery of velocity at the aft of each turbulent spot. The calmed region is formed by the downstream 'sweeping' of high momentum fluid from the freestream towards the near wall of the turbulent spot's trailing edge. From the perspective of the velocity perturbation, it is difficult to distinguish the boundary between the calmed region and the trailing edge of the turbulent spot. However, the calmed region has a fuller velocity profile that is even more stable than the local laminar boundary layer profile.

Figure 4.166a also shows the development of the turbulent spot at different streamwise locations between $625 \leq x \leq 725$mm. The turbulent spot can be seen to grow both in height and longitudinal length as it propagates downstream. Although not measured in this study, the turbulent spot is also expected to grow in width as it propagates downstream. As the measurement location increases, the arrival times of the turbulent spot's leading edge and trailing edge, respectively, also increase. A detection method of setting the velocity perturbation level to be ± 0.02 can be applied to identify the interface between the surrounding laminar fluid and the turbulent spot, which can then be used to calculate the propagation rate. It is found that the propagation rates of the leading edge and trailing edge of the spots are 0.83 and 0.52, respectively. This difference in the propagation rates provides the main mechanism to increase the longitudinal length of the turbulent spot. The overall shape of the velocity perturbation contours and their main features agree well with the existing literature (101) (102).

The next important step is to present the velocity perturbation contours pertaining to the convection of turbulent spots over the Riblet surface, and to compare them with those produced by the smooth Baseline surface. For the velocity perturbations produced by the Riblet surface in Figure 4.16b, there is no obvious difference, at least qualitatively, with those produced by the smooth Baseline surface in Figure 4.16a. The size and growth rate of the turbulent spot do not seem to be altered significantly by the Riblet.

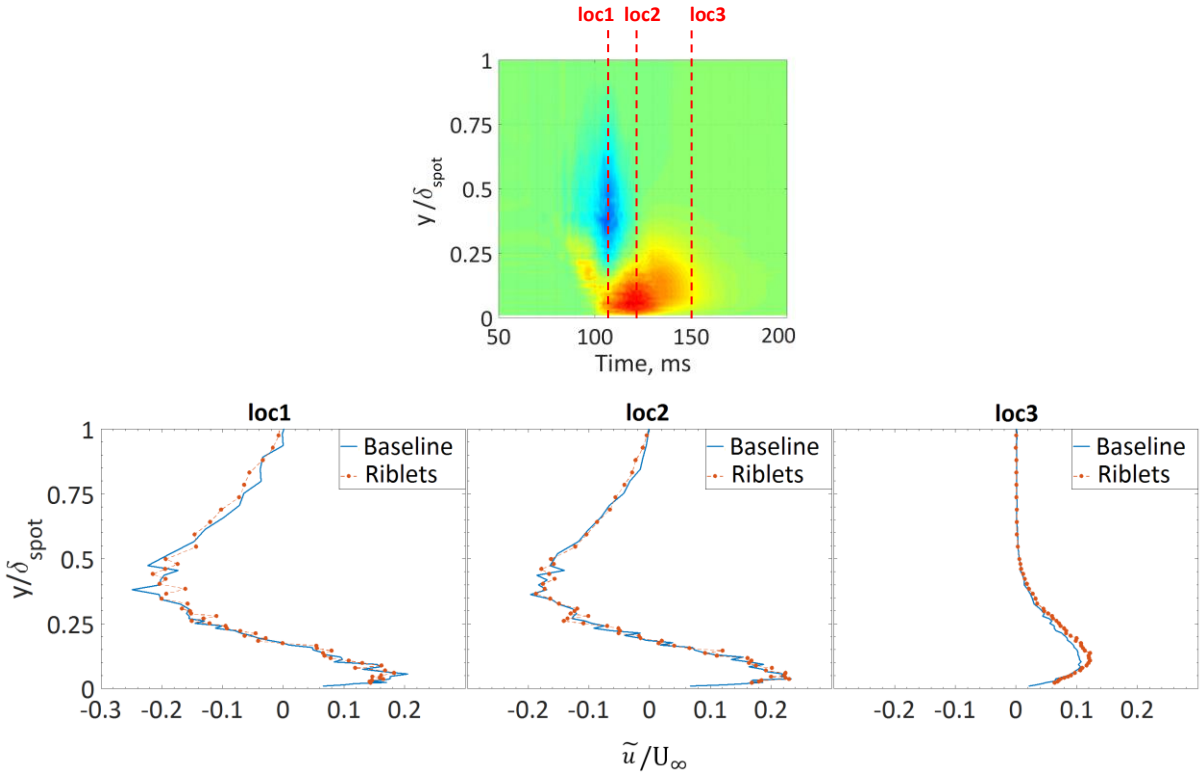

Figure 4.17 – Velocity perturbation at specific time locations for turbulent spot at 625mm downstream of leading edge.

To examine the results more quantitatively, Figure 4.17 compares the variation of the velocity perturbation in the non-dimensional vertical distance between the Baseline and Riblet cases at x = 625mm. δ_{spot} is the boundary layer thickness at the maximum height of the turbulent spot that occurs at loc2. The comparison is based on three time instances at t = 106, 120 and 150ms, which are denoted as loc1, loc2 and loc3, respectively. Note that loc1 is associated with the time instance pertaining to the maximum height of the turbulent spot, as well as where the largest level of negative perturbation occurs at the outer layer. loc2 corresponds to the time instance when the largest level of positive perturbation is recorded at the near wall region. Finally, loc3 corresponds to the calmed region of the turbulent spot. In line with the observation earlier, the velocity perturbation profiles at loc1 and loc2, both of which are in the main body of the turbulent spot, are very similar between the Baseline and Riblet cases. However, at loc3, the Riblet clearly demonstrate a larger peak of the positive velocity perturbation than the Baseline. This enhanced peak is also elevated further away from the Riblet surface. This suggests that when a turbulent spot is convecting over a Riblet surface, it can induce a stronger sweeping event and larger momentum flow to enhance the local stability of the boundary layer. This feature will be brought up again when the r.m.s. velocity fluctuation of the turbulent spot is discussed next.

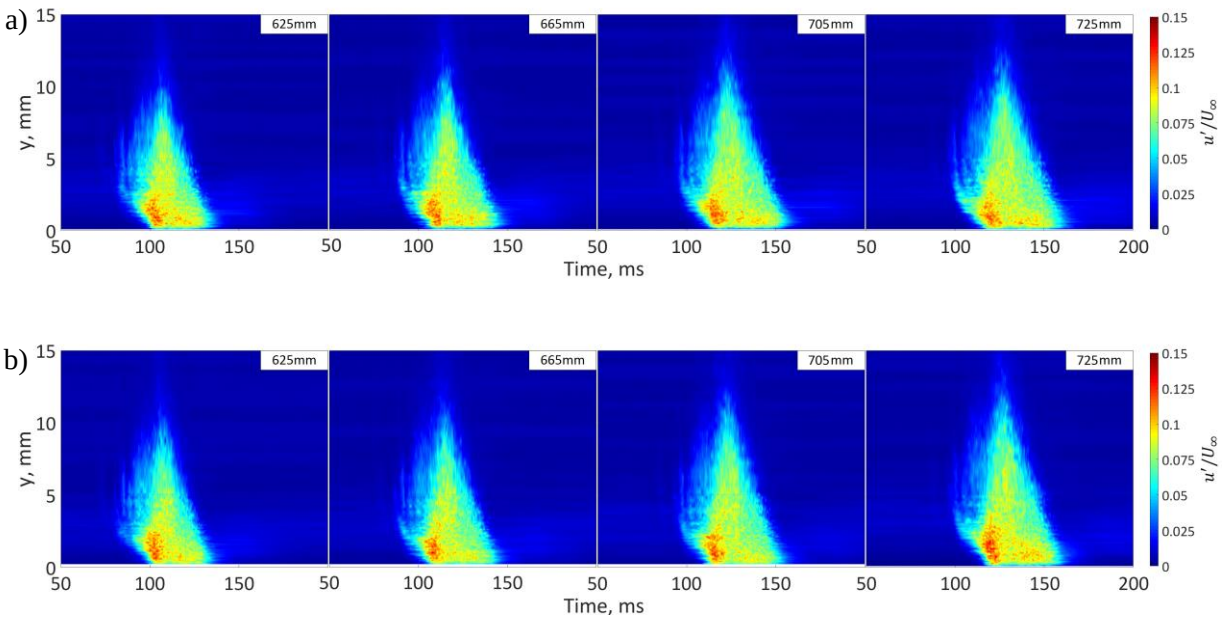

Figure 4.18 – Contours of the r.m.s. velocity fluctuations of a turbulent spot at the plane of symmetry produced over a) Baseline, b) Riblet surface at 625 ≤ x ≤ 725mm

Figure 4.18 shows the corresponding r.m.s velocity fluctuation contours for the same turbulent spot of both the Baseline and Riblet cases. The turbulent spot delineated by the turbulence intensity, though well defined, is quite different from that delineated by the velocity perturbation described earlier. Nevertheless, the salient features such as the leading edge, including its overhang, the maximum height and the trailing edge are all distinguishable from the r.m.s. velocity fluctuation contours. However, as expected, the calmed region is no longer discernible because by definition the turbulence intensity level at the calmed region should be very low.

The r.m.s velocity fluctuation shows that the leading edge at the near wall region, and underneath the overhang, is characterised by very high turbulence intensities between 10–14% (red colour). This region is herein referred to the 'primary turbulence intensity', which can also be found at other streamwise locations. The presence of a primary turbulence intensity within a turbulent spot is consistent with Gad-el-Hak *et al.* (29) and Glezer *et al.* (103) who observe that a strong destabilising regime is located at the leading edge interface under the overhang. This concentrated region is where the turbulence is produced, consistent with the earlier explanation of the near wall ejection of turbulent fluid that will eventually lead to the formation of a leading edge overhang. The presence of the primary turbulence intensity is needed for the destabilisation of the surrounding laminar boundary layer. High and concentrated 'secondary turbulence intensity' (8–10%, yellow-ish colour) is also found to encompass regions that would otherwise coincide with the prominent negative perturbation (at the outer layer, loc1) and positive perturbation (near wall, loc2) regions.

Qualitative comparison of the r.m.s. velocity fluctuation contours between the Baseline and Riblet cases, again, does not reveal significant difference between them. Both are similar in terms of the overall shape, dimension and footprint. However, closer examination does suggest that the secondary turbulence intensity at the near wall region is lower for the Riblet case at $625 \leq x \leq 705$mm. The reduction of the r.m.s. velocity fluctuation level coincides with the region of the near wall positive velocity perturbation (around loc2). At x = 725mm, both the primary and secondary turbulence intensity in the near wall region of the Riblet case undergo a sudden increase when compared to the upstream locations. This is because the turbulent spot has already reached the smooth surface (the Riblet ends at x = 710mm), where the turbulence regeneration mechanism reverts to that of the Baseline case.

$$\Omega(x,y) = \int_{t=0}^{t=300} \frac{\widetilde{U}(x,y,t)}{U_\infty(x)}\,dt$$

Equation 4.8

$$\Psi(x,y) = \int_{t=0}^{t=300} \frac{u'(x,y,t)}{U_\infty(x)}\,dt$$

Equation 4.9

As a summary, when a turbulent spot convects across a Riblet surface, it can result in an enhanced momentum at the calmed region but crucially it is not accompanied by increase in the turbulence level. In addition, inside the main body of the turbulent spot, the secondary turbulence intensity level also reduces compared to the smooth Baseline case. These two could be the contributing factors for the reduced turbulent velocity profiles for the Riblet case observed in Figure 4.3 for a fully developed turbulent boundary layer. However, the calmed region and the locations that coincide with the secondary turbulence intensity are both time and space dependent. Next, the time-averaged velocity perturbation Ω, and r.m.s. velocity fluctuations, Ψ, defined in Equation 4.8 and 4.9 respectively, can be investigated. By integrating these quantities in the time domain, it is possible to obtain a more generalised behaviour of the turbulent spot for the Baseline and Riblet cases. Note that the interval t = 0 and 300s will cover the entire turbulent spot, including that of the calmed region, at each measurement locations.

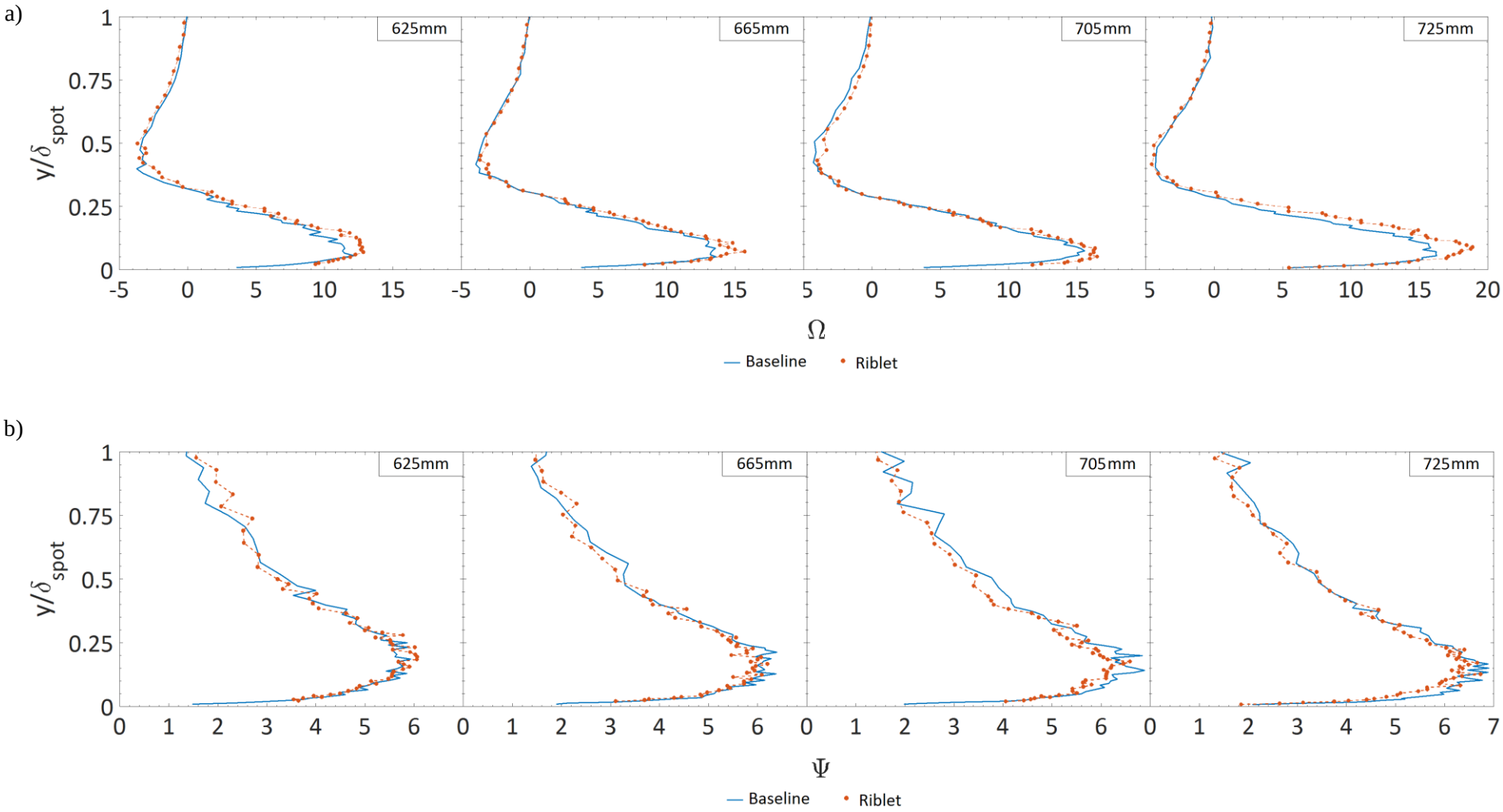

Figure 4.19 – Time integrated characteristics for the turbulent spot for a) Ω, b) Ψ at $625 \leq x \leq 725$mm

By examining the Ω in Figure 4.19a, the largest negative value of Ω occurs at $y/\delta_{spot} \approx 0.4$. This height is approximately located at the edge of the otherwise laminar boundary layer. The Ω profiles are predominantly negative at the outer layer, which remain quite similar between the Baseline and Riblet cases. When Ω becomes positive towards the wall, the Riblet slowly produces larger level of positive Ω compared those produced by the Baseline counterpart. The maximum Ω peak occurs at $y/\delta_{spot} \approx 0.1$, which could be the approximate limit of the viscous sublayer region. The main source of the larger Ω peak achieved by the Riblet is mainly by the increased momentum (but without the increase of turbulence intensity) at the calmed region.

Figure 4.19b shows that the maxima of Ψ occur at $y/\delta_{spot} \approx 0.2$, which is higher than where the Ω is located, and should correspond to the overlap region where the turbulence energy is transported from the inner to outer boundary layer. At x = 625mm, the Ψ profiles between the Baseline and Riblet are largely similar. At $665 \leq x \leq 725$mm, however, the Ψ profiles produced by the Riblets begin to deviate from the Baseline counterparts by showing a reduction, especially for the maxima level. This indicates that the turbulence energy production is reduced by the Riblets.

Turbulent spots are considered as the building blocks of a turbulent boundary layer. Before a fully developed turbulent boundary layer is established, the transitional boundary layer contains multiple turbulent spots that are generated randomly in space and time. As each turbulent spot is convecting downstream, it will grow in length, height and span. These growths will facilitate merging of the neighbouring turbulent spots, resulting in intermittent laminar and turbulent events. A fully developed turbulent boundary layer is only established when these turbulent spots are fully merged in space.

When the turbulent spots are convecting over a Riblet surface, two mechanisms can *collectively* cause an eventual reduction of the turbulent velocity profile in the case of a fully developed turbulent boundary layer (Figure 4.3). First, the enhanced momentum achieved at each turbulent spot's calmed region will mitigate the impact of turbulence merging with the neighbouring turbulent spots. Second, the secondary turbulence intensity level inside the turbulent spot's main body can be reduced directly by the Riblet surface, which is another factor that produces a lower turbulence intensity level for a fully developed turbulent boundary layer. Therefore, it can be concluded that a Riblet, at least the one designed and manufactured in the current study, had successfully reduced the velocity turbulence level and skin friction coefficient of a turbulent boundary layer. However, the level of turbulence reduction in the velocity field does not seem to replicate in the wall fluctuating pressure field. Based on the available data presented in this thesis, using a Riblet alone is not expected to result in considerable level of trailing edge noise reduction, unless it is incorporated with another control device to execute a multiple source targeting for the turbulent boundary layer. A combination of

Riblet with the Large Eddy BreakUp (LEBU) device has been investigated, where encouraging results are discussed in Section 5.5 of Chapter 5. Before that, Sections 5.3 and 5.4 in Chapter 5 will examine the response of the turbulent boundary layers and turbulent spots on the LEBU only.

4.5. Summary

The following bullet points summarise the main outcomes of this chapter:

- There are clear evidences that the Riblet change in the way that turbulence develops in the boundary layer, especially in the near wall region.

- For the turbulent boundary layer, the streamwise turbulence intensity was reduced by the Riblet, whilst the mean velocity increased. The Riblet can also reduce the turbulent boundary layer thicknesses.

- The Riblet is shown to reduce the skin friction coefficients of the turbulent boundary layer generated on a flat plate. The level of reduction is the greatest when the freestream velocity is low, while the level of reduction reduces when the freestream velocity increases. This suggests that the Riblet has operational limitations where the effectiveness of skin friction reduction can only be achieved over a finite range of the ratio between the Riblet height and the boundary layer displacement thickness.

- Whilst the convection velocities of the turbulent eddies remain unchanged between the Riblet and smooth Baseline surfaces, the Riblet exhibits a streamwise coherence function decline, which suggest that they can alter the turbulence structure in the convective field (i.e. its longitudinal structure). However, the Riblet may not change the fundamental turbulence re-generation mechanism significantly.

- The wall pressure power spectral density (S_{qq}) results show that the Riblet produces slight reduction of the spectral level at the low frequency, but increase at the mid-frequency range. The Riblet can reduce the lateral coherence length (l_z) of the turbulence across a large frequency range, including at low frequency.

- The product in the form of $10 \log_{10}(l_z . S_{qq})$ could provide a hint of the trailing edge noise radiation subjected to Riblet implemented on the surface. The results show that whilst the

Riblet can produce a lower value of 10 $\log_{10}(l_z . S_{qq})$ at low frequency, they remain largely unchanged at the mid and high frequencies compared to the Baseline due to the counter-balancing effect between the S_{qq} and l_z.

- The study of turbulent spot convecting over the Baseline and Riblet surfaces in the spatial and temporal domains provide an in-depth analysis of the fundamental turbulence reduction mechanisms by the Riblet. The results indicate that the reason a Riblet can reduce the turbulent velocity profile of a turbulent boundary layer is due to two factors. First, the enhanced momentum achieved at each turbulent spot's calmed region will mitigate the impact of turbulence merging with the neighbouring turbulent spots. Second, the internal turbulence level inside the turbulent spot's main body can be reduced directly by the Riblet surface.

- Whether or not Riblet is effective to reduce the trailing edge noise still requires further investigation and optimisation efforts. The evidences presented in this thesis on a single type of Riblet flair well in terms of low turbulence and low skin friction productions, but less effective on the aeroacoustics performances unless it is combined with another type of flow control device to achieve multiple source targeting.

Chapter 5 The effect of LEBU

5.1. Introduction

This chapter focusses on the aeroacoustics potential of the outer-layer flow control, Large Eddy BreakUp (LEBU) device. This passive device will be examined for its effectiveness in the manipulation of the fluctuating pressure field, which will provide useful information of whether it can be effective for the reduction of trailing edge noise. In order to provide a bit more detail about the effect of the wall-normal height of the LEBU on the fluctuating pressure field, two LEBU heights have been investigated.

Section 5.2 provides some scaling exercises for the LEBU geometry in terms of the undisturbed turbulent boundary layer parameters. The remainder of the chapter follows the same reporting format as Chapter 4. Section 5.3 investigates the effect of the LEBU on the fluctuating pressure field for a "stationary" turbulent boundary layer on a smooth surface. The effects of the LEBU are evaluated in their wall pressure spectra, streamwise/spanwise wall fluctuating pressure cross-correlations and coherence, and the partial hydrodynamic sources based on Amiet's model $10\log_{10}(l_z.S_{qq})$. It should be noted that the LEBU is positioned in various upstream locations with respect to the reference remote microphone sensor at $x_{\mathrm{ref}} = 625\mathrm{mm}$. Examination of the flow interaction between the turbulent spot and LEBU in the spatial and temporal domains will be performed in Section 5.4. The aim of this sub-section is to provide some insights of the turbulence interaction and mechanisms that produce the wall pressure spectra and correlation fields as observed in Section 5.3.

The last section this chapter (Section 5.5) is dedicated to the results of a preliminary study on the combined use of Riblet and LEBU. The aim of this investigation is to determine whether utilising both devices, which target the near wall and outer layer respectively, could deliver a further suppression of the turbulent characteristics of the boundary layer.

5.2. Scaling of the LEBU by the Turbulent Boundary Layer at x_{ref}

The aforementioned LEBU "height" refers to the vertical placement of the LEBU with respect to the wall surface. As the results later show, the height can affect significantly its effectiveness as a drag reduction device. This is a logical outcome considering that the LEBU height will be underpinned by the local boundary layer thickness. Two LEBU heights are chosen in the current work – one is 2.5mm above the wall surface, and another one is 5mm above. For reference purposes, these will be labelled as $\mathrm{LEBU}_{2.5}$ and $\mathrm{LEBU}_{5.0}$, respectively. The height, $\tilde{h}$ and chord length C_{LEBU} of the LEBU are normalised by the Baseline boundary layer thickness δ_{ref} at the reference location, $x_{\mathrm{ref}} = 625\mathrm{mm}$. In addition, the height is also scaled in a wall unit $\tilde{h}^{+} = \frac{\tilde{h}u_{\tau}}{\nu}$ to indicate the vertical location of the LEBU with respect to the different zones of the turbulent boundary layer at X_{ref}. However, the readers should take note that the $\tilde{h}$ will maintain the same physical distance relative to the wall when it is moved upstream. The values are tabulated in Table 5.1.

	$\mathrm{LEBU}_{2.5}$			$\mathrm{LEBU}_{5.0}$		
	10	12	15	10	12	15
$\tilde{h}^{+}$	84.667	99.500	120.833	169.333	199.000	241.667
$\frac{\tilde{h}}{\delta_{ref}}$	0.220	0.230	0.238	0.440	0.461	0.476
$\frac{C_{LEBU}}{\delta_{ref}}$	1.321	1.382	1.428	1.321	1.382	1.428

Table 5.1 – Normalised LEBU height and chord length by the Baseline turbulent boundary layer properties at $X_{ref} = 625mm$.

From the table, the LEBU achieves $\tilde{h}/\delta_{\mathrm{ref}}$ between 0.2 and 0.5. This range is found to be lower than the suggested optimal placement at $\tilde{h}/\delta \approx 0.8$ for a tandem LEBU configuration, but close to the suggested optimal value for a single plate LEBU which can provide good skin friction reduction (50) (104) (105) (106) (107). From the values in 5.1, the $\tilde{h}^{+}$are predominantly larger than 50. This

indicates that despite the LEBU locating at different positions upstream of the X_{ref}, the wake generated by these LEBU will propagate to the outer layer region of the turbulent boundary layer at X_{ref}.

$x_{ref} - x_{LEBU}$	5 mm	15 mm	30 mm	50 mm	80 mm
$(x_{ref} - x_{LEBU})/\delta_{ref}$ 10m/s	0.440	1.321	2.643	4.405	7.047
$(x_{ref} - x_{LEBU})/\delta_{ref}$ 12m/s	0.461	1.382	2.763	4.605	7.369
$(x_{ref} - x_{LEBU})/\delta_{ref}$ 15m/s	0.476	1.428	2.856	4.761	7.617

Table 5.2 – LEBU location normalised by the Baseline turbulent boundary layer thickness

As mentioned earlier, both the $\mathrm{LEBU}_{2.5}$ and $\mathrm{LEBU}_{5.0}$ will be positioned at several distances upstream of the x_{ref}, which can be represented by $(x_{\mathrm{ref}} - x_{\mathrm{LEBU}})$. Here, x_{LEBU} = 620, 610, 595, 575 and 545mm. Therefore, the values of $(x_{\mathrm{ref}} - x_{\mathrm{LEBU}})$ investigated here are 5, 15, 30, 50, and 80mm, respectively. Table 5.2 summarises the normalised streamwise locations of the LEBU in the context of $(x_{\mathrm{ref}} - x_{\mathrm{LEBU}})/\delta_{\mathrm{ref}}$ at U_∞ = 10, 12 and 15m/s. From the table, it shows that the LEBU is moved upstream of x_{ref} between 0.4 and $7.5\delta_{\mathrm{ref}}$, which should provide a good coverage for the investigation of the LEBU's effectiveness.

5.3. "Stationary" Turbulent Boundary Layer – analysis on the wall pressure fluctuations

5.3.1. Power Spectral Density

The surface pressure Power Spectral Density (PSD) downstream of the $\mathrm{LEBU}_{2.5}$ is presented in Figure 5.1. The dashed lines in the figures represent the PSD from the Baseline turbulent boundary layer without the presence of the LEBU. In addition to the X_{ref} (i.e. x = 625mm), the wall pressure PSD are also presented at other two measurement locations at x = 645 and 665mm. The effects of the upstream placement of the $\mathrm{LEBU}_{2.5}$ as per the Table 5.2 are presented. Figure 5.1 also contains the wall pressure PSD generated at U_∞ = 10, 12 and 15m/s.

The case of U_∞ = 10m/s for x = 625mm (x_{ref}) will be examined first. When the LEBU is placed at $(x_{\mathrm{ref}} - x_{\mathrm{LEBU}})/\delta_{\mathrm{ref}}$ = 0.440, the microphone at x_{ref} encounters the near wake generated by the LEBU

directly. There is a clear increase in the PSD level at $0.2 \leq f < 2$kHz compared to the Baseline case where up to 10 dB difference can be observed. Further upstream placement of the $LEBU_{2.5}$, i.e. $(x_{ref} - x_{LEBU})/\delta_{ref} \geq 1.321$, will still produce a higher PSD level at low frequency, but they gradually become closer to the level of the Baseline case. This is an expected outcome because a further upstream placement of the $LEBU_{2.5}$ will reduce the level of wake–turbulent boundary layer interaction at x_{ref}. Now back to the nearest placement of the $LEBU_{2.5}$ at $0.440\delta_{ref}$, there is a sharper decay in the wall pressure PSD level ($\sim f^{-7}$) compared to that of the Baseline case (f^{-5}). This indicates that the near wake produced by the $LEBU_{2.5}$ can cause a faster energy dissipation at the high frequency region. Interestingly, this is the only instance a reduction of the wall pressure PSD level against the Baseline case can be observed. In other words, the LEBU can indeed increase the rate of turbulence breakdown in the high frequency range, and is the most effective when the LEBU is closest to the microphone at x_{ref}. At further upstream placement of the $LEBU_{2.5}$, i.e. $(x_{ref} - x_{LEBU})/\delta_{ref} \geq 1.321$, the high frequency decay seems to revert to the f^{-5} decay rate. Furthermore, the wall pressure PSD level are generally slightly above that produced by the Baseline.

With the same $LEBU_{2.5}$ placements at $0.440 \leq (x_{ref} - x_{LEBU})/\delta_{ref} \leq 7.047$, the wall pressure PSD at the downstream measurement locations at x = 645 and 665mm are also investigated. The increased PSD level at low frequency produced by the $LEBU_{2.5}$ is still present but the difference against the Baseline case becomes less significant. The same trend is also observed for the high frequency range where the wall pressure spectra produced by the $LEBU_{2.5}$ gradually conform to the Baseline spectra. More specifically, when the $LEBU_{2.5}$ is placed upstream, it will encounter thinner boundary layer and larger effective $\tilde{h}^+$ locally. This would mean that the LEBU is targeting a higher point in the outer layer than what is stated in Table 5.1. At x = 645mm, even when the $LEBU_{2.5}$ is placed at the furthest location at $(x_{ref} - x_{LEBU})/\delta_{ref} = 7.047$, the corresponding wall pressure PSD level appears to be similar to other $(x_{ref} - x_{LEBU})/\delta_{ref}$ locations. The same trend is also observed at x = 665mm. As a summary, when the LEBU is placed at a vertical height near the wall surface ($LEBU_{2.5}$):

1. the wake it produces can enhance the larger turbulence structure across a considerable x distance downstream (reflected in the low frequency spectra),
2. it can also enhance the smaller turbulence structure (reflected in the high frequency spectra), slightly, but the effect is not as significant as the large turbulence structure,
3. the most signification manipulation of the wall pressure fluctuation field occurs at about $(x_{ref} - x_{LEBU})/\delta_{ref} = 0.44$, where large levels of turbulent energy spectra increase and decrease at the low and high frequency regions, respectively, are observed. This indicates that the otherwise canonical turbulent boundary layer at the near field of the LEBU has been manipulated significantly.

At a slightly higher freestream velocity of U_∞ = 12m/s, the trends still hold true, although the deviation against the Baseline becomes slightly less. To provide some explanations to the above phenomena, Dowling (108) found that the introduction of a LEBU can add additional dipole sources into the pressure field, which is the most evident for the surface pressure field directly beneath or nearby the LEBU due to the flow suction. She also noticed that this effect gradually dissipated at downstream distance from the LEBU. The results of the $LEBU_{2.5}$ thus far indicate that this phenomenon is applicable when U_∞ = 10 and 12m/s.

However, at U_∞ = 15m/s and x = 625mm (x_{ref}), there seems to be a deviation from the trend where the large scale turbulence structures at low frequency are subjected to less enhancement from the $LEBU_{2.5}$. At high frequency, the upstream placement of the $LEBU_{2.5}$ for $(x_{\mathrm{ref}} - x_{\mathrm{LEBU}})/\delta_{\mathrm{ref}} \geq 2.856$ can even achieve reduction in the wall pressure PSD level compared to the Baseline counterpart. However, at other downstream measurement locations of x = 645 and 665mm, the variations of the wall pressure PSD pertaining to the $0.476 \leq (x_{\mathrm{ref}} - x_{\mathrm{LEBU}})/\delta_{\mathrm{ref}} \leq 7.617$ do not follow a clear pattern, although the reduction in the wall pressure PSD level at $(x_{\mathrm{ref}} - x_{\mathrm{LEBU}})/\delta_{\mathrm{ref}} \geq 2.856$ by the $LEBU_{2.5}$ is still consistently demonstrated.

Figure 5.2 are based on a very similar format as Figure 5.1, except that the wall pressure PSD are now produced by the $LEBU_{5.0}$. When comparing the spectra between Figure 5.1 and Figure 5.2, different characteristics of the wall pressure PSD are readily discernible. When the $LEBU_{5.0}$ is nearby the reference measurement location at x = 625mm (x_{ref}), i.e. $0.44 \leq (x_{\mathrm{ref}} - x_{\mathrm{LEBU}})/\delta_{\mathrm{ref}} \leq 1.428$, the near wake interaction with the turbulent boundary layer can result in a very significant enhancement of the wall pressure PSD across the entire frequency of interest. This phenomenon is consistent across all the freestream velocities investigated here at U_∞ = 10, 11 and 12m/s. A direct consequence of this spectral enhancement is the increase of the overall turbulence intensity of the velocity field, which is detrimental from the aeroacoustical point of view. However, if the $LEBU_{5.0}$ is moved upstream to $2.643 \leq (x_{\mathrm{ref}} - x_{\mathrm{LEBU}})/\delta_{\mathrm{ref}} \leq 2.856$, while the measurement position is retained at x = 625mm (x_{ref}), the corresponding wall pressure PSD undergo a swift transition to align with that of the Baseline's. Further upstream placement of the $LEBU_{5.0}$ to $4.405 \leq (x_{\mathrm{ref}} - x_{\mathrm{LEBU}})/\delta_{\mathrm{ref}} \leq 7.617$ results in an interesting phenomenon, where the corresponding wall pressure PSD follow a higher decay rate of f^{-1} instead of the $f^{-0.5}$ for the Baseline. In addition, the $f^{-5/3}$ scaling for the mid frequency also tends towards the low frequency region. These changes in the decay rates indicate that the $LEBU_{5.0}$ can fundamentally disrupt the cascade of the turbulence length scales. More importantly, while similar in the wall pressure PSD level at $f \leq$ 600Hz, the $LEBU_{5.0}$ can cause a reduction at $f >$ 600Hz compared to the Baseline level.

When the measurement point is moved downstream to x = 645mm, the phenomena described in the previous paragraph still hold true, except that it is now more resistant to the increase of the wall pressure PSD level when the LEBU5.0 is nearby. When the measurement point further increases to x = 665mm, the wall pressure PSD become even less sensitivity to the streamwise location of the $LEBU_{5.0}$ but they exclusively achieve reduction against the Baseline at f > 600Hz, and collapse with the Baseline at $f \leq$ 600Hz.

From the results discussed thus far, the $LEBU_{5.0}$ is more effective than the $LEBU_{2.5}$ in disrupting the turbulent energy transfer from the large to small scale without having to affect the large scale turbulence structure significantly. It is also clear that the $LEBU_{5.0}$ is most effective when it is located further upstream from the point of interest. From the results in Figure 5.1 and 5.2, when placed at reasonably upstream of an aerofoil trailing edge, the $LEBU_{5.0}$ has a potential to achieve self-noise reduction due to the lower wall pressure PSD level at the mid and high frequency. However, as already demonstrated in Chapter 4, the radiated self-noise is also dependent on other hydrodynamic sources, such as the spanwise coherence length scale. A more complete investigation of the aeroacoustics performance by the LEBU will be conducted in Section 5.3.3.

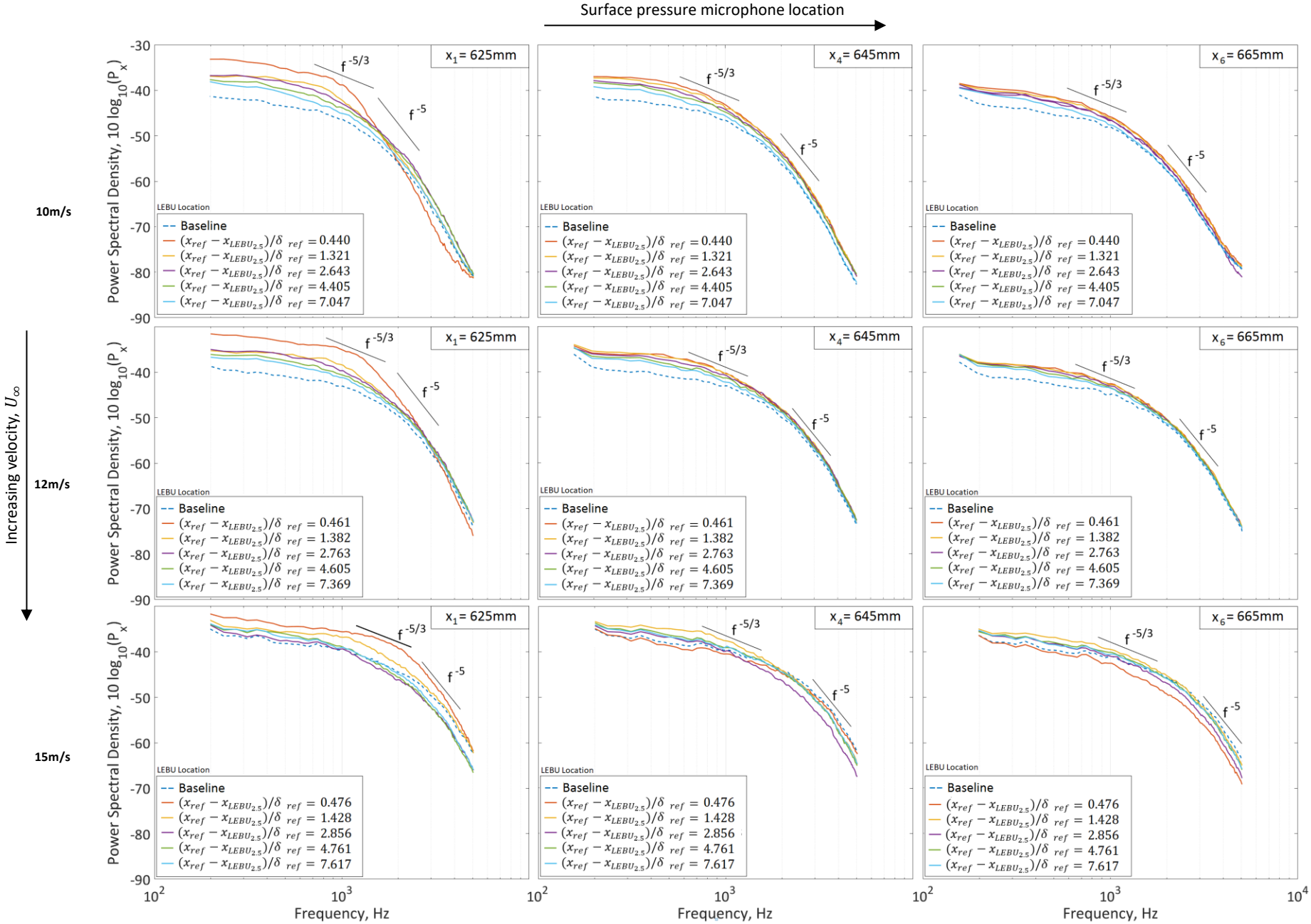

Figure 5.1 –Baseline and $LEBU_{2.5}$ surface pressure PSD comparison

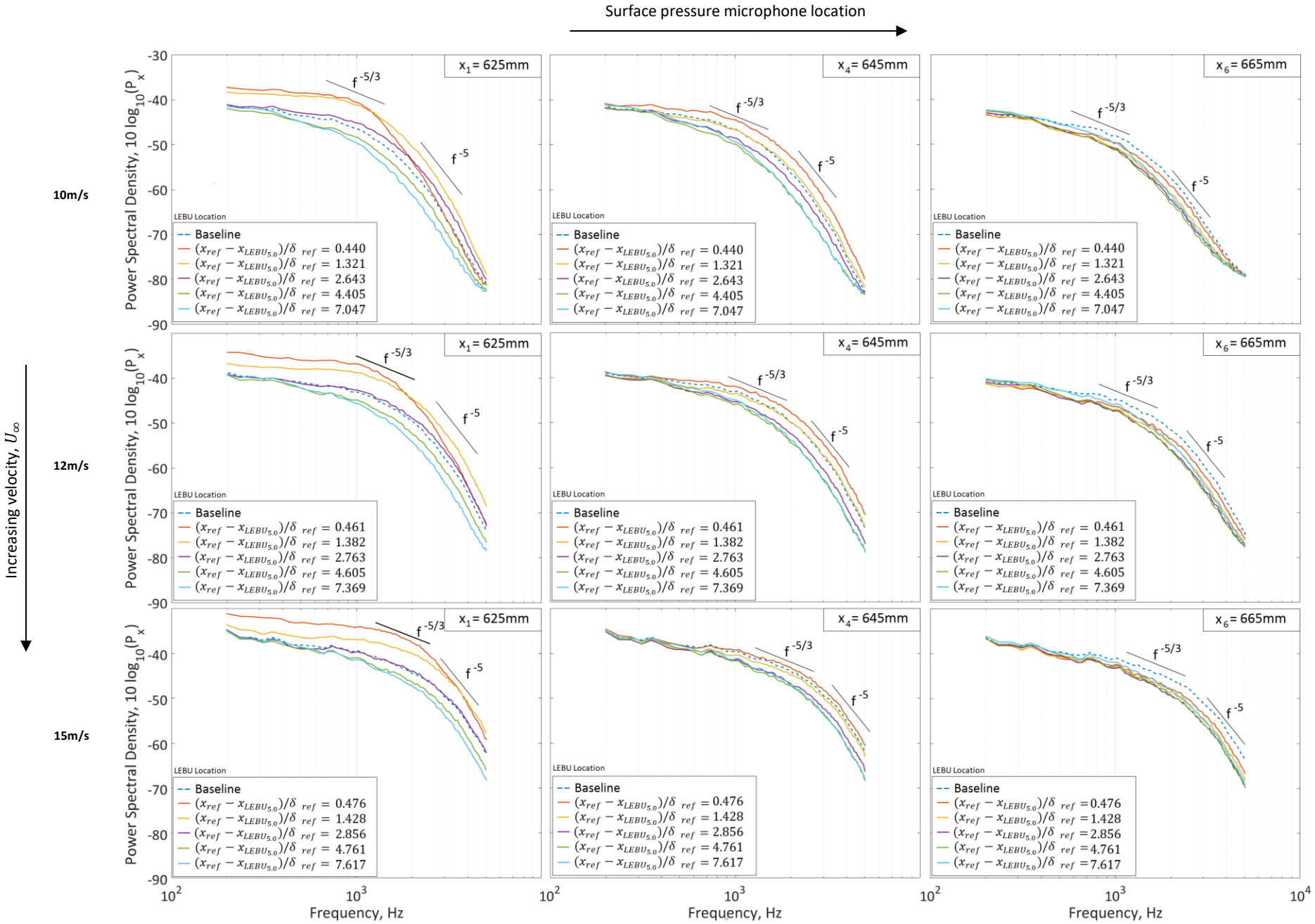

Figure 5.2 –Baseline and $LEBU_{5.0}$ surface pressure PSD comparison

5.3.2. Streamwise cross-correlation

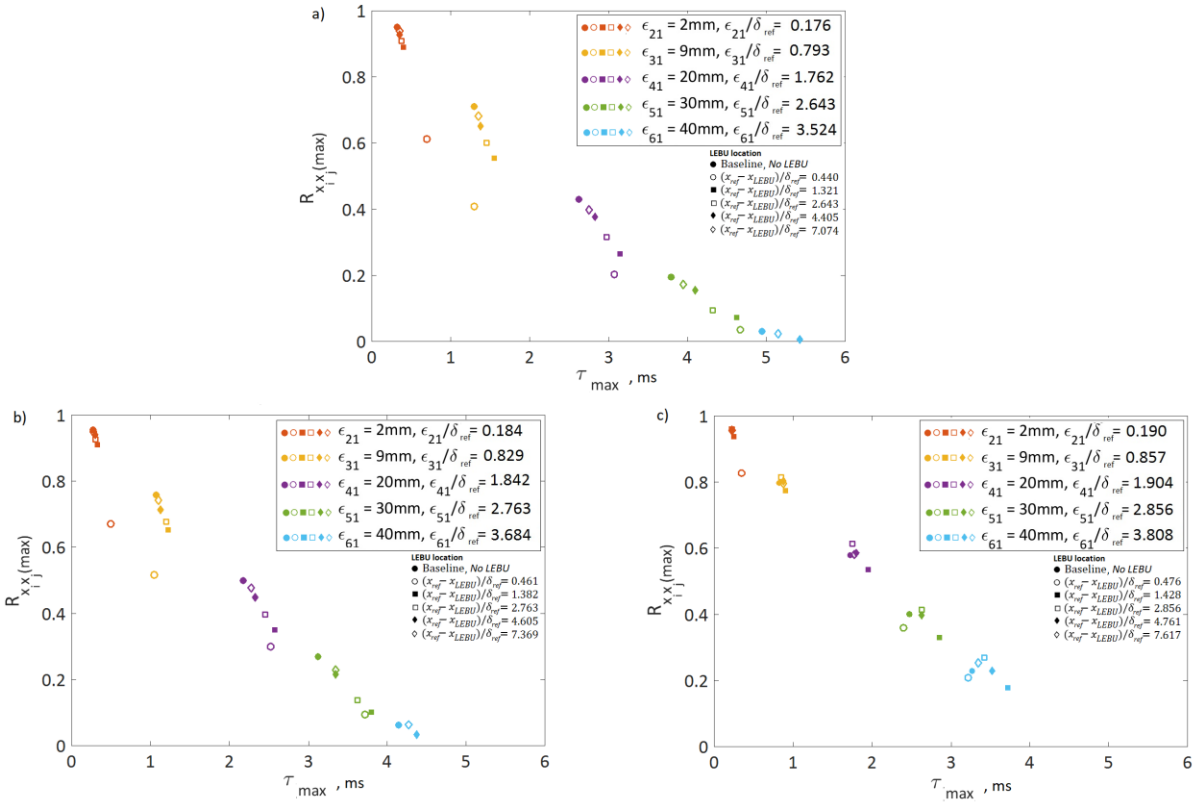

Figure 5.3 – Comparison of streamwise cross-correlation maxima for Baseline and LEBU$_{2.5}$ at a) 10m/s, b) 12m/s and c) 15m/s

Definition of the streamwise cross-correlation has already been provided in Section 4.3.2 of the previous chapter. Figure 5.3 shows the cross-correlation coefficients for the Baseline and the LEBU$_{2.5}$ at various upstream placements of $(x_{\text{ref}} - x_{\text{LEBU}})/\delta_{\text{ref}}$. Compared to the Baseline, the greatest correlation decay corresponds to when the LEBU$_{2.5}$ is at $(x_{\text{ref}} - x_{\text{LEBU}})/\delta_{\text{ref}}$ = 0.440–0.476. This observation is true for U_∞ = 10, 12 and 15m/s. The almost 40% correlation loss is mainly due to the direct near wake interaction with the propagating turbulent eddies. When the LEBU is moved upstream, the mechanism of direct near wake interaction becomes weakened. The ϵ_{11} is no longer inside the near wake region, which will not experience a strong perturbation like the previous case. This suggest that the wake is dissipated and become less influential at larger separation distance between the microphones.

It is clear that whenever the LEBU$_{2.5}$ is utilised, it will consistently produce lower value of the cross-correlation coefficients compared to those produced by the Baseline. Nevertheless, when the LEBU$_{2.5}$ is moved further upstream, the values of the cross-correlation coefficient will become closer to the

Baseline's values. There is a trend that the loss of cross-correlation coefficients becomes less pronounced when the freestream velocity increases.

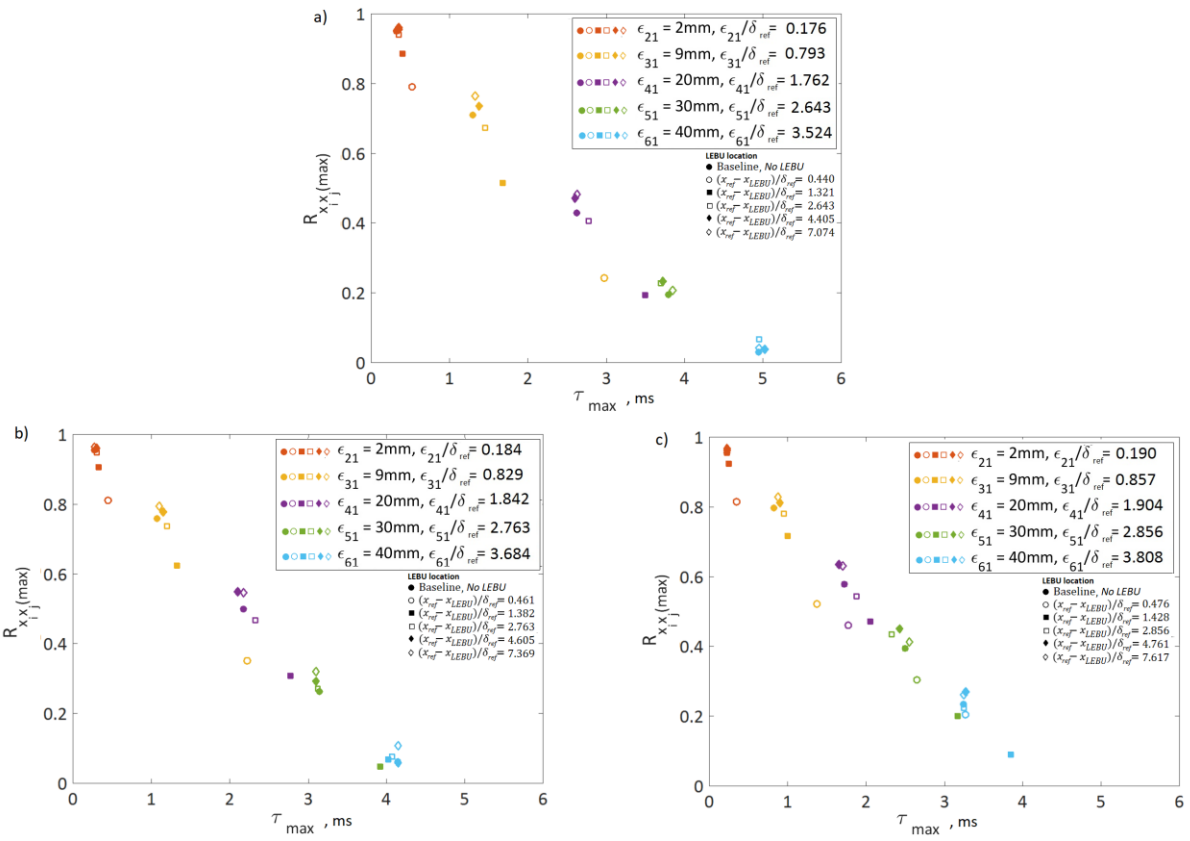

Figure 5.4 – Comparison of streamwise cross-correlation maxima for Baseline and LEBU$_{5.0}$ at a) 10m/s, b) 12m/s and c) 15m/s

A similar analysis is conducted for the streamwise cross-correlation coefficients produced by the LEBU$_{5.0}$, which is shown in Figure 5.4. From the overall trend of each graph (Figure 5.4a – c), as the freestream velocity increases, the rate of cross-correlation coefficient decay as the result of near wake interaction (underpinned by low value of $(x_{\text{ref}} - x_{\text{LEBU}})/\delta_{\text{ref}}$) becomes less severe.

Adopting the similar analysis technique used in Chapter 4, the convection velocities of the turbulent eddies can be calculated by the gradients of the linear fit for the ε against τ_{max}. The collection of data is shown in Figure 5.5 for both the LEBU$_{2.5}$ and LEBU$_{5.0}$. A summary of the convection velocity is tabulated in Table 5.3.

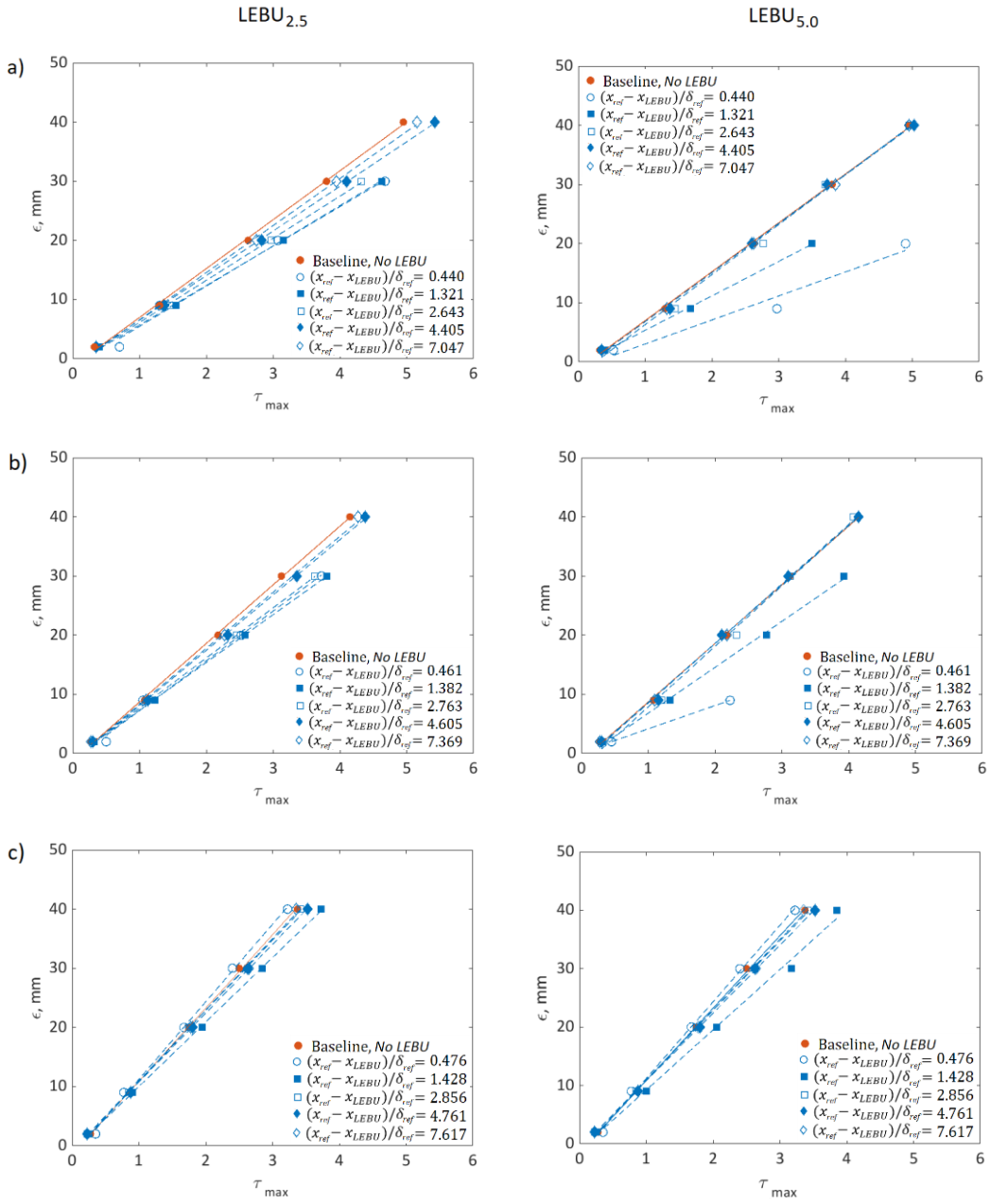

Figure 5.5 – Convection velocities for $LEBU_{2.5}$ and $LEBU_{5.0}$ at a) 10m/s, b) 12m/s and c) 15m/s

A quick glance in Figure 5.5 can already reveal different gradients for the best fit lines, which represents a clear indication that the LEBU can affect the propagation speeds of the turbulent eddies. More specifically, for the $LEBU_{2.5}$ at $U_\infty = 10m/s$ and $U_\infty = 12m/s$, the lowest convection velocity is witnessed in the lowest $(x_{\text{ref}} - x_{\text{LEBU}})/\delta_{\text{ref}}$, which denotes the most downstream location of the LEBU. The gradient then recovers towards the Baseline's when $(x_{\text{ref}} - x_{\text{LEBU}})/\delta_{\text{ref}}$ increases, i.e. the $LEBU_{2.5}$ is moved to more upstream distance. This could be directly related to the presence of stronger near wake interaction when $(x_{\text{ref}} - x_{\text{LEBU}})/\delta_{\text{ref}}$ is small. Since the wake is also in closer proximity to the wall (compared to the $LEBU_{5.0}$), there is an expectation that a significant wall-wake interaction can

hamper the streamwise development of the turbulent eddies. As the $LEBU_{2.5}$ is moved upstream, the wake becomes less intense when it arrives the measurement points. Therefore, the convection velocity of the turbulent eddies recovers. Interestingly, for the $LEBU_{5.0}$ case, despite the level of wall-wake interaction will be less intense since it is further away from the wall surface, the propagation rates of the turbulent eddies are hampered even more significantly at the low $(x_{\mathrm{ref}} - x_{\mathrm{LEBU}})/\delta_{\mathrm{ref}}$. However, the recover to the Baseline values is also much faster when the $(x_{\mathrm{ref}} - x_{\mathrm{LEBU}})/\delta_{\mathrm{ref}}$ increases. This trend bears some degrees of resemblance to the wall pressure PSD (discussed in the previous section) for the $LEBU_{5.0}$ in that the manipulation of the turbulent boundary layer is more significant at $(x_{\mathrm{ref}} - x_{\mathrm{LEBU}})/\delta_{\mathrm{ref}} \leq 1.428$, but a quick recovery will follow when the $(x_{\mathrm{ref}} - x_{\mathrm{LEBU}})/\delta_{\mathrm{ref}}$ increases further.

	$LEBU_{2.5}$									
$x_{ref} - x_{LEBU}$ (mm)	5		15		30		50		80	
U_∞	u_c (m/s)	u_c/U_∞	u_c (m/s)	u_c/U_∞	u_c (m/s)	u_c/U_∞	u_c (m/s)	u_c/U_∞	u_c (m/s)	u_c/U_∞
10m/s	6.417	0.642	6.627	0.663	7.089	0.709	7.488	0.749	7.917	0.792
12m/s	8.054	0.671	8.058	0.672	8.421	0.702	9.325	0.777	9.500	0.792
15m/s	12.403	0.827	10.935	0.729	11.875	0.792	11.515	0.768	12.160	0.811
	$LEBU_{5.0}$									
$x - x_{LEBU}$ (mm)	5		15		30		50		80	
U_∞	u_c (m/s)	u_c/U_∞	u_c (m/s)	u_c/U_∞	u_c (m/s)	u_c/U_∞	u_c (m/s)	u_c/U_∞	u_c (m/s)	u_c/U_∞
10m/s	3.025	0.303	5.714	0.571	8.261	0.826	8.128	0.813	8.261	0.826
12m/s	4.045	0.337	7.778	0.648	9.912	0.826	9.870	0.823	9.806	0.817
15m/s	12.653	0.844	10.556	0.704	11.875	0.792	11.515	0.768	12.160	0.811

Table 5.3 – Summary of convection velocities for $LEBU_{2.5}$ and $LEBU_{5.0}$

5.3.3. Streamwise Coherence

The streamwise coherence is investigated here. The results for the $LEBU_{2.5}$ are presented in Figure 5.6. From examining the coherence for all velocities where $(x_{ref} - x_{LEBU})$ = 5mm, for ϵ_{21} there is a large drop in coherence across all frequencies when compared to the Baseline. Since ϵ_{11} (which is the reference microphone located at x = 625mm, x_{ref}) is located inside the near wake region, this shows that the turbulence structure profiles change significantly in the near wake. This suggests that the presence of the $LEBU_{2.5}$ has a very strong destructive effect on the turbulence structures in the near wake. Since there a such a strong reduction in coherence between ϵ_{11} and ϵ_{21}, the downstream

streamwise coherences between ϵ_{21} and ϵ_{61} would hold almost no coherence level compared to the reference location. This is shown throughout the freestream velocity cases when the $LEBU_{2.5}$ is placed at $(x_{ref} - x_{LEBU})$ = 5mm.

As the $LEBU_{2.5}$ is moved further upstream to $(x_{ref} - x_{LEBU})$ = 15mm, the reference microphone is in a more dissipated wake region. The streamwise coherence in the low frequency range between 0.2 – 1kHz shows level closer to the Baseline. This indicates that the decay rate of the streamwise coherence as a function of the frequency are similar to the Baseline decay rates. At f > 1kHz, there is still a considerable reduction in the streamwise coherence level, but not as significant as the previous case. This indicates that the measurement point is now away from the near-wake from the $LEBU_{2.5}$. The ϵ_{21} still exhibits less streamwise coherence level than it would compared to the Baseline, indicating that there is a turbulence disruption in the wake of the $LEBU_{2.5}$.

As the $LEBU_{2.5}$ is moved further upstream to $(x_{ref} - x_{LEBU})$ = 80mm, the streamwise coherence is reverting to the Baseline level. This shows that at a certain point, the effect of the $LEBU_{2.5}$ on the turbulence dissipation becomes weaker and the turbulent boundary layer downstream of the $LEBU_{2.5}$ re-establishes to its canonical characteristics.

Generally, the phenomena described above also apply to the $LEBU_{5.0}$ in Figure 5.7, although some subtle differences still exist. From these streamwise coherence results, both the $LEBU_{2.5}$ and $LEBU_{5.0}$ show that turbulent boundary layers subjected to the LEBU treatment have similar dominant frequency composition to the Baseline turbulent boundary layer. The $LEBU_{2.5}$ follows the streamwise coherence levels of the Baseline case more closely, especially when the LEBU is nearby, e.g. $(x_{ref} - x_{LEBU})$ = 5mm. The $LEBU_{5.0}$, on the other hand, shows a marked decrease in the streamwise coherence level when the $LEBU_{5.0}$ is at $(x_{ref} - x_{LEBU})$ between 30 and 50mm.

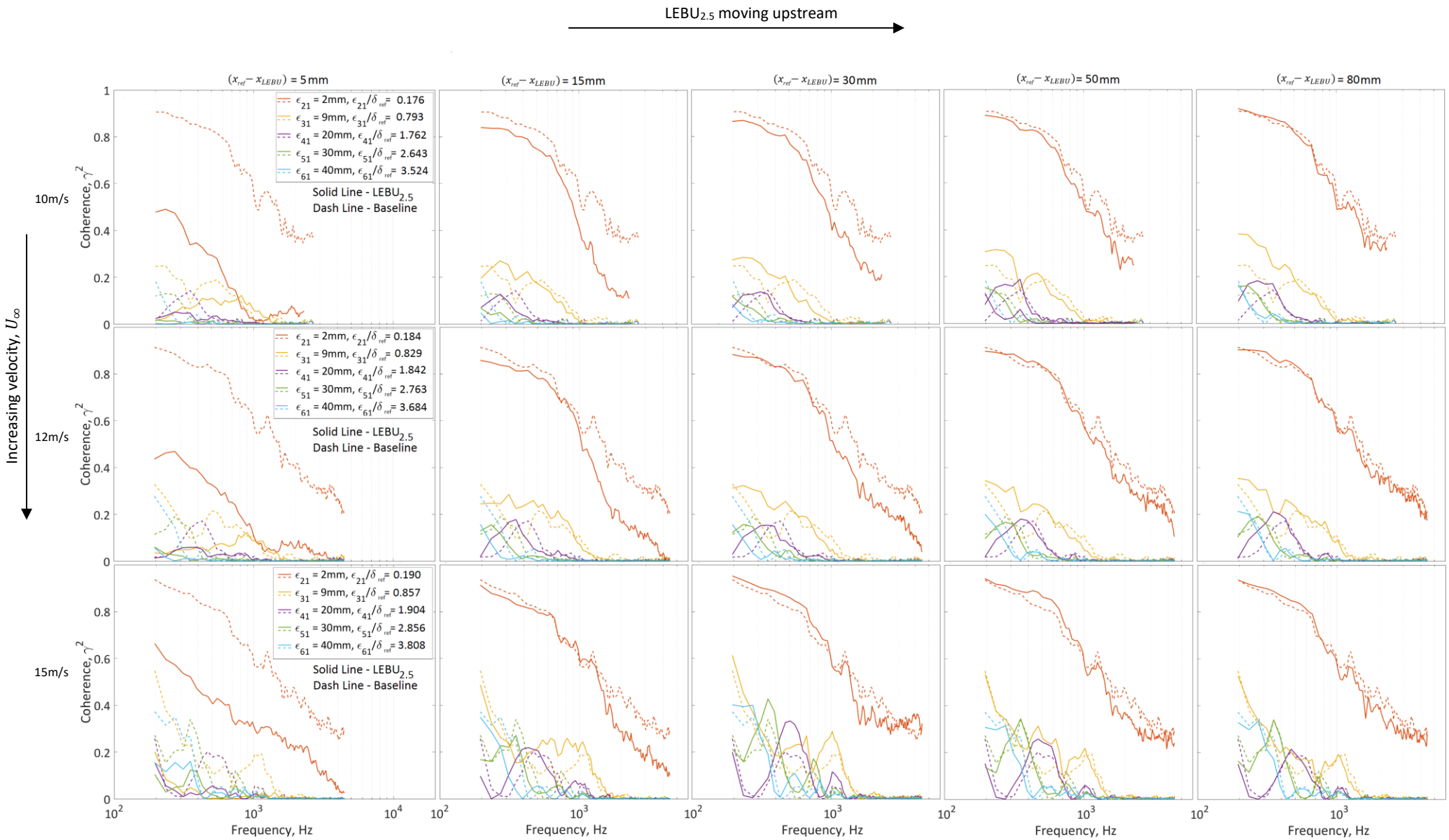

Figure 5.6 – Comparison of Baseline and LEBU$_{2.5}$ streamwise coherence at a) 10m/s, b) 12m/s and c) 15m/s

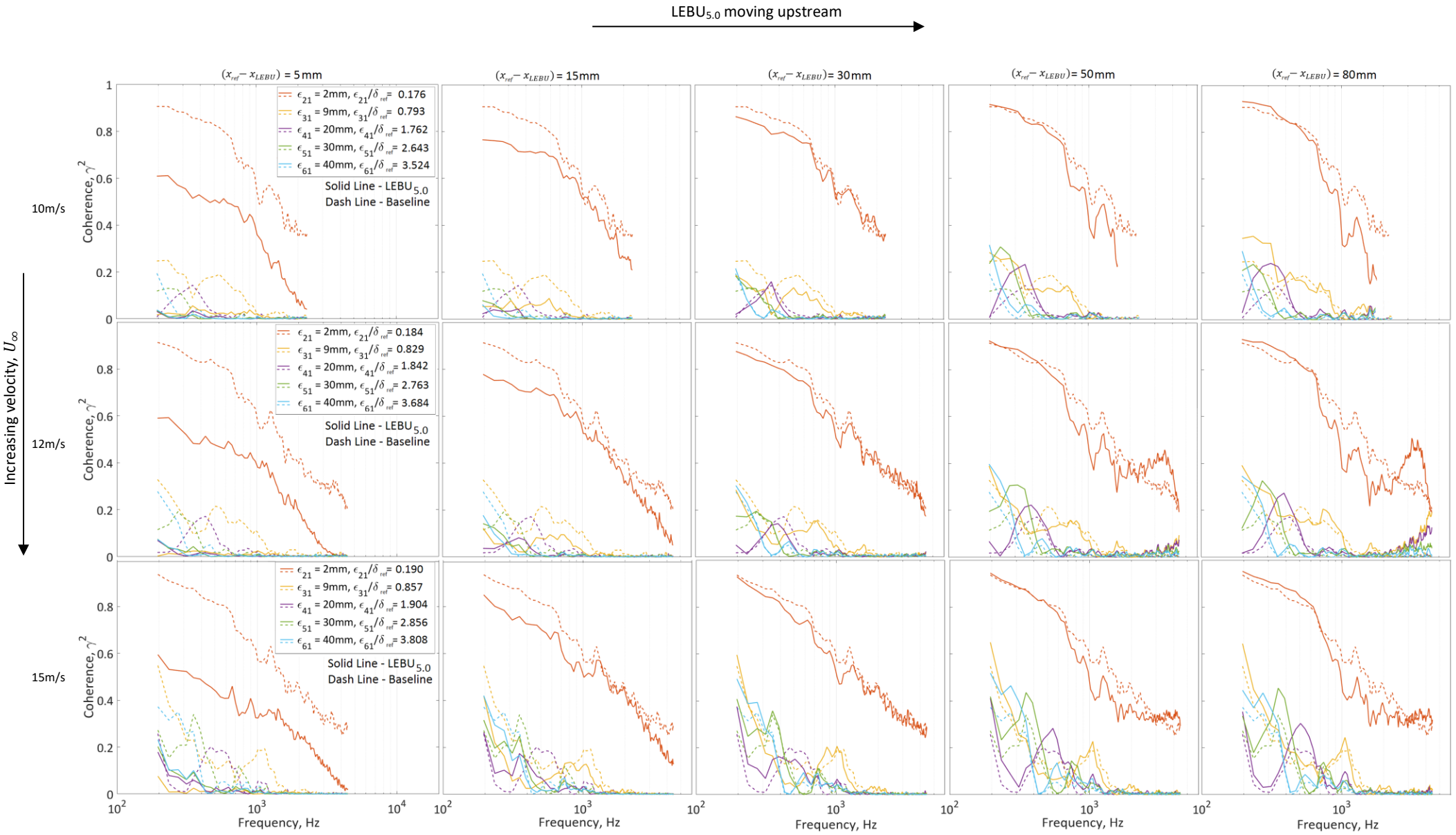

Figure 5.7 – Comparison of Baseline and LEBU$_{5.0}$ streamwise coherence at a) 10m/s, b) 12m/s and c) 15m/s.

5.3.4. Spanwise Coherence

As mentioned in the previous chapter, the spanwise coherence length l_z is a major factor in the radiated treailing edge noise. The surface pressure spanwise coherence subjected to the LEBU treatment is presented in this section, which will then be used to calculate the l_z.

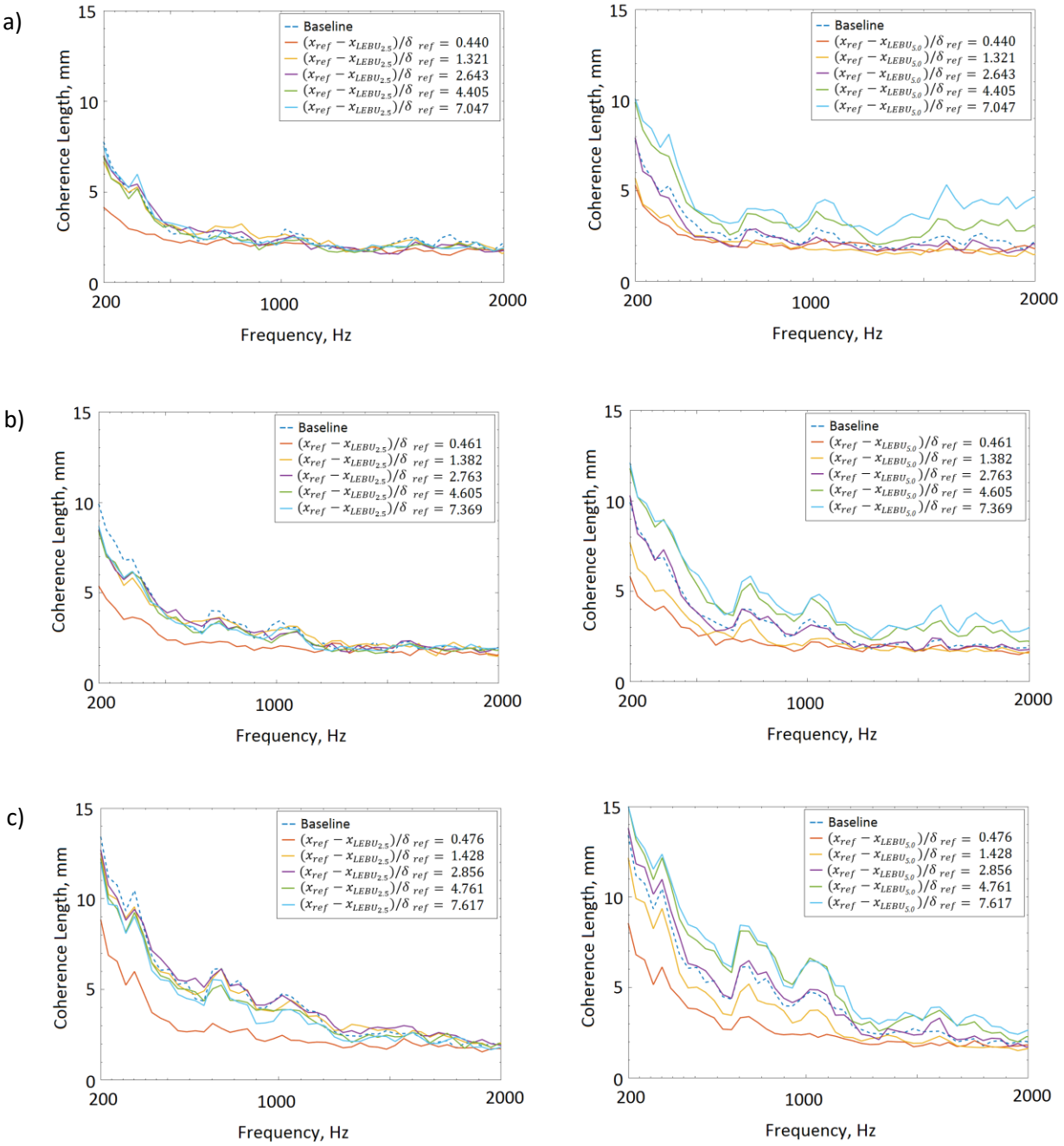

Figure 5.8 – Spanwise coherence length at 625mm downstream with respect to frequency for a) 10 m/s , b) 12m/s and c) 15m/s. LEBU2.5 is on the left, LEBU5.0 is on the right

For brevity, the results of the spanwise coherence are not presented here. Instead, Figure 5.8 shows the spectra of l_z for both the LEBU$_{2.5}$ and LEBU$_{5.0}$. For the LEBU$_{2.5}$ case, there is a clear reduction of the l_z at $(x_{\mathrm{ref}} - x_{\mathrm{LEBU}})/\delta_{\mathrm{ref}} \leq 0.476$ against the Baseline level. When the $(x_{\mathrm{ref}} - x_{\mathrm{LEBU}})/\delta_{\mathrm{ref}}$ increases, i.e. the LEBU$_{2.5}$ is moved further upstream, the l_z largely conforms to, and in certain cases lower than the Baseline level. Therefore, as far as the spanwise coherence length scale of the turbulence is concerned, the LEBU$_{2.5}$ is favourable for the aeroacoustics application. Interestingly, this contradicts to its performance in the wall pressure PSD where no significant reduction against the Baseline is observed.

For the LEBU$_{5.0}$, however, the corresponding l_z spectra are mostly larger level than the Baseline level for intermediate and large upstream placement of the LEBU$_{5.0}$, i.e. $(x_{\mathrm{ref}} - x_{\mathrm{LEBU}})/\delta_{\mathrm{ref}} \geq 4.405$. On the other hand, when $(x_{\mathrm{ref}} - x_{\mathrm{LEBU}})/\delta_{\mathrm{ref}} \leq 2.643$, i.e. the LEBU$_{5.0}$ is closer to the measurement location where near wake interaction will be more intense, the corresponding l_z spectra is lower than the Baseline level.

This follows a similar trend to the Riblet (Chapter 4) where there seems to be a contradiction between the wall pressure PSD and l_z. Again, the implication to the aeroacoustics performance is better informed by examining the $10\ \log 10\ (l_z \cdot S_{qq})$, which is shown in Figure 5.9 for the pressure field at x = 625mm (x_{ref}) and U_∞ = 10, 12 and 15m/s for both the LEBU$_{2.5}$ and LEBU$_{5.0}$. For the LEBU$_{2.5}$, at U_∞*=10 and 12m/s*, from $f > 2000\ Hz$ there is a slight reduction in the $10\ \log 10\ (l_z \cdot S_{qq})$ achieved in the high frequency range by the LEBU$_{2.5}$ placement at $(x_{ref} - x_{LEBU}) \sim 0.461\delta_{ref}$. Otherwise, almost all other LEBU$_{2.5}$ placement would produce an increase of the $10\ \log 10\ (l_z \cdot S_{qq})$ level, as a function of frequency, against the Baseline level. A slightly better outlook is performed by the LEBU$_{5.0}$. Due to the contradiction between the wall pressure PSD and l_z mentioned earlier, large scale reduction of the $10\ \log 10\ (l_z \cdot S_{qq})$ is understandable not observed. However, there still exists a consistent reduction of the $10\ \log 10\ (l_z \cdot S_{qq})$ at f > 600 Hz when $(x_{ref} - x_{LEBU}) > 4.605\delta_{ref}$.

The analysis thus far produces one of the most important outcomes of this thesis. The results show that a LEBU has a potential to reduce the trailing edge self-noise scattering, say at x_{ref}, when two conditions are met:

1. it is placed at a height of between **40** and **50%** of the turbulent boundary layer thickness at x_{ref}. Here the height means the vertical distance between the LEBU and wall surface.
2. it is placed at an upstream distance of about **5 times** the boundary layer thickness at x_{ref}.

It should also be emphasised here that the potential of trailing edge self-noise reduction described above does not applicable to low frequency. Furthermore, the possibility of self-noise generation by

the LEBU itself could compromise the overall aeroacoustics performance but this issue is not considered here.

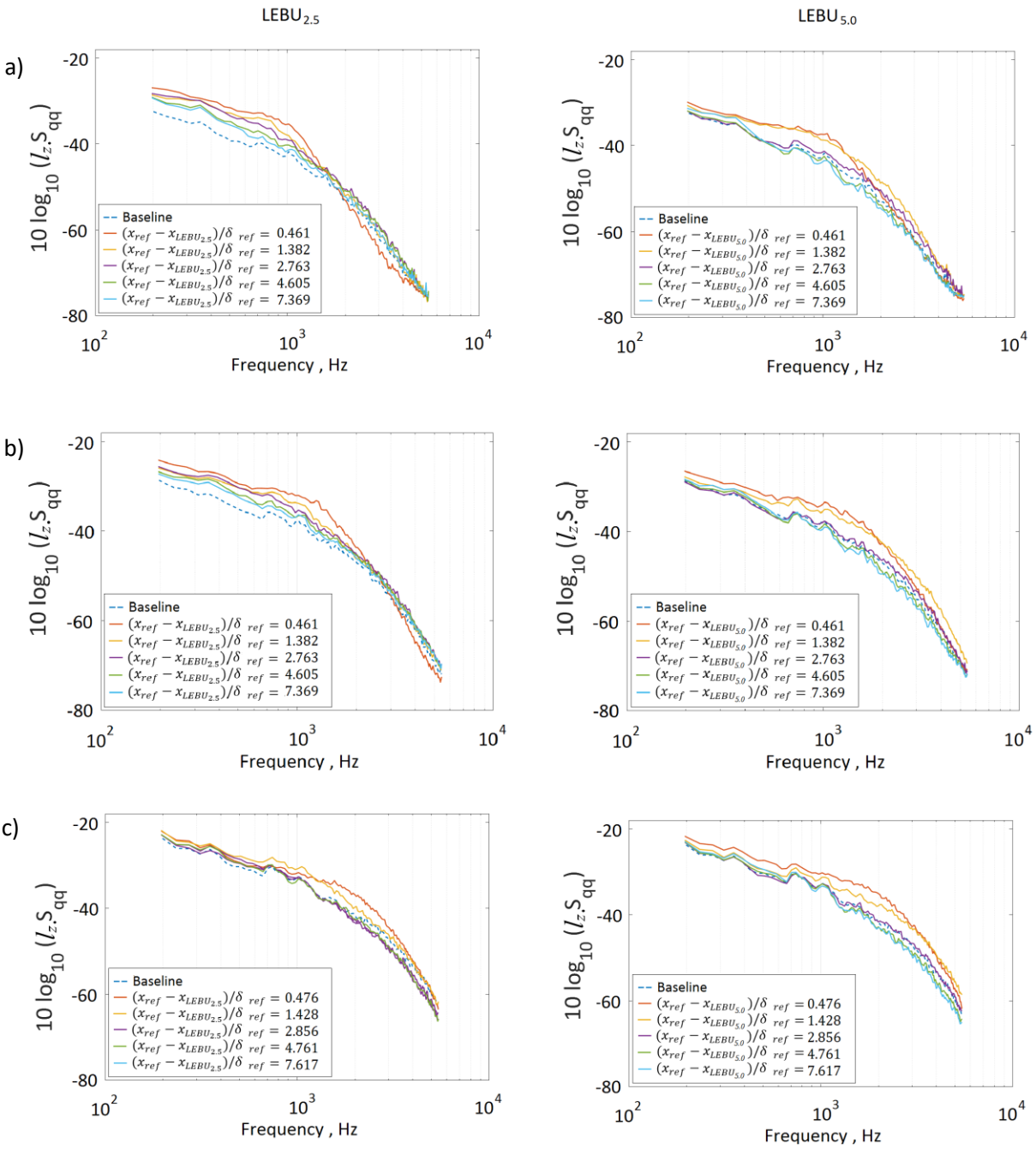

Figure 5.9 – Partial Amiet's model to predict the noise radiation at 625mm for a) 10m/s, b) 12m/s and c) 15m/s. LEBU2.5 is on the left and LEBU5.0 is on the right.

5.4. "Dynamic" Turbulent Boundary layer – analysis based on turbulent spots convecting over a LEBU

The following section looks exclusively at the effect of LEBU placement and configuration on the velocity perturbations and r.m.s. velocity fluctuations of the ensemble-averaged turbulence. The analysis of the turbulence development at the temporal domains can provide some insights into the flow dynamics pertaining to the LEBU, as well as help to explain some of the statistical results presented in the earlier sections.

5.4.1. Velocity Perturbations and r.m.s. Velocity Fluctuations

Similar to the analysis in Chapter 4, the same definition of the velocity perturbation $\tilde{u}$ (Equation 3.10) will also be used here. It is important to note here that the wake generated by the LEBU will be time-invariant. To understand how the generated wake by the LEBU can affect the velocity perturbation, another definition of $\tilde{u}_{wake}$ as described in Equation 5.1 is also used. This will the wake to be considered when examining the turbulent spot.

$$\tilde{u}_{wake} = \frac{\hat{u}(x,y,t) - u_{laminar_{Baseline}}(x,y)}{U_{\infty}(x)}$$

Equation 5.1

$u_{laminar_{Baseline}}$ is defined as the velocity of the undisturbed, untreated (Baseline) laminar boundary at $x_{ref} = 625mm$. $\hat{u}$ is ensemble averaged velocity of the turbulent spot. Note that for all the results presented in this sub-section, the freestream velocity U_{∞} is set at 7m/s.

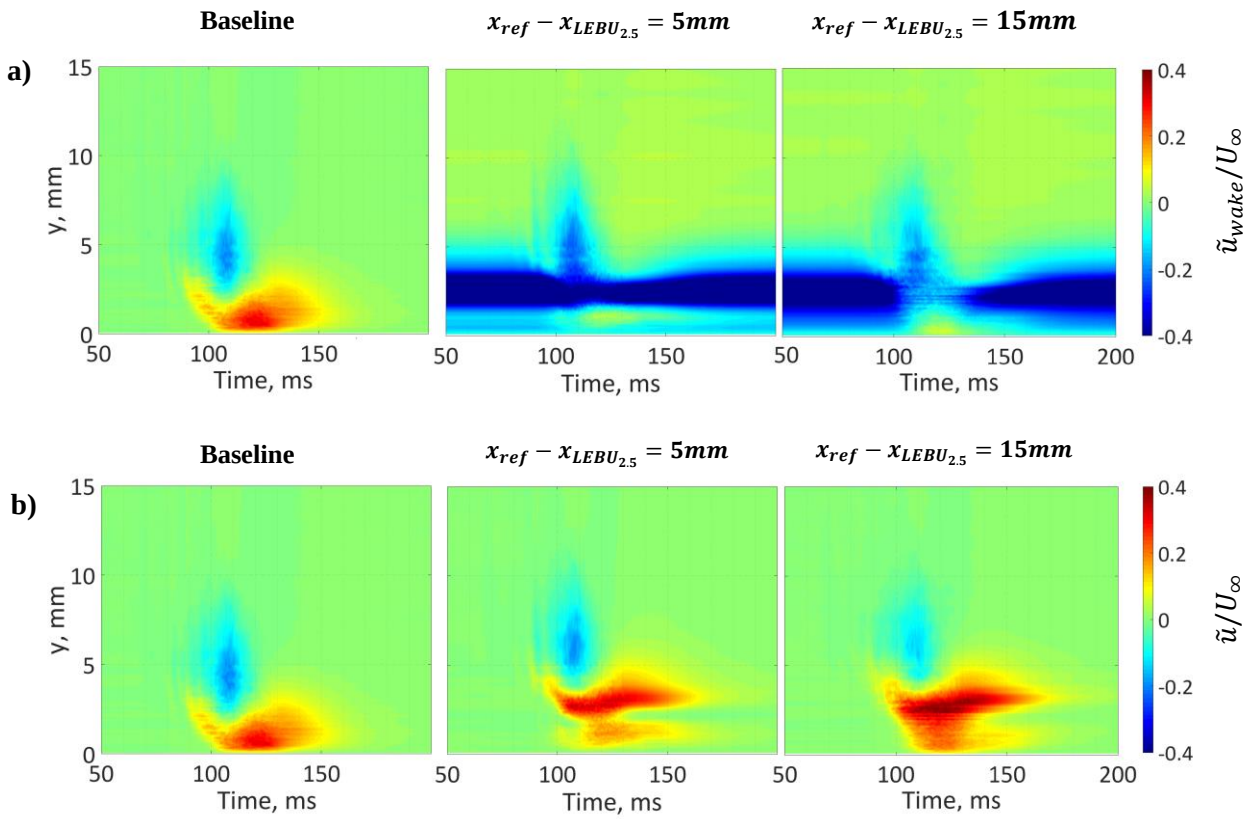

Figure 5.10 – Velocity perturbation contours of a turbulent spot downstream of LEBU2.5 a) highlighted wake interaction, b) turbulent spot inside the wake

Figure 5.10 represents the contours of $\tilde{u}$ and $\tilde{u}_{wake}$ for the LEBU$_{2.5}$. The Baseline case is also included for comparison. The measurement location is always fixed at $x_{ref} = 625mm$. For the $\tilde{u}_{wake}$ in Figure 5.10a, the velocity perturbations in the near wall show a clear momentum deficit in the wake of region that exists throughout the time. It has been discussed in the previous section that the wall–wake interaction by the LEBU$_{2.5}$ is the main cause for the reduced convection velocity. Indeed, this is consistent with the presence of a large-scale momentum deficit observed here. At $x_{ref} - x_{LEBU_{2.5}} = 15mm$, the thickness of the wake region is increased, which would agree with the flow pattern downstream of an aerofoil, where the wake spreads and diffuses. The momentum deficit region of the spot, which occurs at the outer layer, becomes weaker than at $x_{ref} - x_{LEBU_{2.5}} = 5mm$. For both the LEBU$_{2.5}$ locations at $x_{ref} - x_{LEBU_{2.5}} = 5 \; and \; 15mm$, there is no positive perturbation, i.e. momentum excess region near the wall. It seems that the wake has successfully cut off the turbulent spot and deprive the near wall momentum generation that is expected for a canonical turbulent boundary layer. The results highly indicate that the LEBU$_{2.5}$ can alter the turbulent boundary layer significantly.

By using the conventional definition of the velocity perturbation, in this case the $\tilde{u}$, it is possible to exclude the wake perturbation effect and isolate turbulent spot, as shown in Figure 5.10b. At $x_{ref} - x_{LEBU_{2.5}} = 5mm$, it appears that the LEBU$_{2.5}$ has a lifting effect on the turbulent spot, as the main body

of the spot is elevated above the surface, while the spot internal structure and the perturbation level remains relatively intact. There is a small patch of momentum excess underneath the turbulent spot, where it will grow in size when the $LEBU_{2.5}$ is moved further upstream to $x_{ref} - x_{LEBU_{2.5}} = 15mm$. At this particular placement of the $LEBU_{2.5}$, the momentum deficit and excess for the turbulent spot decreases and increases, respectively, compared to the Baseline levels.

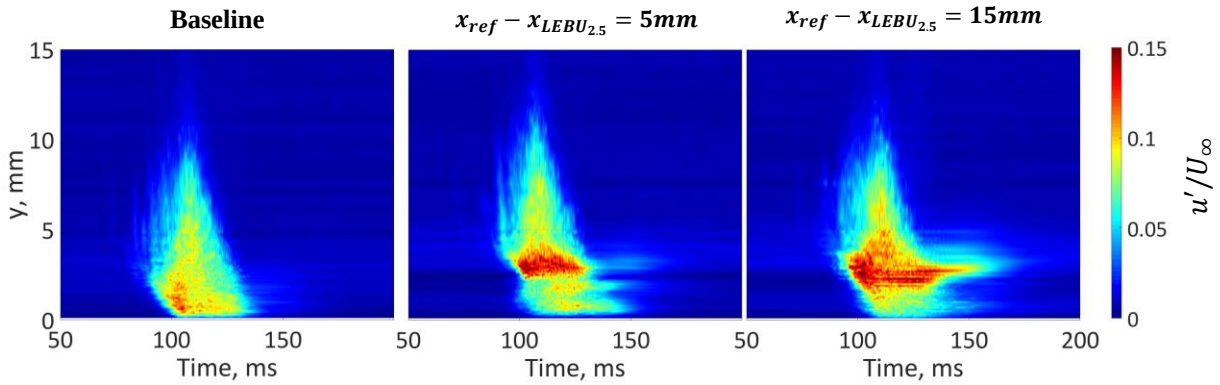

Figure 5.11 – Turbulence intensity contours of a turbulent spot downstream of $LEBU_{2.5}$

Next, the r.m.s. velocity fluctuations is examined. The corresponding turbulent intensity contours for the $LEBU_{2.5}$ is shown in Figure 5.11. At $x_{ref} - x_{LEBU_{2.5}} = 5mm$, while the "lifting" phenomenon is also vividly presented, it shows that there is considerable lower turbulence intensity level at the near wall region. In the outer region of the spot, there is a high intensity region around the height of the $LEBU_{2.5}$. These are the velocity fluctuations caused by the interaction of the outer spot directly with the near wake produced by the $LEBU_{2.5}$. When the $LEBU_{2.5}$ is placed further upstream at $x_{ref} - x_{LEBU_{2.5}} = 15mm$, the high velocity fluctuation zone is elongated as manifested by the wake spreading, but it is still away from the wall surface, which continually to exhibit lower turbulence intensity compared to the Baseline level.

So far, the results from the turbulent spot interaction with the LEBU could be used to explain the wall pressure PSD observed earlier. To recoup, as shown in Figure 5.1, when the $LEBU_{2.5}$ is placed close to the x_{ref}, the wall pressure PSD level at low frequency is higher than the Baseline level, while the opposite is true for the high frequency. This can be explained by the dynamics of turbulent spot presented in Figure 5.11. It shows that the "lifted" turbulent spot, which includes the wake turbulence in its main body, has an overall larger size and elevated turbulence level at the outer region. However, there is not much turbulent spot activity at the near wall region, and the turbulence level is lower than the Baseline level. When the $LEBU_{2.5}$ is placed further upstream, the turbulent spot still remains "lifted" but the interaction with the LEBU wake now occupy a larger spatial and temporal domain. In addition, the turbulence intensity at the outer region is also increased. This explains the observations

in Figure 5.1 for the wall pressure PSD at larger $x_{ref} - x_{LEBU_{2.5}}$, which show that while the low frequency spectra level remains higher than the Baseline level, the high frequency spectra level gradually revert to that of the Baseline level.

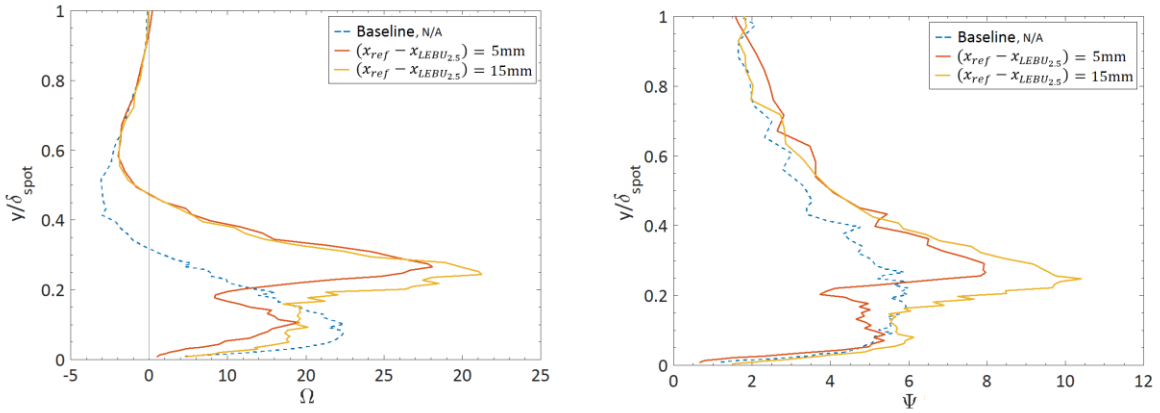

Figure 5.12 – Time integrated velocity perturbations (TIVP) and time integrated turbulence intensity (TITB) for LEBU$_{2.5}$

The mechanisms described above can also be examined quantitatively by the time-integrated velocity perturbations (Ω) and turbulence intensities (Ψ) of the turbulent spot, which are based on Equations 4.8 and 4.9, respectively. The results are shown in Figure 5.12. When the LEBU$_{2.5}$ is placed at $x_{ref} - x_{LEBU_{2.5}} = 5\ and\ 15mm$, the turbulent spot exhibits higher momentum excess in the near wall region but lower velocity deficit at the outer layer when compared to the Baseline. The momentum at the wall is reduced by the LEBU$_{2.5}$, achieving the lowest value at $x_{ref} - x_{LEBU_{2.5}} = 5mm$. It is also shown that the near wall momentum excess will recover as the LEBU$_{2.5}$ is moved upstream. For the time-integrated turbulence intensity, whilst the turbulence intensity is reduced at the near wall region at $x_{ref} - x_{LEBU_{2.5}} = 5mm$, it slowly recovers and even exceed that of the Baseline level at $x_{ref} - x_{LEBU_{2.5}} = 15mm$. The quantitative results presented in Figure 5.12 support the mechanisms discussed in the previous paragraph.

The same analysis is now applies to the LEBU$_{5.0}$ case. Figure 5.13 shows the corresponding velocity perturbations in $\tilde{u}$ and $\tilde{u}_{wake}$. The analysis first focus on the $\tilde{u}_{wake}$. Compared to the LEBU$_{2.5}$, the LEBU$_{5.0}$ shown in Figure 5.13a seems to produce wake that is more localised and less spread. The aforementioned "lifting" process for the turbulent spot does not happen in the LEBU$_{5.0}$ case. The momentum excess region of the turbulent spot at the near wall still remains largely intact but the size could vary with different $x_{ref} - x_{LEBU_{5.0}}$. The results suggest a stronger, less perturbed turbulent spot. As the LEBU$_{5.0}$ is moved upstream from $x_{ref} - x_{LEBU_{5.0}} = 5mm$ to $x_{ref} - x_{LEBU_{5.0}} = 15mm$, the wake becomes less intense and shows signs of dissipation. The momentum excess pertaining to the

turbulent spot near the wall prevails despite the wake entrainment. This trend continues as the $LEBU_{5.0}$ is continuously to be moved upstream. The analysis now focus on the velocity perturbation in $\tilde{u}$ in Figure 5.13b, which can describe the isolated spot better. As the $LEBU_{5.0}$ is moved upstream, the near wall momentum excess region remains intact, and slightly increases in the level compared to the Baseline case. Interestingly, the wake generated by the $LEBU_{5.0}$ can bisect the momentum deficit at the outer layer region, with the bulk of the momentum deficit concentrates at the lower half.

For the corresponding r.m.s. velocity fluctuation contours, they are shown in Figure 5.14. Unlike the $LEBU_{2.5}$ counterpart, the turbulent spots are not "lifted" up when they are interacted with the wake generated by the $LEBU_{5.0}$, which is further away from the wall surface. The turbulence intensity at $x_{ref} - x_{LEBU_{5.0}} = 5mm$ initially shows a marked increase at the near wall, but crucially it is dissipated quickly when the $LEBU_{5.0}$ is gradually moved upstream up to $x_{ref} - x_{LEBU_{5.0}} = 50mm$. At this location, the near wall turbulence intensity level of the turbulent spot is lower than that produced by the Baseline. However, there also seems to have some residue turbulences at the near wall region, which appear to elongate the overall length of the spot. When the $LEBU_{5.0}$ is gradually moved upstream, the dissipation of the turbulence intensity pertaining to the wake at the outer layer region is also demonstrated vividly. The turbulent spot results in Figure 5.14 by the $LEBU_{5.0}$ also correlate quite well with the corresponding wall pressure PSD in Figure 5.2:

1. For $x_{ref} - x_{LEBU_{5.0}} = 5\ and\ 15mm$, the increased wall pressure PSD level compared to the Baseline level (Figure 5.2) is manifested by the increased turbulence intensity level of the turbulent spots at the near wall region in Figure 5.14.
2. For $x_{ref} - x_{LEBU_{5.0}} = 30\ and\ 50mm$, the reduced wall pressure PSD level compared to the Baseline level (Figure 5.2) is also correlated by the reduced turbulence intensity level of the turbulent spots at the near wall region in Figure 5.14.

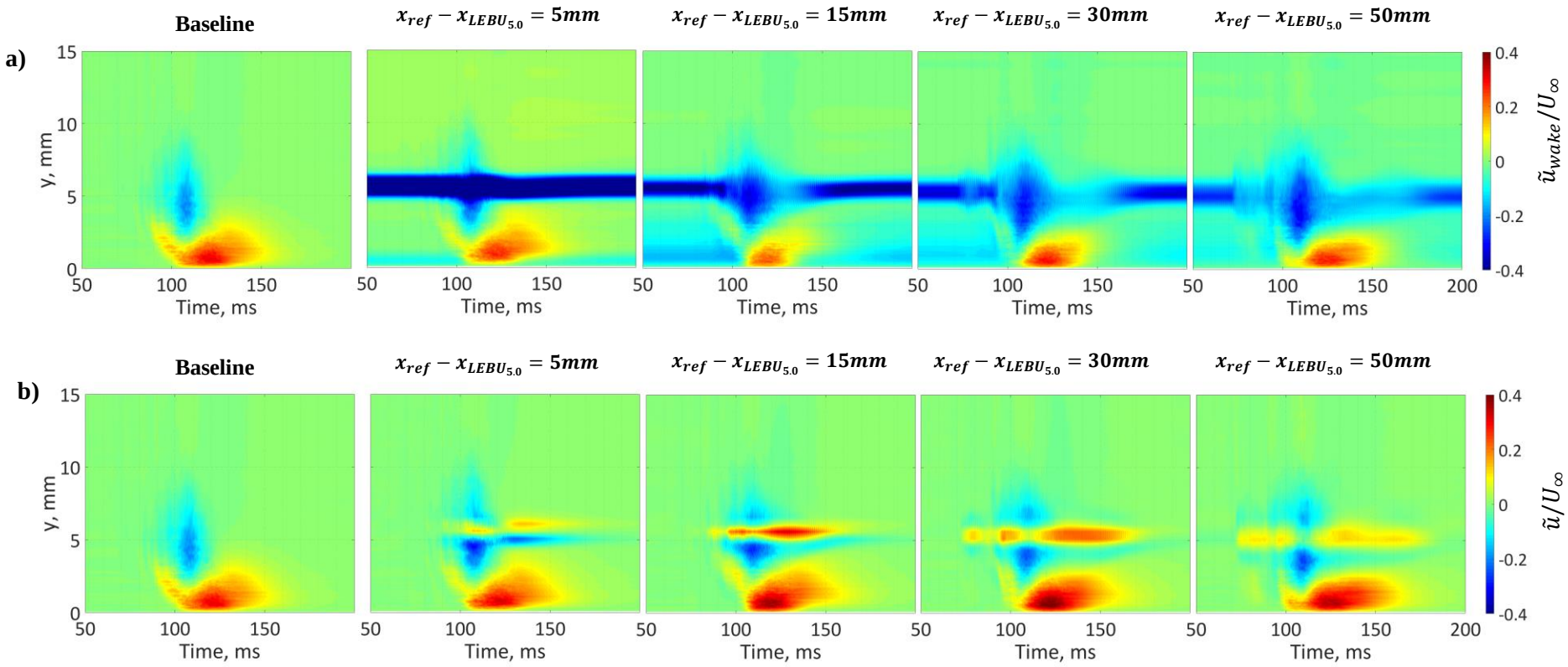

Figure 5.13 – Velocity perturbation countours of a turbulent spot downstream of $LEBU_{5.0}$ a) highlighted spot/wake interaction, b) isolated turbulent spot

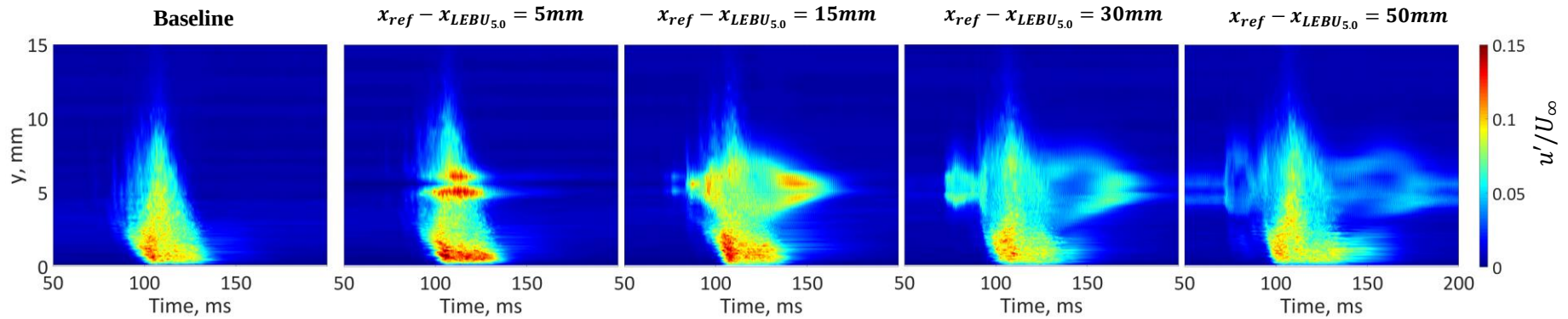

Figure 5.14 – Turbulence intensity perturbation countours of a turbulent spot downstream of $LEBU_{5.0}$

5.5. Hybrid Configurations (Riblet + LEBU)

So far, the efforts have been on the investigation of the effects for the Riblet and LEBU separately. In Chapter 4, especially for the $10\ \log 10\ (l_z \cdot S_{qq})$ spectra presented in Figure 4.15, possible trailing edge self-noise reduction could be achieved by the Riblet at low frequency only. On the other hand, LEBU has been demonstrated in Figure 5.9 that it can reduce the trailing edge self-noise at mid and high frequency, but not at the low frequency.

A logical extension of this work is to combine both the Riblet and LEBU together and investigate whether the effect of the pressure field manipulation can be additive and non-destructive against each other. The aim is especially to investigate whether the reduction of $10\ \log 10\ (l_z \cdot S_{qq})$ by the combined use of Riblet and LEBU is underpinned by a larger frequency range.

The same Riblet is used in the "hybrid", which contains two configurations: (Riblet + $LEBU_{2.5}$) and (Riblet + $LEBU_{5.0}$). The first configuration is called the $HYBRID_{2.5}$, and the second configuration is called the $HYBRID_{5.0}$. Results of the $10\ \log 10\ (l_z \cdot S_{qq})$ for the $HYBRID_{2.5}$ and $HYBRID_{5.0}$ are shown in Figure 5.15 for x = 625mm at U_∞ = 10, 12 and 15m/s. A very promising outcome can be observed in the $10\ \log 10\ (l_z \cdot S_{qq})$ spectra. It shows that the $HYBRID_{5.0}$, when placed at $(x_{ref} - x_{LEBU}) > 4.605\delta_{ref}$, can consistently achieve lower level than the Baseline case throughout the ***entire*** frequency range under investigation here. This provides a hint that the proposed Hybrid configuration can target the turbulent boundary layer independently without much interference against each other.

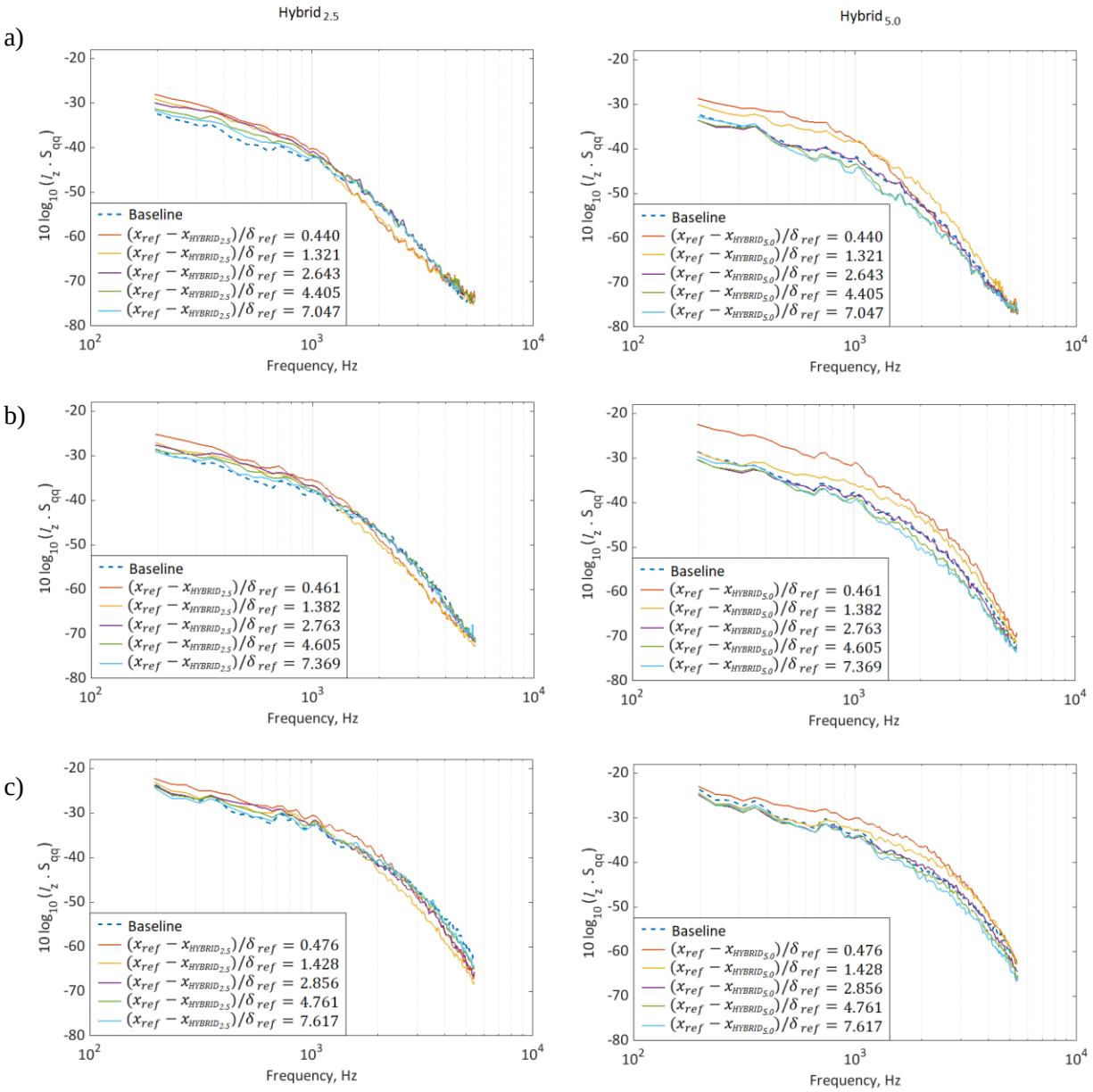

Figure 5.15 – Partial Amiet's model to predict the noise radiation at x = 625mm for a) 10m/s, b) 12m/s and c) 15m/s. Hybrid$_{2.5}$ is on the left and Hybrid$_{5.0}$ is on the right.

5.6. Summary

The following bullet points summarise the main outcomes of this chapter.

- The propagation of the turbulent eddies can be slowed down quite significantly by the LEBU.
- The wall pressure PSD results show that the LEBU can potentially reduce the wall surface energy level of the mid and high frequency pressure fluctuations.

- The spanwise coherence length spectra, on the other hand, predominantly show an increase of the value when the LEBU is present

- The product in the form of 10 $\log_{10}(l_z . S_{qq})$ could provide a hint of the trailing edge noise radiation subjected to the LEBU implemented on the surface. The results show that whilst the LEBU can produce a lower value of 10 $\log_{10}(l_z . S_{qq})$ at the mid and high frequency, they remain largely unchanged at the low frequencies compared to the Baseline due to the counter-balancing effect between the S_{qq} and l_z.

- Very interestingly, the above point is opposite to the 10 $\log_{10}(l_z . S_{qq})$ spectra produced by the Riblet (Chapter 4), in which the Riblet can produce a lower value of 10 $\log_{10}(l_z . S_{qq})$ at the low frequency, but remain largely unchanged at the mid and high frequencies.

- A preliminary study on the combination of Riblet and LEBU has produced very encouraging results whereby both control devices can target the turbulent boundary layer independently without much interference against each other, and produce lower level of 10 $\log_{10}(l_z . S_{qq})$ than the Baseline case throughout the ***entire*** frequency range under investigation here.

- As a final point, for the LEBU itself, an important criteria for an optima geometry for the LEBU are to place it at a height of approximately 50% of the turbulent boundary layer thickness, and at an upstream distance of 5 times of the turbulent boundary layer thickness. Note that the turbulent boundary layer thickness stated here refers to the target location.

Chapter 6 Conclusion and future works

6.1. Conclusion

The main aim of the current thesis was to investigate the effect of the upstream use passive flow control devices of riblets and large eddy break up device (LEBU) on the turbulent boundary layer fluctuating velocity and pressure field. The implication is to determine whether their use can potentially lead to radiated trailing edge noise reduction.

The aims of the current thesis were to:

- Investigate whether drag the reducing riblets can potentially lead to trailing edge noise reduction from turbulent wall pressure fluctuations. Use the fluctuating pressure field beneath a turbulent boundary layer to investigate whether a Large Eddy Break Up Device (LEBU) can potentially reduce trailing edge noise radiation.
- Use turbulent spots to investigate the effect of the riblets and LEBU on the turbulent structure of a single instance of the turbulence to ascertain a potential correlation between the fluctuating streamwise velocity field and pressure field.
- Determine the effect of a hybrid configuration of Riblets and LEBU on a turbulent spot and determine the effects on trailing edge noise radiation.

The turbulent boundary layer over the smooth Baseline and drag reducing Riblets were investigated to provide a comprehensive staring point to this study. Using a single wire hot wire probe, it was established that whilst the velocity profile over the Riblets did not appear to provide significant

change in the profile, there was evidence of an increased momentum in the near wall. There is a skin friction drag reduction, c_f, and reduced streamwise turbulence intensity in the near wall.

The Riblets show limited power spectral density reduction capabilities when compared like for like with the smooth Baseline, however, when scaled by the outer bounder layer parameters, there is clear evidence that the Riblet changes the turbulence scales in the high frequency content of the boundary layer (near wall).

The propagation and coherence of the turbulent eddies by use of the LEBU can be significantly affected when the scale and placement is aimed to facilitate this.

The wall pressure PSD results show that the LEBU can potentially reduce the wall surface energy level of the mid and high frequency pressure fluctuations and with correct scaling and hybridisation (use in conjunction with riblets), there is evidence to suggest that there can be trailing edge noise implications. This is shown by using the measure surface pressure beneath the boundary layer, downstream of the LEBU to create a reduction in the $10 \log_{10}(l_z . S_{qq})$ spectra.

Scaling and optimal placement is a very important factor in this study, and it has been reiterated that LEBU should be placed it at a height of approximately 50% of the turbulent boundary layer thickness, and at an upstream distance of 5 times of the turbulent boundary layer thickness to facilitate trailing edge noise reduction.

6.2. Contribution to research

In an effort to make steps towards a quieter flight through intuitive passive flow control design, this work contributes a study of the flow interaction between a turbulent spot and the LEBU. Little work has been carried out thus far using this method.

This thesis also successfully uses rapid prototyping SLA 3D printing to manufacture the riblet and LEBU geometry. This adds to the validity of the method for small scale aerodynamic geometries and can lead to further studies in this area.

Trailing edge noise reduction has not used this technique before, and I submit this work to the body of knowledge about the wall pressure fluctuations beneath a turbulent boundary with the implication solely on trailing edge noise reduction.

6.3. Future works

To continue the study of this work further, the following suggestions are made for future study:

- Cross-wire velocity measurements to establish the wall normal velocity fluctuations that contribute to the fluctuating pressure field beneath the turbulent boundary layer.

- Simultaneous pressure and velocity fluctuation measurements for cross to analyse the pressure field in the temporal domain to establish significant events inside the boundary layer including sweeps and ejections.

- Actual radiated noise measurements of the turbulent boundary layer and trailing edge noise with and without treatments to establish the accuracy of the predicted radiated noise.

- Installation of the Riblets and LEBU on an airfoil for airfoil noise measurements to determine the lift, drag and stall angle changes that the riblets and LEBU cause to normal operating conditions.

Chapter 7 References

1. **Airbus.** *Global Market Forecast 2018-2037.* Blagnac Cedex, France : Airbus S.A.S, 2018.

2. **IATA.** *International Air Transport Association Annual Review 2019.* Soel : IATA, 2019.

3. —. IATA Forecast Predicts 8.2 billion Air Travelers in 2037. *IATA Press Release.* [Online] IATA, October 24, 2018. [Cited: August 29, 2019.] https://www.iata.org/pressroom/pr/Pages/2018-10-24-02.aspx.

4. **ICAO.** [Online] https://www.icao.int/environmental-protection/Pages/noise.aspx .

5. **Airbus.** Global Market Forecast 2017-2036. *Airbus.* [Online] http://www.airbus.com/content/dam/corporate-topics/publications/backgrounders/Airbus_Global_Market_Forecast_2017-2036_Growing_Horizons_full_book.pdf.

6. **European Aviation Safety Agency.** European Aviation Environmental Report 2019. [Online] 2019. https://www.easa.europa.eu/eaer/system/files/usr_uploaded/219473_EASA_EAER_2019_WEB_LOW-RES.pdf.

7. **Kempton, Andrew.** *Acoustic liners for modern aero-engines.* Southampton : Rolls Royce, 2011.

8. **Dobrzynski, Werner.** Almost 40 Years of Airframe Noise Research: What Did We Achieve? *Journal of Aircraft.* 2010, Vol. 47, 2, pp. 353-367.

9. **Proenca, Anderson.** *Aeroacoustics of isolated and installed jets under static and in-flight conditions.* Faculty of Engineering and the EnvironmentInstitute of Sound and Vibration. Southampton : University of Southampton, 2018. Thesis.

10. **GE.** How Loud Is A Wind Turbine? *GE Reports.* [Online] GE, August 2nd, 2014. https://www.ge.com/reports/post/92442325225/how-loud-is-a-wind-turbine/.
11. **Copping, Jasper and Gray, Richard.** Switch-off for noisy wind fars. *The Telegraph.* [Online] November 11, 2011. https://www.telegraph.co.uk/news/earth/energy/windpower/8901431/Switch-off-for-noisy-wind-farms.html.
12. **Vathylakis, Alexandros.** *Reduction of broadband trailing edge noise by serrations.* London UK : Brunel University London, 2015.
13. **Pope, S.** *Turbulent Flows.* Cambridge : Cambridge University Press, 2000.
14. **S. J. Kline, W. C. Reynolds, F. A. Schraub, P. W. Runstadlers.** The Structure Of Turbulent Boundary Layers. *Journal Fluid Mechanics.* 1967, Vol. 30, 4, pp. 741 - 773.
15. **Willmarth, W . W .** Structure of Turbulence in Boundary Layers. *Advances In Applied Mechanics.* 1975, Vol. 15, pp. 159-254.
16. **H. T. Kim, S. J. Kline and W. C. Reynolds.** The production of turbulence near a smooth wall in a turbulent boundary layer. *Journal of Fluid Mechanics.* 1971, Vol. 50, 01, pp. 133-160.
17. **Laufer, John.** *The structure of turbulence in fully developed pipe flow.* Washington, DC : NACA, 1954.
18. **PW Runstadler, SJ Kline, WC Reynolds.** *An experimental investigation of the flow structure of the turbulent boundary layer.* Stanford, California : Stanford University, 1963. PhD Thesis.
19. **E. R. Corino, Robert S. Brodkey.** A visual investigation of the wall region in turbulent flow. *Journal of Fluid Mechanics.* 1969, Vol. 37, 1, pp. 1-.
20. **G. R. Offen, S. J. Kline.** Combined dye-streak and hydrogen-bubble visual observations of a turbulent boundary layer. *Journal of Fluid Mechanics.* 1974, Vol. 62, 2, pp. 223-.
21. **B-K. Ahn, W. R. Graham.** *Modelling Unsteady Wall Pressures Beneath Turbulent Boundary Layers.* Manchester, UK : AIAA/CEAS 10th Aeroacoustics Conference, 2004.
22. **G. R. Offen, S. J. Kline.** A proposed model of the bursting process in turbulent boundary layers. *Joural of Fluid Mechanics.* 1975, Vol. 70, 2, pp. 209-.
23. **Head, M.R. and Bandyopadhyay, P. R.** New aspects of turbulent boundary-layer structure. *Journal of Fluid Mechanics.* 1981, Vol. 107, pp. 297-338.
24. **Emmons, H. W.** The Laminar-Turbulent Transition in a Boundary Layer - Part 1. *Journal Of The Aeronautical Sciences.* 1951, Vol. 18, pp. 490-498.
25. **Shubauer, G. B. and Klebanoff, P. S.** *Contributions on the Mechanics of Boundary-Layer Transition.* Washington : National Advisory Comittee for Aeronautics - Technical Note 3489, 1955.
26. **Cantwell, Brian, Coles, Donald and Dimotakis, Paul.** Structure and entrainment in the plane of symmetry of a turbulent spot. *Journal of Fluid Mechanics.* 1978, Vol. 87, 4, pp. 641-672.
27. **Riley, James J. and Gad-el-Hak, Mohamed.** The Dynamnics of Turbulent Spots. *Frontiers in Fluid Mechanics.* 1985, pp. 123-155.

28. **Falco, R. E.** Coherent motions in the outer region of turbulent boundary layers. *Physics of Fluids.* 1977, Vol. 20, pp. S124-S132.
29. **Gad-El-Hak, Mohamed, Blackwelder, Ron F. and Riley, James J.** On the Growth of Turbulent Regions in Laminar Boundary Layers. *Journal of Fluid Mechanics.* 1981, Vol. 110, pp. 73 - 95.
30. **Wygnanski, I., Sokolov, M. and Friedman, D.** On a turbulent 'spot' in laminar boundary layer. *Journal of Fluid Mechanics.* 1976, Vol. 78, pp. 785-819.
31. **Reif, W. E. and Dinkelacker, A.** Hydrodynamics of the squamation in fast swimming sharks. *Neues Jahrbuch fuer Geologie und Palaeontologie.* 1982, pp. 184 - 187.
32. **D. Becheret, W. Reif.** *On the Drag Reduction of the Shark Skin.* Colorado : AIAA 23rd Aerospace Sciences Meeting Shear Flow Control Conference, 1985.
33. **Dean, Brian and Bhushan, Bharat.** Shark-Skin Surfaces for Fluid-Drag Reduction in Turbulent Flow: A Review. *Philosophical Transactions of The Royal Society A Mathematical Physical and Engineering Sciences.* 2010, Vol. 368, pp. 4775-806.
34. **Walsh, M.J.** *Turbulent Boundary Layer Drag Reduction Using Riblets.* Hampton, VA : American Institute of Aeronautics and Astronautics 20th Aerospace Sciences Meeting, 1982.
35. **Hooshmand, A., et al.** An experimental study of changes in the structure of a turbulent boundary layer due to surface geometry changes. *21st American Institute of Aeronautics and Astronautics, Aerospace Sciences Meeting.* 1983.
36. **Pulles, C. J. A.** *Drag reduction of turbulent boundary layers by means of grooved surfaces.* Eindhoven, Netherlands : Technische Universiteit Eindhoven, 1988. Thesis.
37. **Bacher, E. V. and Smith, C. R.** *A Combined Visualization-Anemometry Study of the Turbulent Drag Reducing Mechanisms of Triangular Micro-Groove Surface Modifications.* Boulder, Colorado : AIAA Shear Flow Control Conference, 1985.
38. **Gallagher, J. A. and Thomas, A. S. W.** Turbulent Boundary Layer Charachteristics Over Streamwise Grooves. *AIAA 2nd Applied Aerodynamics Conference.* 1984.
39. **Choi, Kwing-So.** Near-wall structure of a turbulent boundary layer with riblets. *Journal of Fluid Mechanics.* 1989, Vol. 208, pp. 417-458.
40. **S. J Lee, S. H. Lee.** Flow field analysis of a turbulent boundary layer over a riblet surface. *Experiments in Fluids.* 2001, Vol. 30, pp. 153–166.
41. **Walsh, Michael J.** *Riblets as a Viscous Drag Reduction Technique.* Orlando : AIAA, 1983.
42. **Bacher, E.V and Smith, C. R.** Turbulent Boundary-Layer Modification by Surface Riblets. *AIAA Journal.* 1986, Vol. 28, 8.
43. **Yong Chae Jung, Bharat Bhushan.** Biomimetic Structures or Fluid Drag Reduction in Laminar and Turbulent Flows. *Journal of Physics: Condensed Matter.* 2009, Vol. 22, 3.
44. **Chamorro, Leonardo P., Arndt, R.E.A. and Sotiropoulos, F.** Drag reduction of large wind turbine blades through riblets: Evaluation of riblet geometry and application strategies. *Renewable Energy.* 2013, Vol. 50, pp. 1095 - 1105.

45. **Sareen, Agrim, et al.** Drag Reduction Using Riblet Film Applied to Airfoils for Wind Turbines. *Journal of Solar Energy Engineering.* 2013, Vol. 136, 2.
46. **Walsh, M.J. and Lindemann, A. M.** *Optimization and Application of Riblets for Turbulent Drag Reduction.* Reno, Nevada : AIAA 22nd Aerospace Sciences Meeting 22nd Aerospace Sciences Meeting, 1984.
47. **Walsh, Michael J., Sellers, William L. and McGinley, Catherine B.** *Riblet Drag Reduction at Flight Conditions.* Williamsbug, VA : AIAA 6th Applied Aerodynamics Conference, 1988.
48. **Szodruch, J.** Viscous Drag Reduction on Transport Aircraft. *American Institute of Aeronautics and Astronautics 29th Aerospace Sciences Meeting.* 1991.
49. **Zuniga, Fanny A., Anderson, Bianca T. and Bertelrud, Arlid.** *Flight Test Results of Riblets at Supersonic Speeds.* USA : NASA Technical Memorandum 4387, 1992.
50. **Sandborn, V. A.** *Control of surface shear stress fluctuations in turbulent boundary layers.* Colorado : Colorado State University. Libraries, 1981. Report.
51. **Walsh, M. J. and Weinstein, L. M.** Drag and Heat Transfer on Surfaces with Small Longitudinal Fins. *11th Fluid and Plasma Dynamics Conference.* 1978.
52. **Bechert, D. W., et al.** Experiments on drag-reducing surfaces and their optimization with an adjustable geometry. *Journal of Fluid Mechanics.* 1997, Vol. 338, pp. 59-87.
53. **El-Samni, O. A., Chun, H. H. and H.S.Yoon.** Drag reduction of turbulent flow over thin rectangular riblets. *International Journal of Engineering Science.* 2007, Vol. 45, 2-8, pp. 436-454.
54. **Kurita, Mitsuru, et al.** Flight Test of a Paint-Riblet for Reducing Skin-Friction. *AIAA 2018 Applied Aerodynamics Conference.* 2018.
55. **Stenzel, Volkmar, Wilke, Yvonne and Hage, Wolfram.** Drag-reducing paints for the reduction of fuel consumption in aviation and shipping. *Progress in Organic Coatings.* 2010, Vol. 70, 4, pp. 24-229.
56. **Huawei Chen, Fugang Rao, Xiaopeng Shang, Deyuan Zhang, Ichiro Hagiwara.** Flow over bio-inspired 3D herringbone wall riblets. *Experiments in Fluids.* 2014, Vol. 55, 3, pp. 1698-.
57. **Bechert, D. W., Bruse, M., & Hage, W.** Experiments with three-dimensional riblets as an idealized model of shark skin. *Experiments in Fluids.* 2000, Vol. 28, 5, pp. 403-412.
58. **Bechert, D. W., Ghoppe, G. and Reif, W. E.** *On the drag reduction of the shark skin.* Boulder, Colorado : AIAA 23rd Aerospace Sciences Meeting, 1985.
59. **García-Mayoral, Ricardo and Jiménez, Javier.** Drag reduction by riblets. *Philosophical Transactions of The Royal Society A Mathematical, Physical and Engineering Sciences.* 2011, Vol. 369, 1940, pp. 1412-1427.
60. **García-Mayoral, R. and Jiménez, J.** Hydrodynamic stability and the breakdown of the viscous regime over riblets. *Journal of Fluid Mechanics.* 2011, Vol. 678, pp. 317 - 347.
61. **Grek, G. R., Kozlov, V. V. and Titarenko, S. V.** An Experimental Study of the Influence of Riblets on Transition. *Journal of Fluid Mechanics.* 1996, Vol. 315, pp. 31-49.

62. **Ancrum, Derek. B. and Yaras, Metin. I.** Measurement of the Effect of Streamwise Riblets on Boundary layer Turbulence. *Journal of Fluids Engineering.* 2017, Vol. 139, 11.
63. **Yajnik, K. S., & Acharya, M.** Non-equilibrium effects in a turbulent boundary layer due to the destruction of large eddies. *Lecture Notes in Physics.* Bangalore : Springer, 1977.
64. **Jerry N. Hefner, Leonard M. Weinstein,t and Dennis M. Bushnell.** Large-Eddy Breakup Scheme for Turbulent Viscous Drag Reduction. *AIAA.* 1979, pp. 110-127.
65. **Savill, A. M. and Mumford, J. C.** Manipulation of turbulent boundary layers by outer-layer devices: skin-friction and flow-visualization results. *Journal of Fluid Mechanics.* 1988, Vol. 191, pp. 389 - 418.
66. **I. V. Gudilin, Yu. A. Lashkov & V. G. Shumilkin.** Combined effect of longitudinal riblets and LEBU-devices on turbulent friction on a plate. *Fluid Dynamics.* 1995, Vol. 30, pp. 366 - 371.
67. **Lighthill, M. J.** On Sound Generated Aerodynamically. I. General Theory. *Proceedings of the Royal Society of London. Series A, Mathematical and Physical Sciences.* 1952, Vol. 211, 1107, pp. 564–587.
68. —. On Sound Generated Aerodynamically. II. Turbulence as a Source of Sound. *Proceedings of the Royal Society of London. Series A, Mathematical and Physical Sciences.* 1954, Vol. 222, 1148, pp. 1-32.
69. **Blake, William K.** *Mechanics of Flow-Induced Sound and Vibration : General concepts and Elementary Sources.* London : Academic Press Inc., 1986. Vol. Volume 1.
70. **Fluent Inc.** *Acoustics Module Manual.* Lebanon : Fluent Inc., 2003.
71. **Barbier, Charlotte, Jenner, Elliot and D'Urso, Brian.** Large Drag Reduction over Superhydrophobic Riblets. *arXiv.org.* 2014.
72. **Siegel, Frank, Klug, Ulrich and Kling, Rainer.** Extensive Micro-Structuring of Metals using Picosecond Pulses – Ablation Behavior and Industrial Relevance. *Journal of Laser Micro/Nanoengineering.* 2009, Vol. 4, 2, pp. 104-110.
73. **Denkena, Berend, Kohler, Jens and Wang, Bo.** Manufacturing of functional riblet structures by profile grinding. *CIRP Journal of Manufacturing Science and Technology.* 2010, Vol. 3, 1, pp. 14-26.
74. **Manhee Han, Hee Chang Lim, Young-Gil Jang, Seung S. Lee, and Sang-Joon Lee.** Fabrication of a Micro-Riblet Film and Drag Reduction Effects on Curved Objects. *The 12th International Conference on Salid Slate Sensors. Actuators and Microsyslems.* 2003, pp. 396-399.
75. **Kim, Tae Wan.** Assessment of Hydro/Oleophobicity for Shark Skin Replica with Riblets. *American Scientific Publishers.* 2014, Vol. 14.
76. **Zhao, Dan-Yang, et al.** Vacuum casting replication of micro-riblets on shark skin for drag-reducing applications. *Journal of Materials Processing Technology.* 2012, Vol. 212, 1, pp. 198-202.
77. **Mann, Ethan E, et al.** Surface micropattern limits bacterial contamination. *Antimicrobial Resistance and Infection Control.* 3, 2014, Vol. 1.

78. **Wen, Li, Weaver, James C. and Lauder, George V.** Biomimetic shark skin: design, fabrication and hydrodynamic function. *The Journal of Experimental Biology.* 2014, Vol. 217, 10, pp. 1656-1666.
79. **Tonkin, Leah, et al.** *Surface topographies for non-toxic bioadhesion control.* Florida : Patent Application Publication, 2016.
80. **Bhushan, Bharat and Caspers, Matt.** An overview of additive manufacturing (3D printing) for microfabrication. *Microsystem Technologies.* 2017, Vol. 23, 4, pp. 1117–1124.
81. **Young, A.D.** *Boundary Layers.* Oxford : BSP Professional Books, 1989.
82. **E. L. Houghton, P. W. Carpenter.** *Aerodynamics for Engineering Students 5th Edition.* Oxford : Butterworth-Heineman, 2003.
83. **Sagrado, Ana Garcia.** *Boundary Layer and Trailing Edge Noise Sources.* Cambridge : University of Cambridge, 2007. Thesis.
84. **Gruber, Mathieu.** *Airfoil noise reduction by edge treatments.* Faculty of Engineering an the Environment, University of Southampton. 2012. PhD Thesis.
85. **Afshari, Abbas, et al.** Trailing Edge Noise Reduction Using Novel Surface Treatments. *22nd AIAA/CEAS Aeroacoustics Conference.* 2016.
86. **Corcos, G. M.** Resolution of Pressure in Turbulence. *The Journal of the Acoustical Society of America.* 1963, Vol. 35, 2, pp. 192-.
87. **Goody, M.** Emperical Spectral Model of Surface Pressure Fluctuations. *AIAA Journal.* 2004, Vol. 42, 9.
88. **Schewe, Günter.** On the Structure and Resolution of Wall-Pressure Associated with Turbulent Boundary-Layer Flow. *Journal of fluid Mechanics.* 1983, Vol. 134, pp. 311-328.
89. **Bearman, P. W.** Corrections for the Effect of Ambient temperature Drift on Hot-Wire Measurements in Incompressible Flow. *DISA Information No. 11.* 1971.
90. **Jørgensen, Finn E.** *How to measure turbulence with hot-wire anemometers - a practical guide.* Skovlunde, Denmark : Dantec Dynamics, 2001. Technical Report.
91. **Gaster, M. and Grant, I.** An Experimental Investigation of the Formation and Development of a Wave Packet in a Laminar Boundary Layer. *Philosophical Transactions of The Royal Society A Mathematical Physical and Engineering.* 1975, Vol. 347, pp. 253-269.
92. **Bechert, D. W. and Bartenwerfer, M.** The viscous flow on surfaces with longitudinal ribs. *Journal of Fluid Mechanics.* 1989, pp. 105-129.
93. **Clauser, Francis H.** Turbulent Boundary Layers in Adverse Pressure Gradients. *Journal of the Aeronautical Scienes.* 21, 1954, Vol. 2, pp. 91-108.
94. **Squire, L. C. and Savill, A. M.** *Some experiences of riblets at transonic speeds.* London : Proc. Intl Conf. Turbulent Drag Reduction by Passive Means, 1987.
95. **Bandyopadhyay, P. R.** *Review - Mean Flow in Turbulent Boundary Layers Disturbed to Alter Skin Friction.* Hampton, Virginia : AIAA 4th Joint Fluid Mechanics, Plasma Dynamics and Lasers Conference, 1989.

96. **Schlichting, H. and Gersten, K.** *Boundary Layer Theory (8th Edition).* New York : Springer-Verlag Berlin Heidelberg, 2000.
97. **Gravante, S. P., et al.** Characterization of the Pressure Fluctuations Under a Fully Developed Turbulent Boundary Layer. *AIAA Journal.* 1998, Vol. 36, 10, pp. 1808-1816.
98. **Brooks, T. F. and Hodgson, T. H.** Trailing Edge Noise Prediction from Measured Surface Pressures. *Journal of Sound and Vibration.* 1981, Vol. 78, 1, pp. 69-117.
99. **Amiet, R. K.** Noise due to turbulent flow past a trailing edge. *Journal of Sound and Vibrabration.* 1976, Vol. 43, 3, pp. 387–393.
100. —. Acoustic radiation from an airfoil in a turbulent stream. *Journal of Sound and Vibration.* 1975, Vol. 41, 4, pp. 407 - 420.
101. **Wygnanski, I., Zilberman, M. and Haritonidis, Joseph H.** On the spreading of a turbulent spot in the absence of a pressure gradient. *Journal of Fluid Mechanics.* 1982, Vol. 123, pp. 69 - 90.
102. **Mautner, T. S and Atta, C. W. Van.** Wall shear stress measurements in the plane of symmetry of a turbulent spot. *Experiments in Fluids.* 1986, Vol. 4, 3, pp. 153 - 162.
103. **Glezer, A., Katz, Y. and Wygnanski, I.** On the breakdown of the wave packet trailing a turbulent spot in a laminar boundary layer. *Journal of Fluid Mechanics.* 1989, Vol. 198, pp. 1 - 26.
104. **Savill, A. M. and Mumford, J. C.** Manipulation of turbulent boundary layers by outer-layer devices: skin friction and flow visualization results. *Journal of Fluid Mechanics.* 1988, Vol. 191, pp. 389 - 418.
105. **Bertelrud, A., Truong, T. and Avellan, F.** Drag reduction in turbulent boundary layers using ribbons. *American Institute of Aeronautics and Astronautics 9th Atmospheric Flight Mechanics Conference.* 1982.
106. **Corke, Thomas, Nagib, Hassan M and Guezennec, Yann.** A New View on Origin, Role and Manipulation of Large Scales in Turbulent Boundary Layers. *NASA Technical Report Server.* 1982.
107. **Hefner, Jerry N., Anders, John B. and Bushnell, Dennis M.** Alteration of Outer Flow Structures for Turbulent Drag Reduction. *21st American Institute of Aeronautics and Astronautics, Aerospace Sciences Meeting.* 1983.
108. **Dowling, A. P.** The effect of large-eddy breakup devices on flow noise. *Journal of Fluid Mechanics.* 1989, pp. 193-223.
109. **Corcos, G. M.** The resolution of Turbulent Pressures at the Wall of a Turbulent Boundary Layer. *Journal of Sound and Vibration.* 1967, Vol. 6, 1, pp. 59-70.
110. **Gad-El-Hak, Mohamed, Blackwelder, Ron F. and Riley, James J.** On the Growth of Turbulent Regions in Laminar Boundary Layers. *Journal of Fluid Mechanics.* 1981, Vol. 110, pp. 73-95.
111. **Walsh, M. J. and Lindemann, A. M.** *Optimization and Application of Riblets for Turbulent Drag Reduction.* Reno, Nevada : American Institute of Aeronautics and Astronautics 22nd Aerospace Sciences Meeting, 1984.

112. **Wilmarth, W. W.** Wall Pressure Fluctuations In A Turbulent Boundary Layer. *The Journal Of The Acoustical Society Of America.* 1956, Vol. 28.